MEASUREMENT OF LIFT AND DRAG IN MORPHING WINGS USING A HIGH PRECISION LOAD CELL

A THESIS SUBMITTED TO
THE GRADUATE SCHOOL OF NATURAL AND APPLIED SCIENCES
OF
MIDDLE EAST TECHNICAL UNIVERSITY

BY

MEHMET HARUN ÖZKANAKTI

IN PARTIAL FULFILLMENT OF THE REQUIREMENTS
FOR
THE DEGREE MASTER OF SCIENCE
IN
AEROSPACE ENGINEERING

MAY 2015

Approval of the thesis:

MEASUREMENT OF LIFT AND DRAG IN MORPHING WINGS USING A HIGH PRECISION LOAD CELL

submitted by **MEHMET HARUN ÖZKANAKTI** in partial fulfillment of the requirements for the degree of **Master of Science in Aerospace Engineering Department, Middle East Technical University** by,

Prof. Dr. Gülbin Dural Ünver
Dean, Graduate School of **Natural and Applied Sciences** _____

Prof. Dr. Ozan Tekinalp
Head of Department, **Aerospace Engineering** _____

Prof. Dr. Serkan Özgen
Supervisor, **Aerospace Engineering Dept., METU** _____

Examining Committee Members:

Prof. Dr. Nafiz Alemdaroğlu
Aerospace Engineering Dept., METU _____

Prof. Dr. Serkan Özgen
Aerospace Engineering Dept., METU _____

Assoc. Prof. Dr. Melin Şahin
Aerospace Engineering Dept., METU _____

Prof. Dr. Zafer Dursunkaya
Mechanical Engineering Dept., METU _____

Prof. Dr. Yusuf Uludağ
Chemical Engineering Dept., METU _____

Date: _____

I hereby declare that all information in this document has been obtained and presented in accordance with academic rules and ethical conduct. I also declare that, as required by these rules and conduct, I have fully cited and referenced all material and results that are not original to this work.

Name, Last Name: MEHMET HARUN ÖZKANAKTI

Signature :

ABSTRACT

MEASUREMENT OF LIFT AND DRAG IN MORPHING WINGS USING A HIGH PRECISION LOAD CELL

Özkanaktı, Mehmet Harun
M.S., Department of Aerospace Engineering
Supervisor: Prof. Dr. Serkan Özgen

May 2015, 118 pages

This thesis focuses on computational and experimental investigation of three different morphing wing planforms and a baseline wing planform using a commercial CFD software and load cell measurements for the validation of an optimization code developed in a separate study. The wing planforms of interest originate from an optimization tool that minimizes drag for a constant value of lift at a given velocity. The first planform of interest is the planform for optimized drag subject to 14 m/s freestream velocity with constraints for physical dimensions and taper ratio. The other two planforms are generated using the first planform as baseline and optimizing the drag with constant lift subjected to 10 m/s and 16.5 m/s freestream velocity, respectively. In this optimization part, airfoil physical thickness allowances are introduced as inequality constraints to the optimization process. For every case, each of the wing planforms are analyzed by a CFD software and tested with load cell measurements for the corresponding freestream velocity. The results of these analyses and experiments are used to extract lift and drag forces for a wide range of angles of attack. Relations between these parameters and drag of the optimized wing planforms

are established in order to validate the optimization code. Final deduction of aerodynamic parameters ensures that the code that has been developed for the optimization of morphing wing planforms for different flight conditions is valid and useful.

Keyword: Morphing Wing, Load Cell Measurement, Optimization, CFD, Aerodynamic Lift, Aerodynamic Drag, Wing Planform

ÖZ

ŞEKİL DEĞİŞTİREBİLEN KANATLARDA KALDIRMA VE SÜRÜKLEME KUVVETLERİNİN HASSAS YÜK HÜCRESİ İLE ÖLÇÜLMESİ

Özkanaktı, Mehmet Harun
Yüksek Lisans, Havacılık ve Uzay Mühendisliği Bölümü
Tez Yöneticisi: Prof. Dr. Serkan Özgen

Mayıs 2015, 118 sayfa

Bu tez, üç farklı şekil değiştirebilen kanat biçiminin ve bir baz kanat biçiminin, başka bir çalışmada geliştirilen eniyileme kodunun doğrulanması amacıyla, ticari hesaplamalı akışkanlar dinamiği kodu ve yük hücresi ölçümleri ile incelenmesinin sonuçlarını sunmaktadır. Bu kanat biçimlerinin incelenmesine duyulan ilgi, eniyileme kodunun kaldırma kuvveti sabit kalmak kaydıyla sürükleme kuvvetini en aza indirmesinden kaynaklanmaktadır. İlk kanat biçimi 14 m/s hız için geometrik boyutlar ve kanat konikliği sınırlamalarıyla eniyileştirilmiştir. Sonrasında diğer iki kanat biçimi ise bu kanat biçimi baz alınarak sırasıyla 10 m/s ve 16.5 m/s hızlarında eniyilenmiştir. Bu safhada kanat kesitinin fiziksel kalınlığının değişimi belirli ölçüler içerisinde eniyileme algoritmasına sınırlama olarak sunulmuştur. Bütün eniyileme senaryoları mutabık akış hızlarında hesaplamalı akışkanlar dinamiği ve yük hücresi ile rüzgar tünelinde test edilmiştir. Bu deneylerin sonucunda kanadın kaldırma kuvveti ve sürükleme kuvveti geniş bir hücum açısı aralığında test edilmiştir. Bu değişkenlerin hesaplanması ile birlikte eniyileme kodundan alınan teorik hesaplamalar

karşılaştırılmış ve eniyileme kodunun doğruluğunun farklı senaryolar dahilinde geçerli olduğu ve güvenilir olduğu ispatlanmıştır.

Anahtar Kelimeler: Şekil Değiştirebilen Kanat Biçimleri, Yük Hücresi Ölçümü, HAD, Aerodinamik Kaldırma Kuvveti, Aerodinamik Sürükleme Kuvveti, Kanat Plan Şekli

To my grandmother Nazmiye

...and my source of pride, my sister

ACKNOWLEDGMENTS

I would like to state my sincere gratitude to all people in my life who have supported me throughout this adventure.

I would like to express my deepest appreciation to the Middle East Technical University for letting my dream of being a student here become true.

My deepest thanks to Kemal Kurdaş for making this infinite steppe green and revolutionizing my studentship years in METU into years in heaven.

My Advisor, Prof. Dr. Serkan Özgen deserves the biggest thank. None of my deepest and sincere thanks would be enough for his contribution to my theses.

I have to state my gratitude to Dr. Sinan Körpe, He is an honorable friend, dear colleague and guide of my undergrad years.

Anatolian Craft (a.k.a. Anatolien Kraft) is a family to me in a place far away from home. They always supported, pushed me further from beyond the best. Emre Yılmaz, Alpay Demircan, Pelin Ergen and Mehmet Ozan Gözcü, knowing you and gathering all of you in a group maybe the best thing I did in my life. You deserve whole life long acknowledgement.

My family, most probably you don't have any clue of what I am doing in this chaos, nevertheless you never stop supporting me. This the reason for why we are calling this "*Daktilo*" among us. Thanks for all your efforts and being there for me whenever I need.

Also, I would like to thank İsmail Calayır, Engin Leblebici, Derya Kaya and Ahmet Kılıç who helped me in this exhausting work.

This study was supported by The Scientific and Technological Research Council of Turkey (TÜBITAK) with the project number 111M731. This support is gratefully acknowledged.

TABLE OF CONTENTS

LIST OF TABLES

TABLES

LIST OF FIGURES

FIGURES

LIST OF SYMBOLS

a.o.a.	(degree)	Angle of attack
b	(m)	Wing Span
B_R	(%)	Uncertainty of a system
C_f		Skin friction coefficient
C_L		Lift coefficient
Cp_{camber}		Camber Control Point of Spline
$Cp_{thickness}$		Thickness Control Point of Spline
c_r	(m)	Root Chord
c_t	*(m)*	Tip Chord
D	(N)	Drag Force
D_F	*(N)*	Skin Friction Drag Force
D_i	(N)	Induced Drag Force
D_p	(N)	Pressure Drag Force
e	(%/mm)	Eccentric load error
F_m	(N)	Measured force
F_R	(N)	Real force
F_x	(N)	Force measurements at x-axis
F_y	(N)	Force measurements at y-axis
F_z	(N)	Force measurements at z-axis
L	(N)	Lift Force
$L_{boundary\ layer}$	(mm)	Boundary layer height
M		Number of data taken
M_m	(N.m)	Measured moment
R		Measurement
$\bar{R}$		Mean of the measurements
Re		Reynolds Number
S	(m^2)	Wing Planform Area
S_R		Standard deviation
T_x	(N)	Torque measurements at x-axis

T_y	(N)	Torque measurements at y-axis
T_z	(N)	Torque measurements at z-axis
U	(m/s)	Freestream Velocity
$u*$		Friction velocity
V_∞	(m/s)	Velocity
W	(N)	Weight
W_R	(%)	Total system uncertainty
x	(mm)	Distance from axis origin point
$X_{lam.\ separation}$		Distance of laminar separation point on chord
$x_{transition}$		Distance of transition point on chord
y	(m)	Wall distance
y^+		Dimensionless wall distance
z		Control points
$\left(\frac{Z}{C}\right)_{up}$		Physical thickness of optimum airfoil
$\left(\frac{Z}{C}\right)_{upinitial}$		Physical thickness of starting airfoil
α	(degree)	Angle of attack
μ	(Pa.s)	Dynamic Viscosity
ρ	(kg/m^3)	Air Density
σ		Standard deviation
τ_ω	(Pa)	Wall shear stress
υ		Degree of freedom

LIST OF ABBREVIATIONS

A/C	Aircraft
AC	Alternating Current
Akaflieg	Akademische Fliegergruppe
Aoa	Angle of attack
CAD	Computer Aided Design
CAM	Computer Aided Manufacturing
CFD	Computational Fluid Dynamics
DARPA	Defense Advanced Research Projects Agency
Eloxal	Electrolytic Oxidation of Aluminum
F/T	Force and Torque
GRGM	Generalized Reduced Gradient Method
MAS	Morphing Aircraft Structure
METU	Middle East Technical University
MFC	Macro Fiber Composite
NACA	National Advisory Committee for Aeronautics
NASA	National Aeronautics and Space Administration
PIV	Particle Image Velocimetry
PLC	Programmable Logic Controller
PWM	Pulse Width Modulation
RPM	Revolution per minute
SMA	Shape Memory Alloy
UAV	Unmanned Aerial Vehicle
USAF	United States Air Force

CHAPTER 1

INTRODUCTION

1.1. Definition of Morphing

For a better comprehension of the concept of morphing wings, etymological background of the "morphing" word should be investigated. According to Merriam-Webster Dictionary, morph originates from Greek word "*morphē"* which means "shape or form". Notwithstanding, meaning of morphing has altered to changing in form, shape shifting or being subjected to transformation from one form to another form gradually when this concept is adapted into aerospace specialized language. This term points out in-flight outer geometry alteration ability of aircraft sections, particularly wings, in order to enhance aerodynamic performance [1].

Although there are numerous mechanisms or techniques on aircraft which are able to change outer shape of aircraft, most of them cannot be defined as a morphing wings. Therefore, the definition of morphing structure on aircraft should be concretized. One of the definitions is expressed in technical documents of DARPA. This definition with geometric designations states that aircraft wings have to radically change their planform via at least 200% change in aspect ratio, 50% change in wing area, and 20 degree change in wing sweep angle during flight to be named as a morphing wing [2]. Another definition of morphing aircraft structures expressed by The Defense Technology Directive is as follows [3] [4]:

> *"Morphing is a capability to provide superior and/or new vehicle system performance while in flight by tailoring the vehicle's state to adapt to the external operational environment and multivariable mission roles. In the context of this DTO, morphing aircraft are multi-role aircraft that change their external shape substantially to adapt to a changing mission environment during flight"*
>
> — (Anonymous 2006)

1.2. Morphing Wing Concept

Contemporary aircrafts are being designed according to Cayley's design paradigm which splits main and side functions of wings in order to keep only functions that are necessary to preserve flight [5]. According to the requirements on the conceptual design of an aircraft, general dimensions are optimized for one flight regime. In most cases, this flight regime would be cruise. The rest of the flight regimes are just transition regions where the aircraft is comparably inefficient since the existing aerospace manufacturing technology forces to compromise all types of the flight regime into one certain geometry with limited shape alteration ability like flaps or slats. The main reason of this insufficiency is the absence of the necessary materials technology as well as the complexity and the weight of the shape shifting mechanism. This can be claimed as a reason why the morphing wing concept emerged. Unlike birds and flying creatures, modern aircraft is not completely capable of transforming their aerodynamic structures into the most optimized shape due to the requirements [5] which are shown in Figure 1-1.

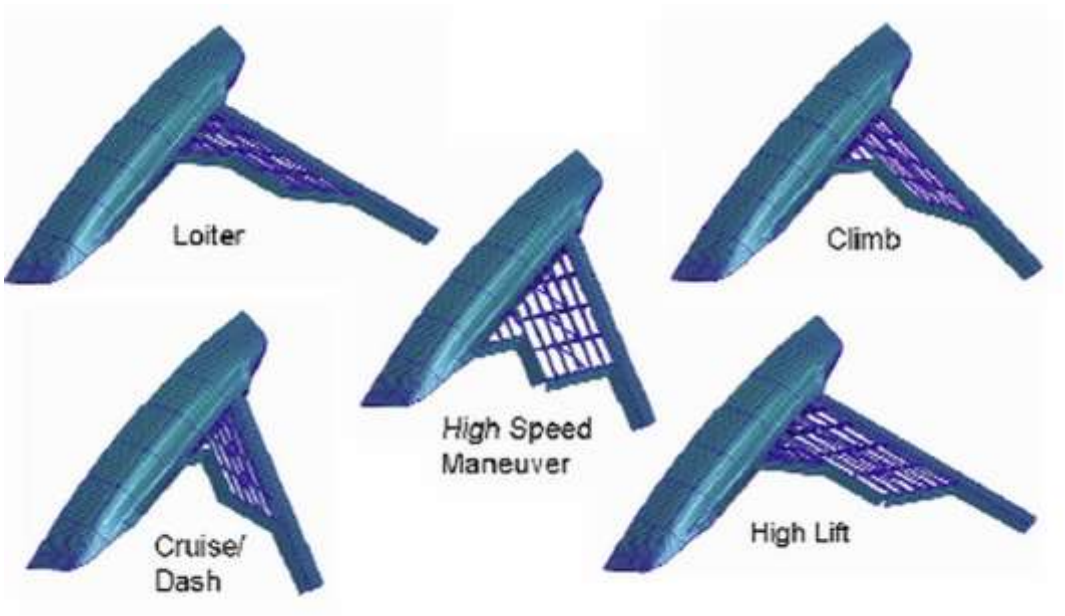

Figure 1-1 Different wing shapes

Besides, morphing wings expand the area of the design space which is comparably narrow because of the aerodynamic limitation of fixed wings seen in Figure 1-2 [7].

Aircrafts with morphing wing capability will be appropriate for several missions and roles.

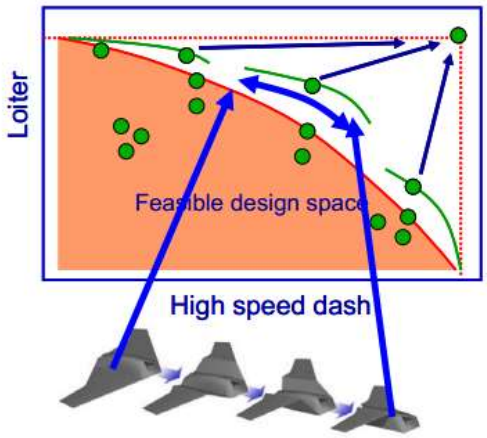

Figure 1-2 Design space area [7]

Modern aircraft is capable of mimicking certain shape transformations through flaps, changing sweep angle and retractable landing gears, which are shown in Figure 1-3. Unfortunately, these morphing mechanisms do not completely satisfy the best performance requirements for all flight conditions. However, they provide comfort in particular flight regimes for which corresponding mechanisms are designed.

Figure 1-3 Discrete morphing mechanisms [6]

Additionally, morphing wing techniques are divided into categories based on their morphing oriented geometric alterations. Although traditional morphing methods, like

retractable landing gears or flaps, enhance aerodynamic performance since they change the outer shape of aircraft, they are ignored in almost all categorizations. The reason for setting these methods apart is not being generic enough to utilize all the forms of morphing. The exemption of the conventional morphing methods is also rationalized with the explanation of these methods. Previously mentioned methods serve only one functionality and performs only for a limited time period within the whole flight. This is the main reason for exemption from almost all morphing wing categorization according to the numerous authorities. Nonetheless, traditional morphing methods can be categorized as discrete morphing, while morphing wings with generic transformation ability, are named as continuous morphing [6]. Table 1-1 also expresses the categorization of morphing concepts with reasons and examples.

Table 1-1 Categorization of morphing wing

Discrete Morphing	**Continuous Morphing**
Flaps, Slats, Ailerons, Retractable Landing Gears, Variable Sweep Wing, Variable Span	*Wings of birds, SMA wings*
Singular Functionality	Multiple Functionality
Locally placed	Placement may be all over the body
Short period utilization	Whole flight utilization

1.3. Historical Aspects of the study

The ancestors of manned flight attempted to glide or fly controllably in air with heavier-than-air vehicles. The main inspiration of these efforts originated from the nature; especially the flying creatures. Furthermore, the forefathers of aviation observed these flying creatures in detail and tried to imitate them in order to achieve the perfect and most efficient flying machine. Unfortunately, they have never succeeded in copying nature entirely, especially in terms of imitating deforming wings of birds dependent on flight condition due to the inadequacy of technological advancements. Nevertheless, numerous attempts were performed in order to achieve

the best controlled flight, and the infrastructure of all of these attempts were based on flying creatures like birds and insects.

Historically, the first attempt for manned flight was the design of an ornithopter by Leonardo da Vinci in 1488 [8]. In the sketches of Leonardo da Vinci, the imitations of bird wings and the resemblance with wing skeleton form are clearly seen [9].

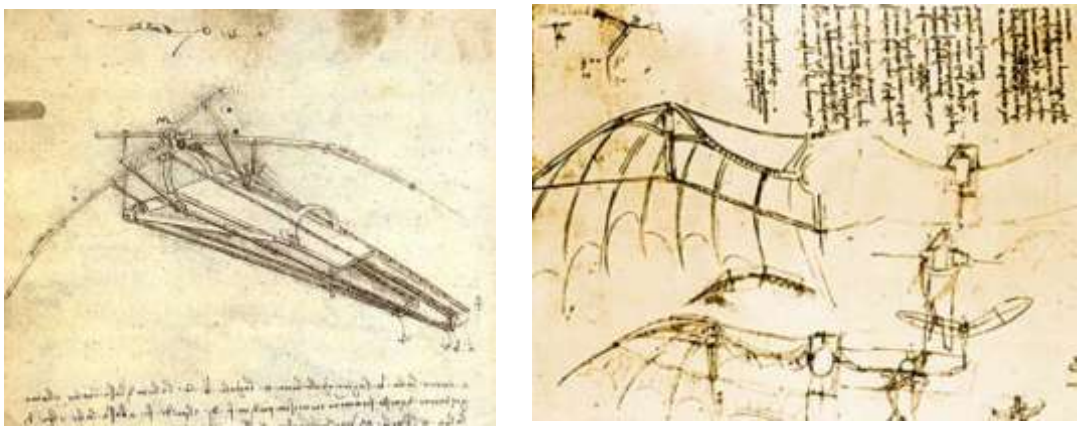

Figure 1-4 Leonardo da Vinci's sketches [9]

As the first attempt, the whole aircraft design with morphable wings was introduced in 1890 by a French inventor and enginner Clement Ader as seen in Figure 1-5. Ader's flying machine named "Eole" was able to change its wing shape during the flight. Clement Ader offered several different aircraft concepts but there is no assertion about whether his designs flied [10].

Moreover, Clement Ader's sayings and his other design sketches clearly expressed his aeronautical engineering philosophy that "Every aircraft should be morphable and retractable." [7].

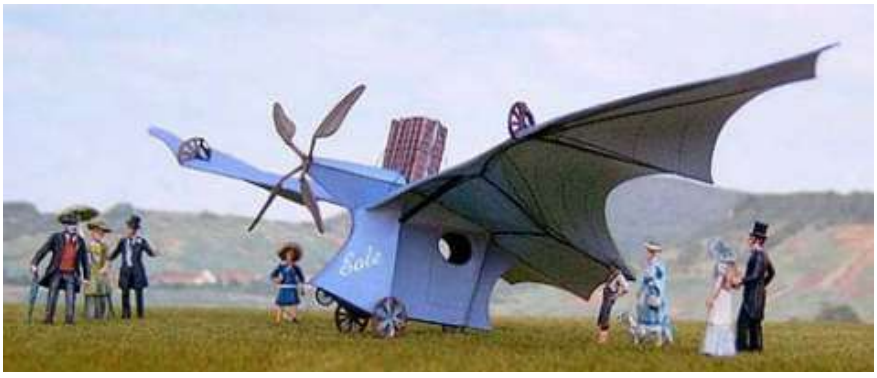

Figure 1-5 Clement Ader's Eole – A morphing wing concept in 1890 [10]

In 1899, Wright brothers came up with the breakthrough concept which improved the control of the airplane and helped to overcome the adverse yaw effects. Their elegant concept included cables, placed over the wings in order to create twist on wing planform. This recently unveiled wing warping concept became a brilliant solution to maneuvering capability of aircraft. In addition, they placed a vertical rudder in order to overcome adverse yaw effects generated by asymmetrical spanwise load distribution on the wing due to wing warping. This rudder mechanism was also connected to their control system with cables. These breakthrough concepts are accepted as the most important contribution of Wright Brothers to the aviation industry by some aviation authorities [11] [12] [13] [14]. In Figure 1-6, the schematic of this breakthrough concept is shown.

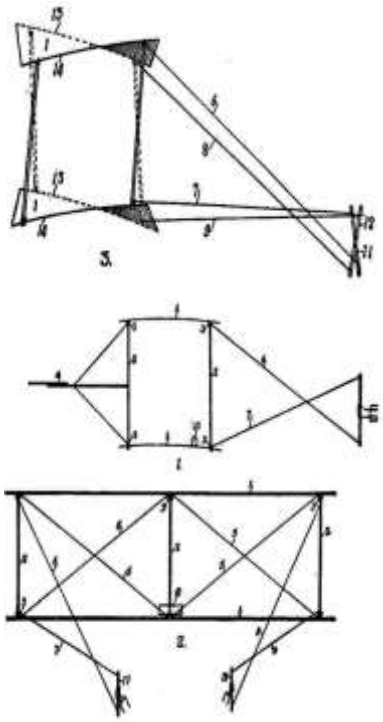

Figure 1-6 Wright Brother's wing warp kite [14]

Subsequently, aircraft wings with morphing capability were initially designed utilizing mechanical shape changes rather than the elasticity of materials. At the time, the nature of materials were inadequate to deal with the complexity of systems and the extra energy requirement to have minimal shape alterations.

Taking these aviation trends into consideration, Geoffrey Terence Roland Hill and Ivan Makhonine came out with two different aircraft concepts in different countries at

the same time. Pterodactyl IV was designed by G.T.R. Hill in the United Kingdom and it had variable sweep ability ranging from 4 to 75 degrees. MAK-10 also referred to as MAK-101 was a design of Soviet engineer/inventor Ivan Makhonine and this particular aircraft had telescopic wings which were able to extent its span from 13 meters to 21 meters. Surprisingly, both of the aircrafts were flown successfully in 1931[7]. Figure 1-7 and Figure 1-8 indicate photos of Pterodactyl and MAK-10, respectively.

Figure 1-7 Pterodactyl variable sweep wing.[7]

Figure 1-8 MAK-10 telescopic wing [15]

Furthermore, another morphing wing aircraft was developed by Baksaev in 1937. Baksaev LIG-7 (Figure 1-9) had a unique morphing wing mechanism with a fixed wing and six 50 cm wide sliding airfoils over the fixed wings. These sliding airfoils were able to extend 2/3 of the wingspan from fuselage by using tensioned steel wires operated from cockpit. In addition, a significant increase in performance was observed during take-off and landing as a result of the extended airfoils without any handling nuisance [7].

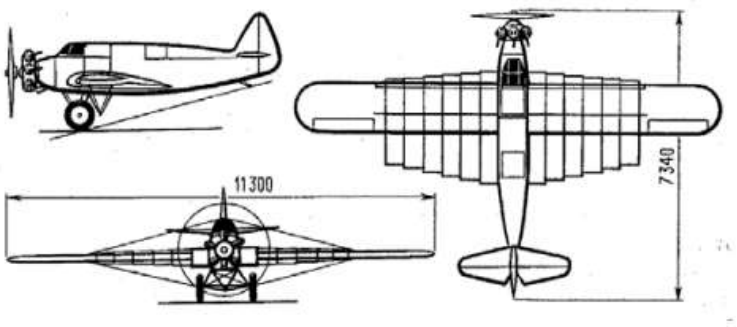

Figure 1-9 Bakshaev LIG-7[7]

In 1950, NACA put forward an experimental design aircraft named X-5 inspired by the Messerschmitt P-1101. However, X-5 had in-flight sweep changing ability. This would be the first aircraft to possess the ability to do this particular alteration. X-5 was able to sweep its wing up to 60 degrees. Besides, X-5 had a mechanism to adjust hinge and pivot position while wing sweep could be changed to overcome the effects by the center of gravity and center of pressure position changes. Although the first few test flights of X-5 were successful, X-5 was retired in 1955 due to fatal spin-stall characteristics. Although X-5 had design flaws, it can be claimed as a successful aircraft that served its purpose because of the experimental data attained from its early testing. Inflight variable wing sweep principles were indeed extracted thanks to this aircraft [16].

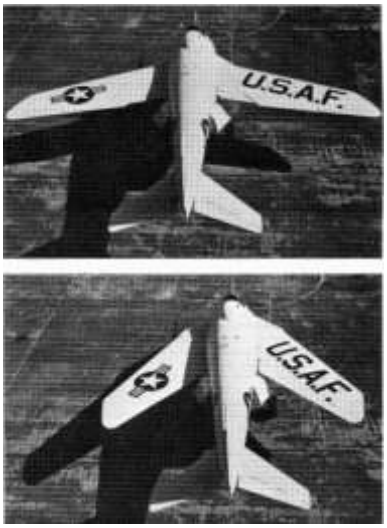

Figure 1-10 Variable sweep wing aircraft: X-5[16]

X-5 can be named as the forefather of modern variable wing sweep aircrafts since X-5 led the fighter aircrafts F-111 and F-14, and bomber B-1 by knowledge gathered from experiments during its design and tests [7]. F-111 is the first mass produced aircraft with variable wing sweep configuration and remained active until 2010 [17]. Figure 1-11 shows the top-view of F-111 with one wing folded and the other open. Within the same time interval, different aircraft manufacturers followed the similar variable wing sweep configuration such as fighter-bomber Tupolev-17 in 1965, supersonic bomber Tupolev-22 (Figure 1-12) in 1969 and fighter MIG-23 in 1967 from Soviet Union, Dassault Mirage G in 1964 from France [18] .

Figure 1-11 F-111 Different sweep orientation [19]

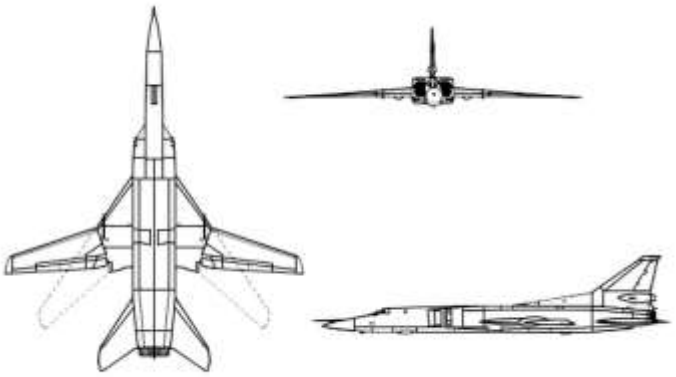

Figure 1-12 Tupolev-22 variable sweep bomber [20]

Dissimilar to 1960's aircrafts, USAF offered a new concept of morphing aircraft named XB-70 in 1964 which is shown in Figure 1-13. This concept included three dimensional wing morphing. XB-70 could change dihedral orientation of its wings by rotating outer wing section according to flight speed.

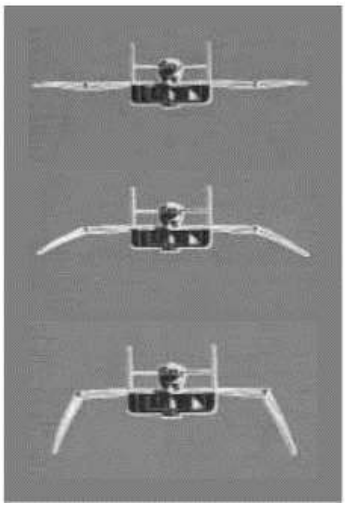

Figure 1-13 XB-70 Bomber [7]

Morphing wing technologies were implemented into not only military aviation but also civil aviation projects. Polymorphing and variable geometry concepts also drew attention in civil aviation with features such as increasing efficiency or quality of flight. In details, German Akaflieg Association designed and manufactured FS-29 glider which had an ability to extent its wing span in order to improve the gliding performance. The telescopic wing on FS-29, which is shown in Figure 1-14, provided performance increase in soaring in distance/speed competitions with extended and retracted wing configurations [21].

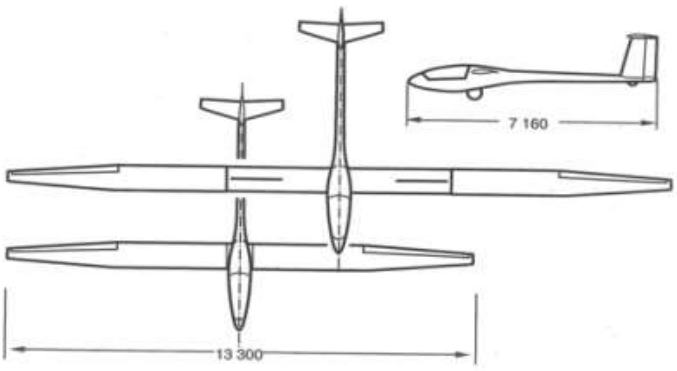

Figure 1-14 FS-29 planform geometry and side view [7]

In time, these aerodynamic performance enhancements were used by aerospace companies mostly planned for utilization for usage in the field of unmanned air vehicles. The enhancements in technology make possible to manufacture electronic equipment, sensors and actuators lighter and smaller as well as smart materials like shape memory materials. Therefore, a significantly increasing number of researchers are nowadays quite interested in morphing wings [22]. Therefore, opposed to the past, contemporary morphing wing concepts are being implemented on unmanned aerial vehicles rather than manned aircraft. The reasons for this are, (i) using UAVs (Unmanned Air Vehicle) for morphing wing implementation is comparably easier and (ii) it diminishes the risk of loss of human life during the tests. Moreover, losing UAVs are more acceptable from this point of view.

Defense Advanced Research Projects Agency, DARPA, commenced and funded morphing aircraft technology program in January 2003. This program aimed to design and produce morphing capable wing and geometry structures within 2.5 years. After the bidding process which was held on April 2002, three contractors stood out amongst other competitors which were Lockheed-Martin, Hypercomb/Nextgen and Raytheon Missile Systems. The first phase of this program lasted for 12 months and the corresponding mission was developing a morphing system with transition ability that was completely different from conventional wing structures [7].

Each contractor conducted intense work in order to satisfy requirements of range and loiter of Hunter-Killer Unmanned Aerial Vehicles or Cruise Missiles. Hypercomb/Nextgen party of the program created a design that was capable of altering its planform shape. This design, which is shown in Figure 1-15, allowed reduction of chord length by extending the span as a result of increasing aspect ratio for the loiter flight regime. It also allowed the reduction of wing area by increasing sweep angle and lowering aspect ratio for dash mission.

Figure 1-15 Nextgen aeronautics' design of the morphing wing [23]

Lockheed-Martin proposed a foldable wing concept for different flight regimes as can be seen in Figure 1-16. Advanced skin material was used in order to perform as morphing wing while maintaining the seamless outer contour. In this way, keeping skin friction at low levels could be achieved.

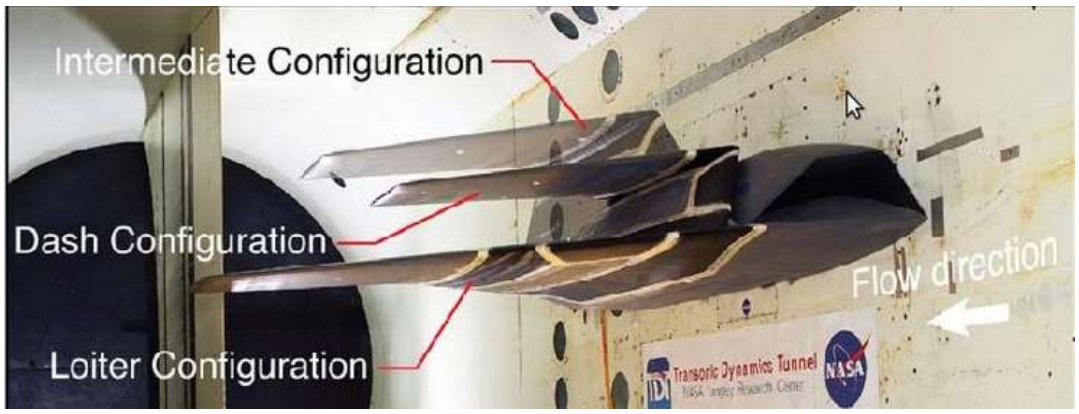

Figure 1-16 Overlapped photograph of Lockheed Martin MAS wind tunnel model during morphing [24]

Dissimilar to other parties of the program, Raytheon generated a telescopic wing design for cruise missiles which is represented in Figure 1-17. This telescopic morphing wing aimed at enhancing range and cruise capability; however, this design encountered problems in overcoming large wing loading values as a result of insufficient available volume for the morphing mechanism [7].

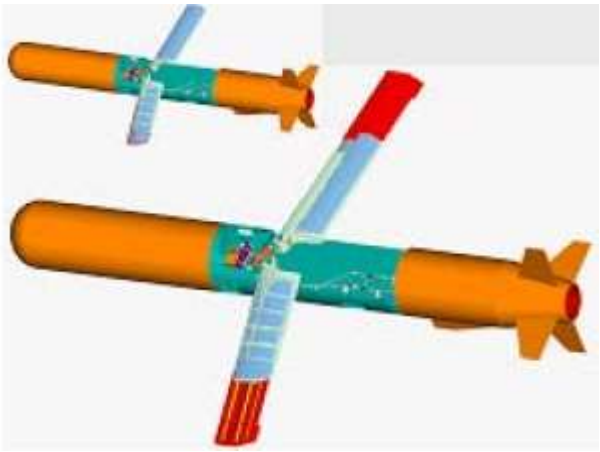

Figure 1-17 Raytheon morphing wing design [7]

1.4. Review of Literature

In recent years, academic research and industrial works in the field of morphing wing have increased dramatically due to the possible future contributions to the flight efficiency. Therefore, the purpose of most studies in this specialized literature is to design a shape shifting mechanism or to develop smart materials with shape shifting ability and shape memory capability.

Poongson et al. [25] conducted research on the design of a variable camber concept. This design comprised of six chordwise rib sections and each of these sections had its own center of rotation in order to change camber orientation as seen in Figure 1-18.

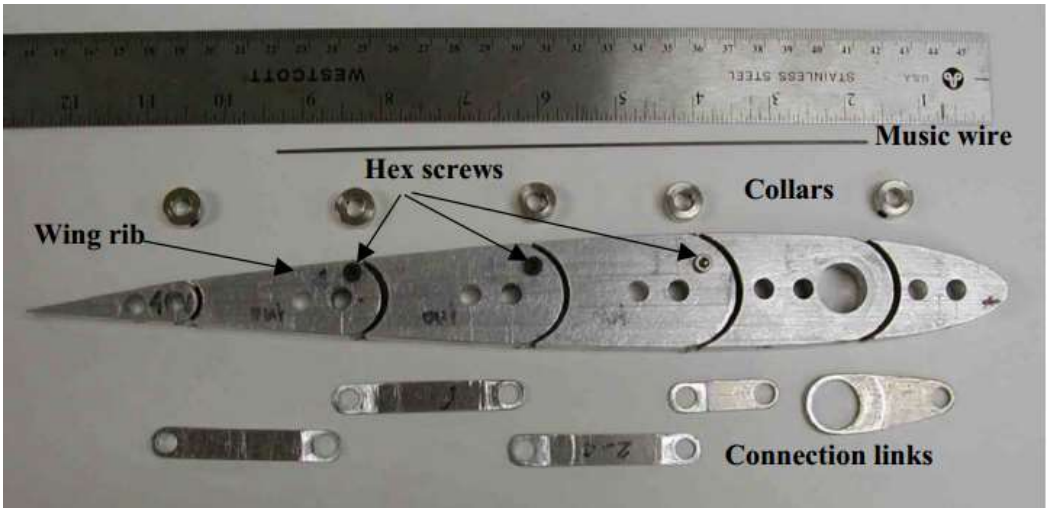

Figure 1-18 Rib of the multi-section variable camber wing [25]

Elastic materials and special coverings are used for a shell covering. When the camber of airfoil changes, its circumference length also changes. This is the reason why Poongson et al. used elastic latex material where only two rib sections met as can be seen in Figure 1-19. Actually, in this dissertation, some aerodynamic improvement was granted. However, measured improvements were not quite reliable due to manufacturing and covering defects. Nevertheless, this work was acceptable in terms of investigating morphing wing mechanism.

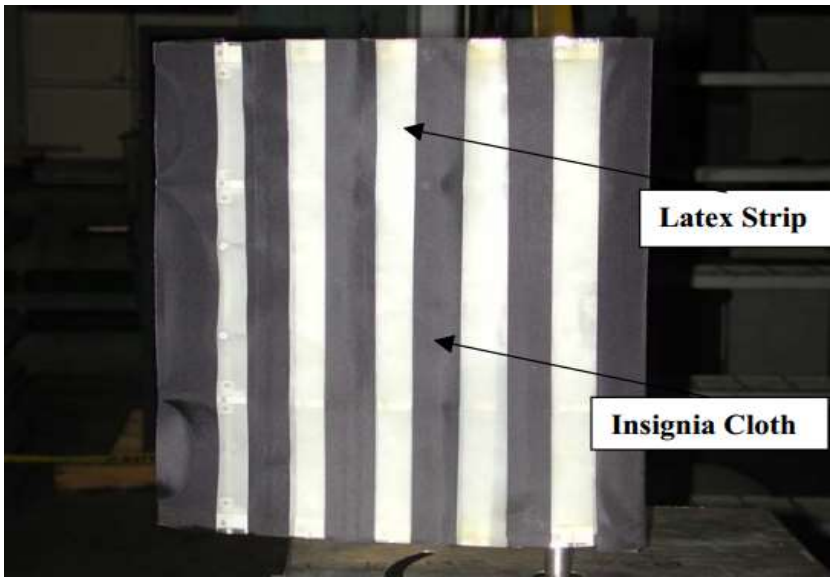

Figure 1-19 Wing with skin [25]

Another camber optimization aimed work was the morphing wing mechanism proposed and researched by Boria et al. [26]. They presented extraordinary study using instantaneous wind tunnel data in order to optimize the camber line. In this work, two different electro-mechanic (servo actuator) systems were used. One of them was located at 21% of the chord in order to change camber positively. The other one located at the trailing edge was responsible for changing camber negatively. Above mentioned mechanism is displayed in Figure 1-20.

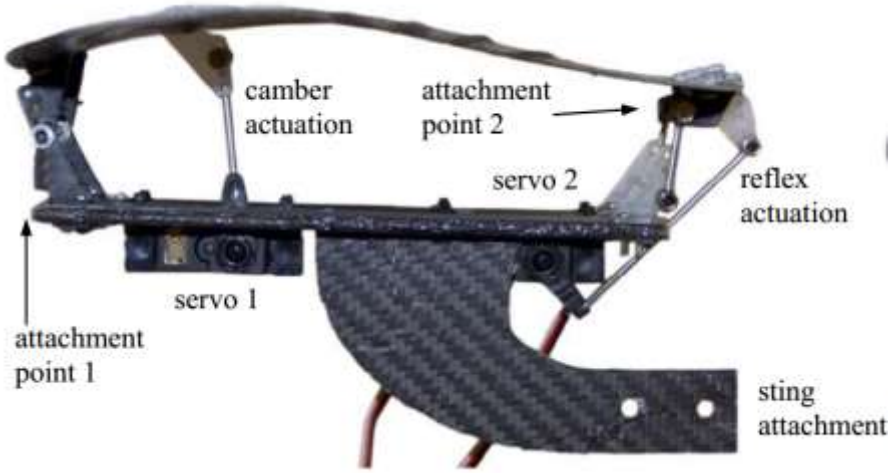

Figure 1-20 Two-design-variable morphing Zimmerman wing [26]

For every angle of attack in the experiment, lift-to-drag ratio of optimized airfoil was increased up to 50% percent as shown in Figure 1-21.

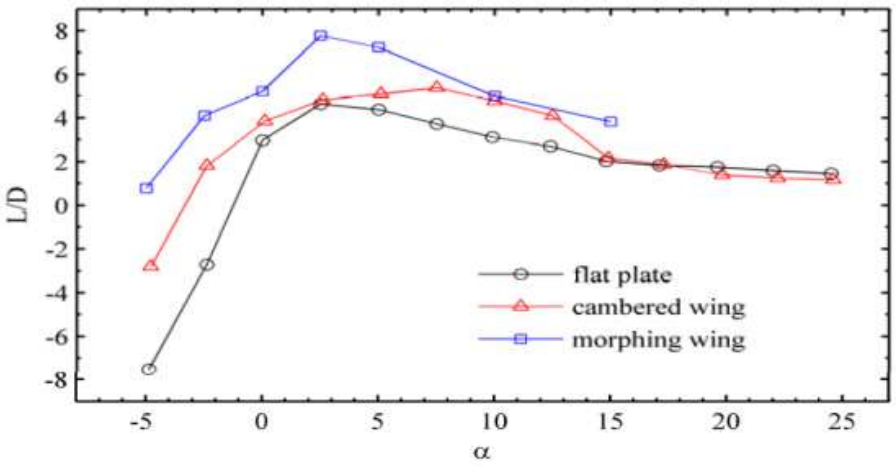

Figure 1-21 Morphing wing L/D performance versus cambered wing and flat plate [26]

Sakarya et al. designed and manufactured an open section hingeless control surface that was able to increase or decrease the camber as shown in Figure 1-22 and Figure 1-23. Servo actuator, rods and thin metal sheets were used in order to provide the elasticity of the adaptive section [27]. Also, servo actuator force and the responsive deflection of trailing edge were analyzed profoundly in this thesis.

Figure 1-22 Hingeless control surface: increased camber [27]

Figure 1-23 Hingeless control surface: decreased camber [27]

Bilgen et al. presented a morphing wing concept where wing section altered its shape with the help of piezoelectric equipment. Macro Fiber Composite (MFC) was used in the study because of its structural flexibility and physical allowance specifications. The design included two active bimorph actuators, which were respectively at the top and at the bottom of the airfoil section [28].

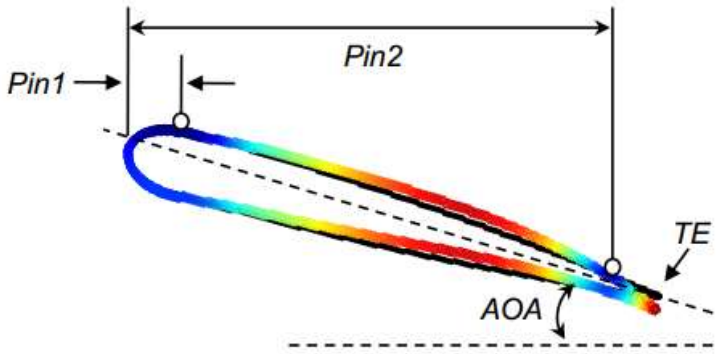

Figure 1-24 Exaggerated presentation of airfoil. Actuated and non-actuated states [28]

In order to obtain analytical results, MATLAB based program and XFOIL were used. XFOIL was utilized to calculate the aerodynamic parameters such as lift, drag and the pressure distribution. Optimum lift and lift-to-drag configurations were obtained using

Matlab based programs which used XFOIL iteratively in order to find the most optimized configuration [28].

In conjunction with this study, Bilgen et al. carried this concept a step further by manufacturing this particular wing. Bimorph materials and unimorph benders are used in order to achieve shape alteration as shown in Figure 1-25 [29].

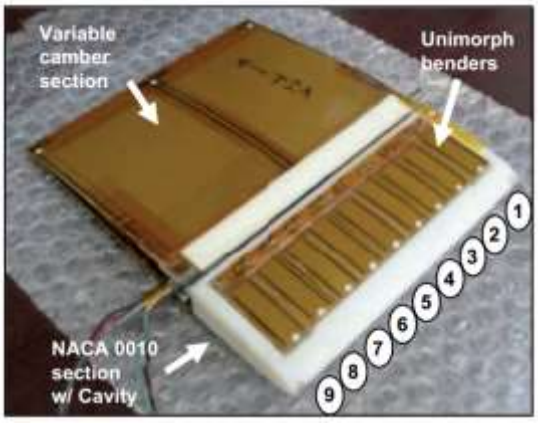

Figure 1-25 Variable Camber Airfoil with morphing materials [29]

The outcomes of this experiment proved that there is important increase in terms of lift under the proper distribution of the excitation conditions. Results showed that the lift coefficient was increased by 18.4% at 5 m/s flow speed [29].

Aside from camber morphing, telescopic morphing wing – a very common concept- was studied by Blondeau et. al. A pneumatic powered inflatable telescopic spar mechanism concept was developed in order to extend wing span by sliding a section of wing to outside [31].

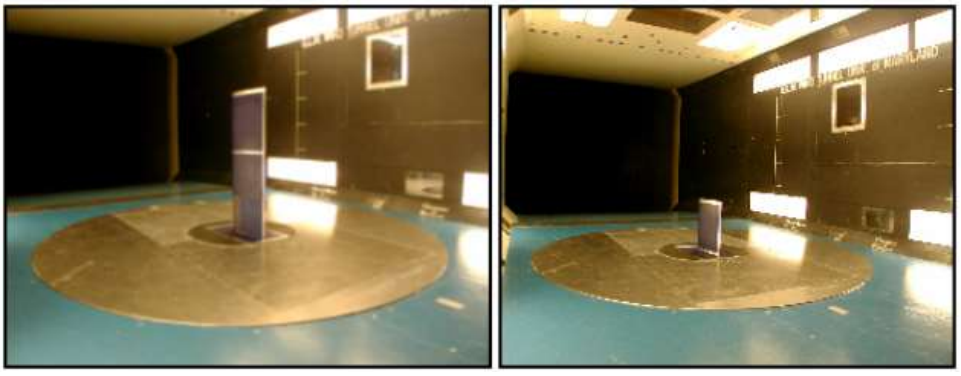

Figure 1-26 Pneumatic Telescopic Wing extended and retracted configuration in wind tunnel [30]

Blondeau et al. conducted numerous wind tunnel tests to compare fixed wind, telescopic wing in retracted and extended version in terms of aerodynamic parameters. As expected, extended morphing wing had higher lift-to-drag ratio with respect to the retracted wing. By contrast, extended wing had lower lift-to-drag ratio compared to fixed wing, even though the aspect ratio and airfoils were the same. The reason of this issue could be explained by the interference and the parasite drag occurring as a result of telescopic wing mechanism and the imperfections on the surface [30].

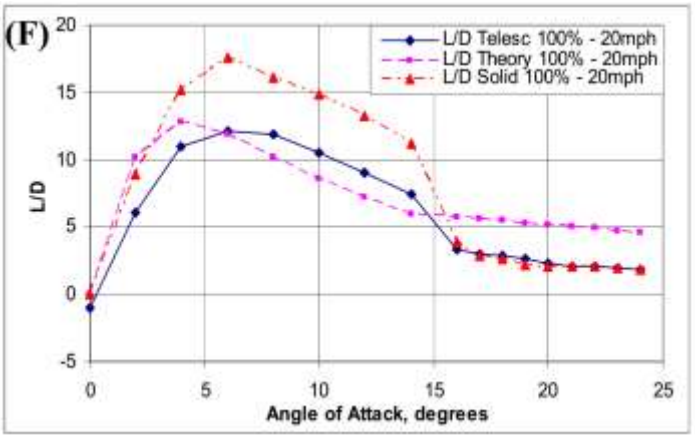

Figure 1-27 Aerodynamic results for wing comparison [30]

Neat et al. proposed a morphing wing mechanism in 2004. This morphing wing mechanism had the capability to shift sweep angle between 0 to 40 degrees, to alter span length between 17 inches to 24.5 inches and to control twist within -20 and 20 degrees. In addition to this system, there was also tail contraction/extension system that operated individually. All these mechanism are illustrated in Figure 1-28. This concept was designed for experimental aerodynamic studies and inflight control analysis of morphing wings. Also, center of mass location changer was integrated to the system in order to overcome instability effects originating from increasing the sweep angle [32].

The experimental results indicated that variable planform capable aircraft was superior in terms of stability and aerodynamic parameters. Increasing sweep angle makes the contour of the drag polar better than the zero degree sweep angle as shown in Figure 1-29. Also, low drag was maintained for a vast spectrum of lift coefficient values. As

a result of these experiments, sweep and span changes were proved to be advantageous [32].

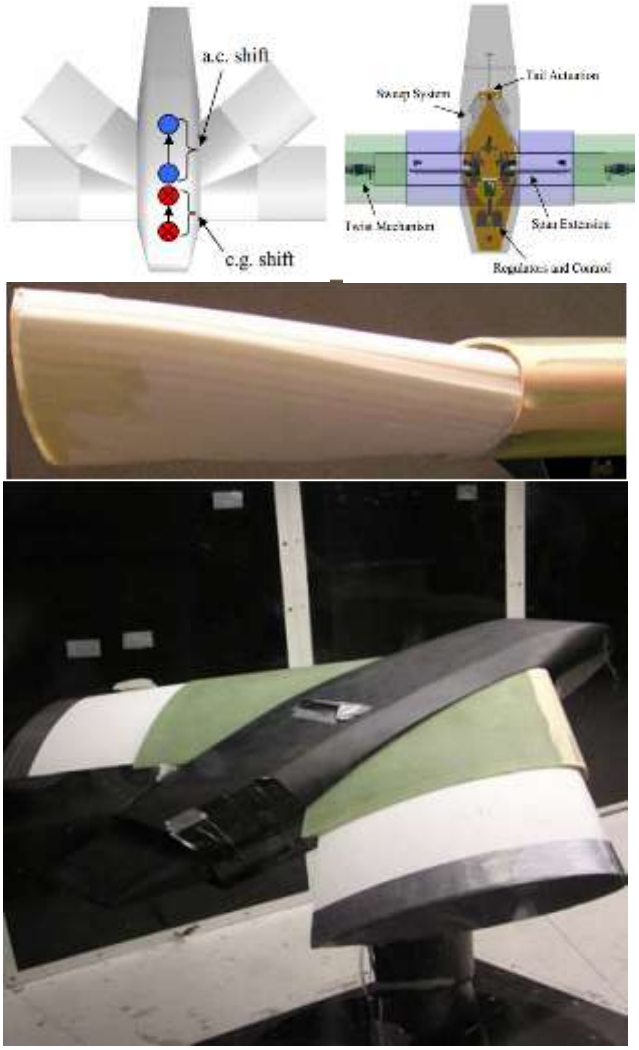

Figure 1-28 CG shift demonstration (top left), wing morphing mechanism actuators (top right), twisted wing tip (middle), model mounted in wind tunnel

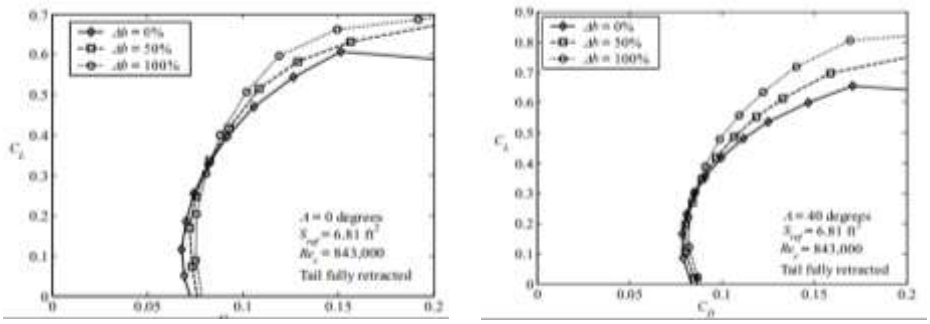

Figure 1-29 Drag polar graphs for different sweep angle [32]

Gamboa et al. presented a study on morphing wing design. This design concept included variable chords, span and airfoils. These mechanisms were required for their research interest which was the optimization of drag values within a desired range of freestream velocities of UAVs. The chord extension mechanism, shown in Figure 1-30, had also side benefits such as changing its airfoil thickness at particular control points, owing to its mechanical design.

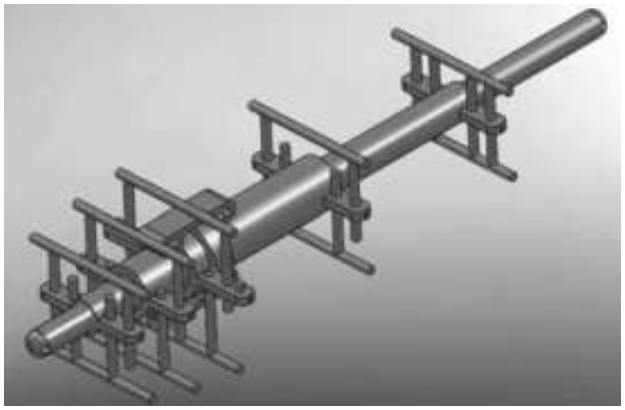

Figure 1-30 Chord extension mechanism [33]

Preserving even intermittency of ribs and stretching outer skin of the wing were aimed while spar extension mechanism was designed. This purpose was achieved by carrying spars outside the fuselage and mechanism rigidity of the spar was maintained as represented in Figure 1-31. In addition, rubber was used as skin material for covering this mechanism because of its high elasticity [33].

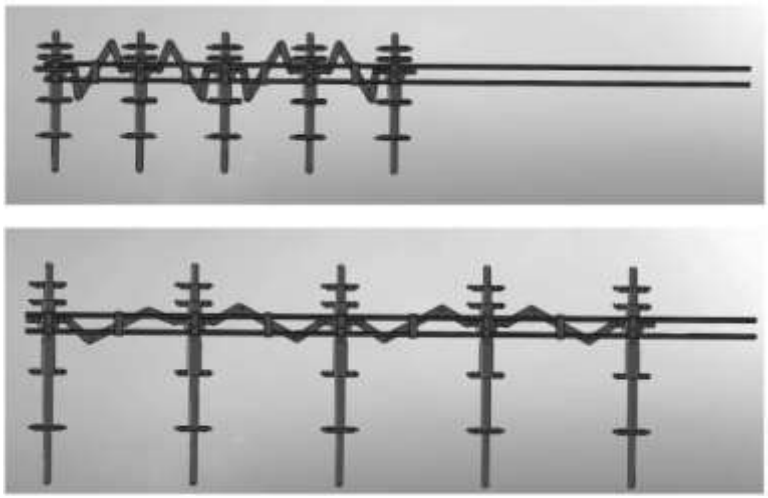

Figure 1-31 Spar extension mechanism [33]

In this work, XFOIL was used to analyze the optimized airfoil in order to gather aerodynamic parameters such as drag and lift forces. As a result of the optimization work, optimized airfoil and planforms were analyzed numerically by the XFOIL tool. Every optimized wing at specified freestream velocities yielded lower drag forces when compared to the corresponding non-morphing wing planforms as seen in Figure 1-32 [33] .

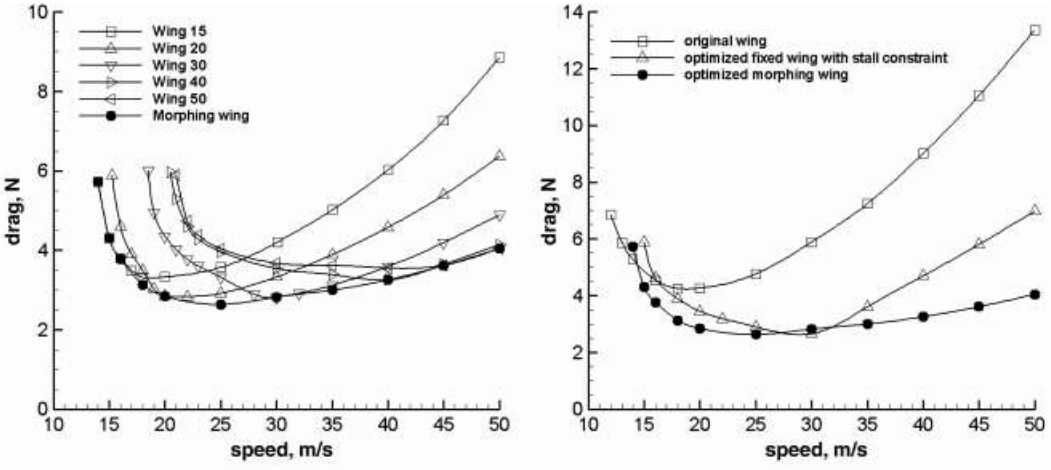

Figure 1-32 Drag results of morphing wing [33]

1.5. Objectives of This Study

In this study, aerodynamic loads are investigated on a baseline wing and optimized morphing wings at different velocities at steady level flight by using loads cells and computational fluid dynamics (CFD). Theoretical aerodynamic results are obtained from an aerodynamic design tool that also obtains the optimum airfoil and planform shape for morphing wings [34]. The aerodynamic design tool uses 3-D panel method and 2-D boundary layer solver in order to determine lift and drag values. The optimization tool uses generalized reduced gradient method for the minimization of the objective function, which is drag, in the presence of behavior constraint, which is steady level flight, and geometric constraints, which are airfoil thickness, span length, root chord and tip chord. Design case within scope of this thesis, is initialized with obtaining an optimized fixed wing for 14 m/s for a mini UAV (Unmanned Air Vehicle) that has a weight of 5N. This wing is accounted as the morphing wing putatively at 14

m/s because it is assumed that morphing wing system is installed into this wing. The airfoil for the process is designed as very close of NACA 4412 airfoil (not NACA4412) and the planform values are 0.6 m, 0.06 m, and 0.06 m, for span, root chord and tip chord, respectively. Then, this wing is processed for optimization at 14 m/s freestream velocity and then used as the baseline wing planform for the optimum morphing wings for 10 m/s and 16.5 m/s at steady level flight. The comprehensible chart of the routine can be seen in Figure 1-33. In this optimization part, airfoil physical thickness allowances are introduced as inequality constraints to the design process. In addition to the optimization constraints, the first optimization of baseline wing has almost no constraint limitations except the physical dimensions of wind tunnel. However, the optimization process of the baseline wing to morphing wings at different velocities has strict constrains due to proposed hypothetical yet realistic morphing wing mechanism.

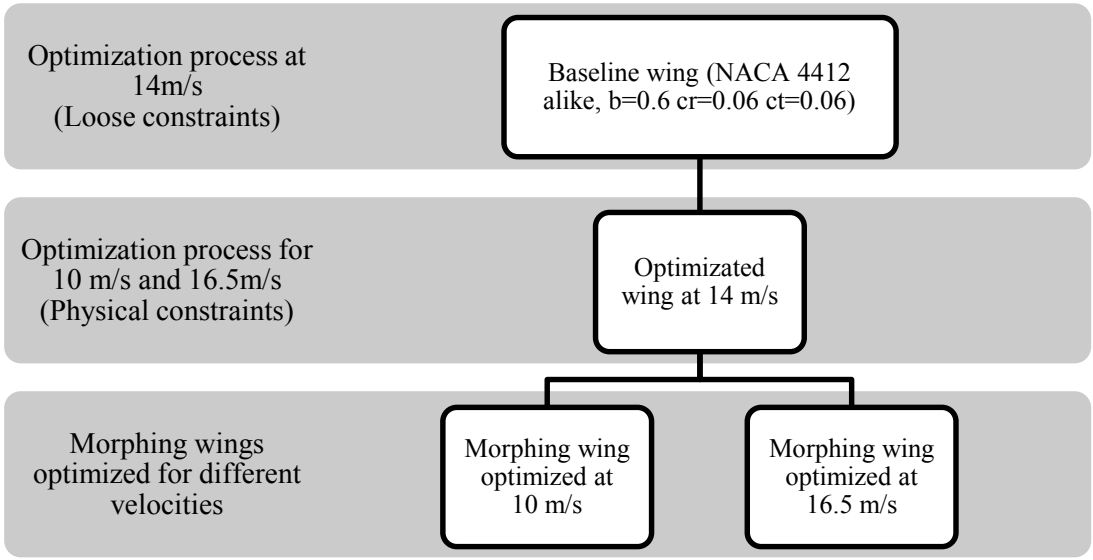

Figure 1-33 Routine of theoretical optimization processes

Furthermore, for different flight conditions, each of the wing planforms are analyzed by a commercial CFD software –FLUENT- and tested with the 6-axis load cell system for the corresponding freestream velocity. The results of these experiments are used to extract parameters which are total lift and total drag. The relationship between these parameters and the drag of the optimized wing planforms is established in order to validate the optimization code. The fact that the main contribution to drag at low Re numbers is the induced drag renders this effort worthwhile. The final results for

aerodynamic parameters are expected to ensure that the code that has been developed for the optimization of morphing wing planforms for different flight condition are valid and useful.

This thesis contains five main sections. First chapter incorporates etymological and aerospace specialized language definition of morphing. Besides, historical background of morphing and former or ongoing research on morphing are introduced. Finally, the first part of thesis is concluded by declaration of brief summary.

Within the second chapter of this study, experimental procedures are discussed in general. The experimental setup, equipment and measurement techniques are cited in detail. Wind tunnel technical specification and characterization are stated. Also, test equipment such as, manufactured wing, load cell system, balance and angle of attack plate and data acquisition software are discussed in this chapter.

In the third part, the modelling and results of the commercial software CFD analysis are introduced.

For the fourth part, the results of the experimental works are presented. The entire data of measurements from the experiment are processed by data and post processing techniques. Then, the meaningful data are displayed by graphics and tables. Meanwhile, measurement errors are discussed in order to enhance data validation.

Subsequently, the final segment of this work contains the essence, the analysis and the comparison of the measurement results with outcomes of the aerodynamic design tool.

CHAPTER 2

EXPERIMENTAL SETUP AND MEASUREMENT DETAILS

In this part of the thesis, experimental procedure is discussed in detail. Wind tunnel specifications and calibrations are also explained in particulars. Besides, wing models which are intended to be used in the wind tunnel experiments are disclosed in every aspects such as design concerns and manufacturing.

2.1. Wing Models for the Experiments

2.1.1. Wing Planform Design

The wings are designed by using the design tool that is developed separately from this work. The design tool offers more stable preliminary design outcomes for morphing wings by depending on a finite wing data. Three dimensional panel method is used in order to gather lift, induced drag and pressure drag. Besides, skin friction is calculated by using two dimensional laminar model of Thwaites and turbulent boundary layer model of Head. In addition to this, transition prediction is done by embedding the e^n method. As a consequence of these calculations, the constituents of total drag for subsonic incompressible flow are aggregated. Also, empirical correction functions are used in order to add the effect of separation point to lift and drag. For this particular design tool, gradient based optimization method named generalized reduced gradient method (GRGM) is used. Subsequently, this design tool is coded by using FORTRAN programming language [34].

In this study, drag optimization is intended for different freestream velocities by changing airfoil and planform parameters. Each wing planform is optimized for minimizing drag by keeping produced lift constant for a particular velocity. Optimization outcomes for each velocity is assumed as an instantaneous configuration of a morphing wing for its corresponding velocity. Realistic but hypothetical shape

shifting mechanism is assumed. This mechanism can transform an instantaneous wing optimized for certain velocity into another instantaneous wing optimized for another velocity. The shape shifting mechanism allows 10% alteration of y coordinate in airfoil geometry and 20% change in span as well as alteration at chord length along the spanwise within the given conditions. Therefore, in order to produce hypothetical

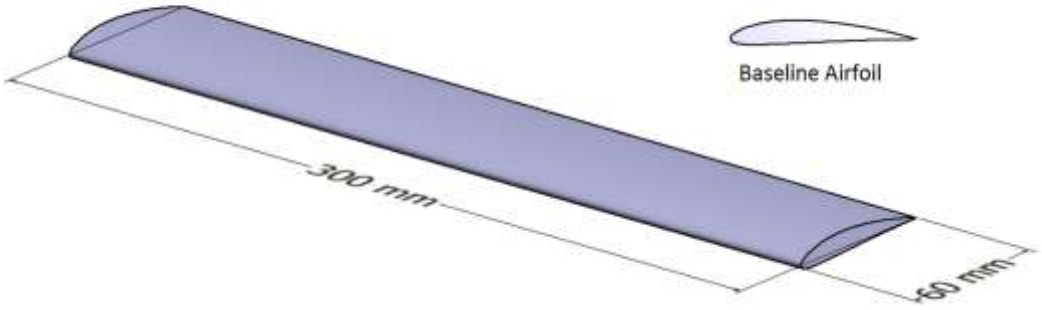

Figure 2-1 Airfoil and planform of baseline wing

shape shifting mechanism, instantaneous forms of morphing wing have to be investigated separately due to the inadequacy in technology of manufacturing and material capabilities

In order to make this study more applicable, a case is chosen by taking the capability and dimensions of wind tunnel facilities, and realistic approaches to presumptive shape shifts of morphing wings into consideration. For this reason, wing planform with an airfoil highly resembling NACA 4412 airfoil, 60 millimeters of tip and root chord and 300 millimeters of half span (Figure 2-1) is designated as the baseline wing in order to provide an initial point to the design tool. Baseline airfoil could not be designated as the NACA4412 airfoil since the spline method of the optimization tool used is not capable of reproducing NACA4412 airfoil exactly. These dimensions and constraints of the optimization tool are determined by considering the wind tunnel test section dimensions. Half span of the baseline wing is designated as half-length of test section length to observe the effect of wing tip vortices, because the main contribution to drag for such low Re numbers is the induced drag. In other words, the development of wing tip vortices are not desirable to interfere with the walls of the test section.

After baseline wing planform is finalized, the design tool optimized the baseline wing for 14 m/s freestream velocity. This wing has become the new baseline wing for the morphing wing platforms which are to be optimized at different freestream velocities with physical thickness constraints. These velocities are determined as 10 m/s and 16.5 m/s by taking wind tunnel maximum flow velocity into consideration.
Furthermore, (i) only planform, (ii) only airfoil and (iii) both airfoil and planform optimization alternatives are available within the design tool. Among these three optimization alternatives both airfoil and planform optimization is selected since it is the most effective. The following optimization works are conducted by using sea level conditions.

In order to prevent ambiguity originating from the nomenclature of the wings, products of the optimization runs are named. Outcomes of the optimization code are referred to as in Table 2-1 hereafter.

Table 2-1 Nomenclature of the wings

Details of the process	Naming
Baseline Wing	Base
Optimized wing for 14 m/s	O14
Morphing wing optimized for 16.5 m/s	M16.5
Morphing wing optimized for 10 m/s	M10

2.1.1.1. Optimization of Wing Planform at 14 m/s

Baseline platform with NACA 4412-like airfoil, is optimized for both airfoil and planform under pre-specified constrains. Eight constraints are represented in Table 2-2, which includes root chord, tip chord, half span, “Cpthickness / Chord”, “Cpcamber / Chord” and transition position constrains. Furthermore, the mean spline of the airfoil geometry is restrained by “Cpcamber / Chord” parameter, and the thickness of the airfoil is controlled by “Cpthickness / Chord” parameter. In details, parameters starts with Cp is the control point of the corresponding curve like thickness and camber distribution and these control points are able to move only in the z-

direction of the Figure 2-2 by the moving of these mentioned control points contour of the particular airfoil takes shape. Airfoil shape is generated by using the b-spline method, which uses the first 8 points for thickness generation at 1.0c, 0.95c, 0.8c, 0.5c, 0.2c, 0.05c, 0.001c, 0c and uses the remaining 7 points for camber generation at 1.0c, 0.95c, 0.8c, 0.5c, 0.2c, 0.05c and 0c.These control points are represented in Figure 2-2. The last control point of the thickness distribution is used to defining leading edge radius [34]. Results of the optimization process are demonstrated in Table 2-3. Planform and airfoil contours are represented in Figure 2-3 and Figure 2-4, respectively. Notice that the optimized planform is highly tapered, has an increased span and planform area compared to the baseline wing. Also, the optimized airfoil is thinner but has more camber compared to the baseline wing.

Table 2-2 Constraint limits for optimization at 14 m/s

Name of the constraints	Lower limit	Upper limit
Root Chord (m)	0.04	0.1
Tip Chord (m)	0.04	0.1
Half Span	0.24	0.36
$Cp_{thickness}$ / Chord	-1.0	1.0
Cp_{camber} / Chord	-1.0	1.0
$(\frac{x_{transition}}{c})_{mean}$ or $(\frac{x_{lam.seperation}}{c})_{mean}$	0.25	-

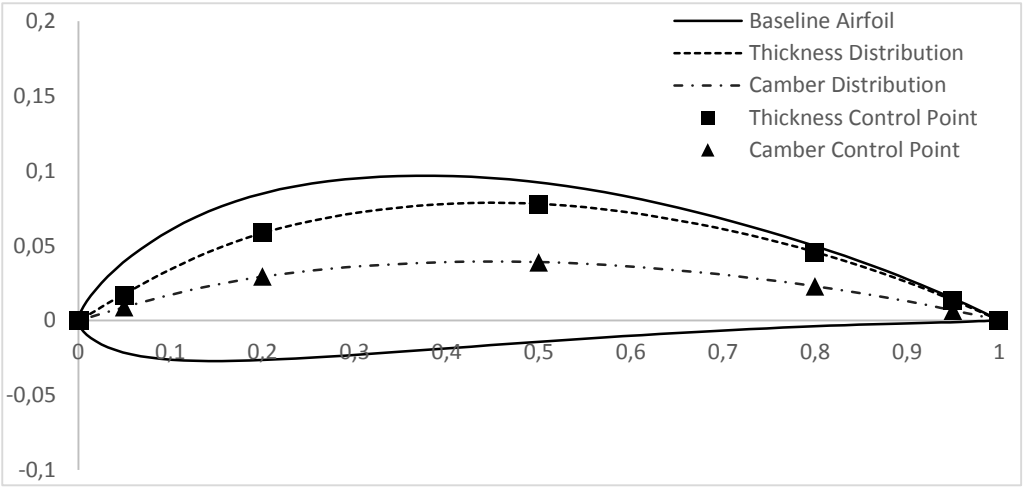

Figure 2-2 Baseline wing airfoil thickness control points and camber control points

Table 2-3 Optimization results for 14 m/s

	Cr [m]	Ct [m]	b/2 [m]	a.o.a [Degree]	Lift [N]	Drag Total [N]
Base	0.060	0.060	0.30	8.4250	5.0000	0.3061
O14	0.097	0.049	0.36	2.8110	5.0000	0.2000

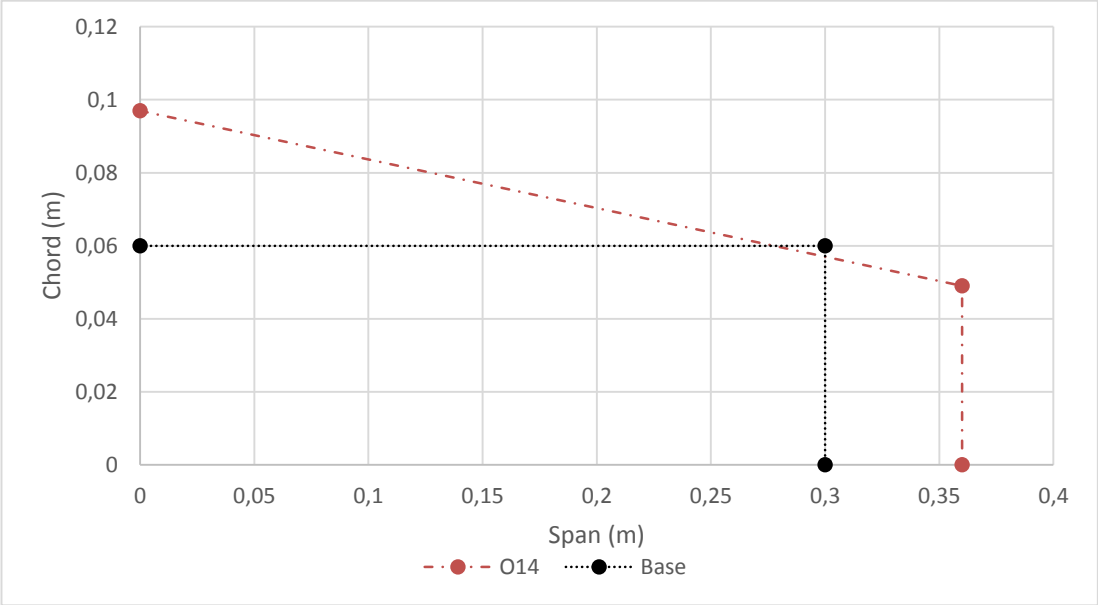

Figure 2-3 Base and O14 planforms

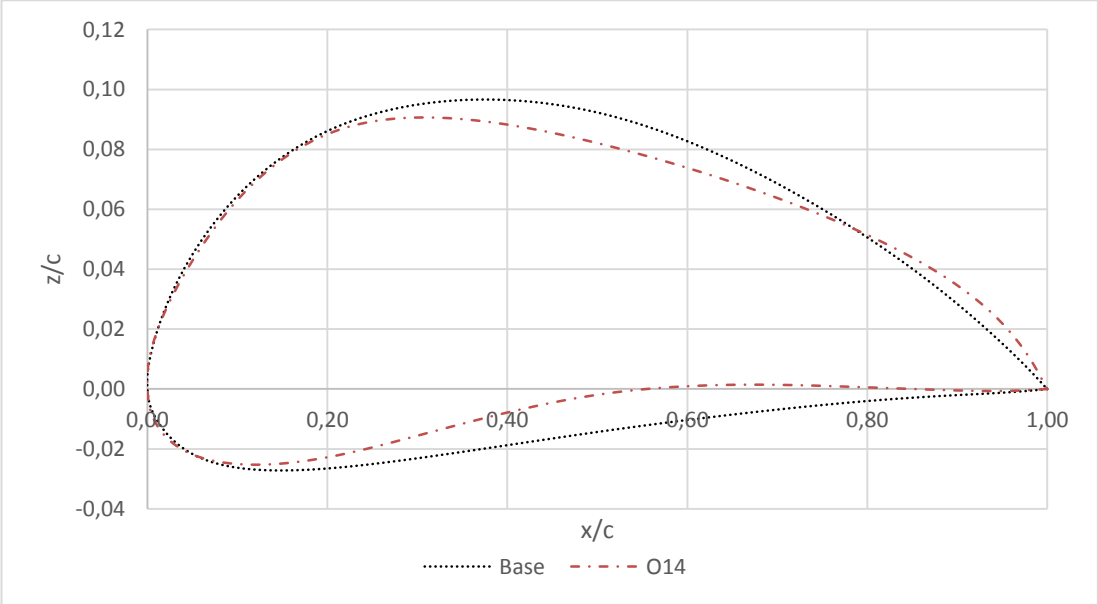

Figure 2-4 Base and O14 airfoils

2.1.1.2. Morphing Wing Planforms at 16.5 m/s

In this optimization process, a parametric study is performed in order to investigate the effect of shape change allowance on the aerodynamic results. Airfoil shape change is allowed according to the upper and lower limits of the control points. These shape changes are limited by 10 percentage change of y coordinate of control points of the optimized wing airfoil. A sample morphing optimization problem is expressed in Equations from **(2.1)** to **(2.6)** for 16.5 m/s.

$$\textbf{Minimize } D = D_i + D_p + D_f \quad @\ V_\infty = 16.5\ m/s \tag{2.1}$$

Subject to

$$L = W = 5\ N \tag{2.2}$$

$$-5^o \leq \alpha \leq 15^o \tag{2.3}$$

$$0.90 * \left(\frac{Z}{C}\right)_{optimized\ fixedairfoil,i} \leq \left|\left(\frac{Z}{C}\right)_{up_{\frac{x}{c}=i}}\right| \leq 1.10 * \left(\frac{Z}{C}\right)_{optimized\ fixedairfoil,i} \tag{2.4}$$

where $i = 1,8$ thickness control points

$i = 7,14$ camber control points

$$0.04\ m \leq c_r, c_t \leq 0.1\ m \tag{2.5}$$

$$0.24\ m \leq b/2 \leq 0.36\ m \tag{2.6}$$

Table 2-4 Optimization results of morphing wing at 16.5 m/s

	Cr [m]	Ct [m]	b/2 [m]	Aoa [degree]	Lift [N]	Drag Total [N]
Base	0.06	0.06	0.30	4.560	5.00	0.250
O14	0.097	0.049	0.36	0.447	5.00	0.205
M16.5	0.077	0.049	0.354	1.105	5.00	0.158

The results of the analysis are represented in Table 2-4 and Table 2-4 and Table 2-5.As can be seen, the morphing wing has greater planform are compared to O14 wing but greater planform area compared to Base wing. The span is comparably smaller but the taper ratio is higher compared to the O14 wing.

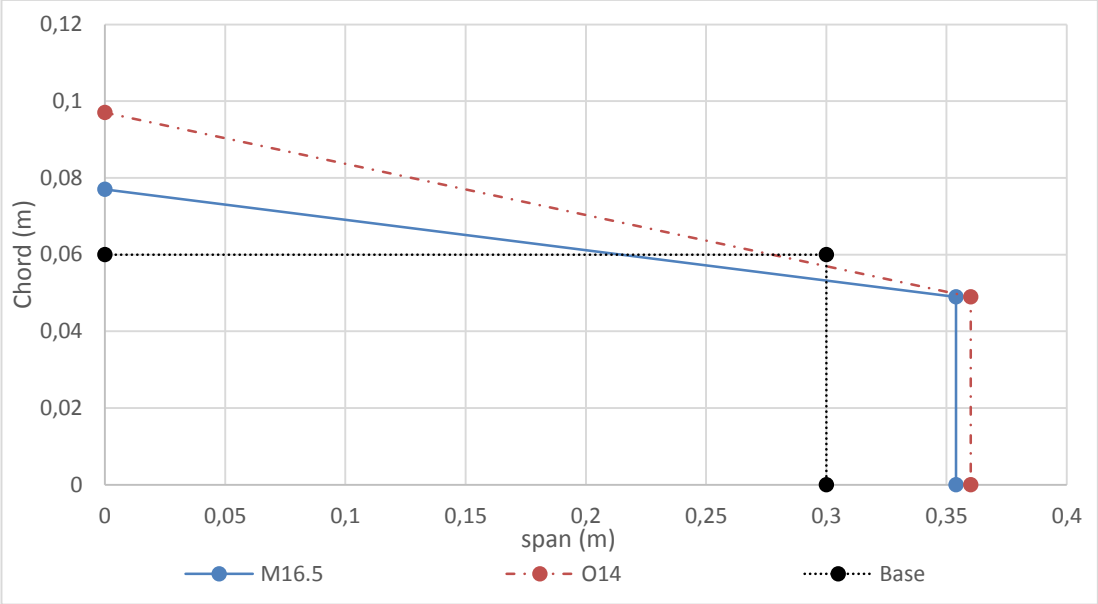

Figure 2-5 Base, O14 and M16.5 planforms

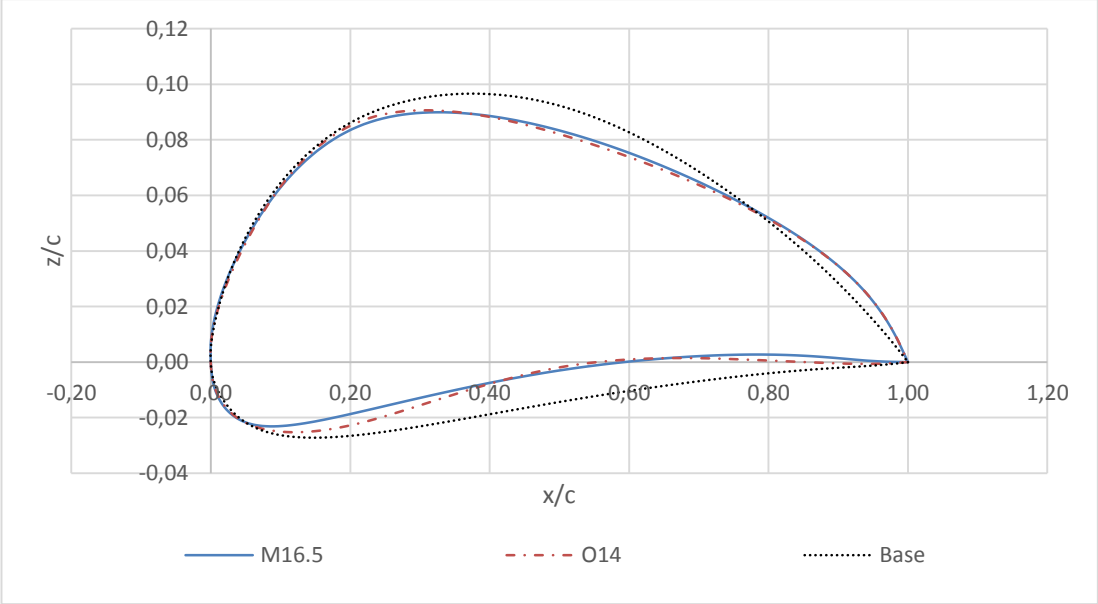

Figure 2-6 Base, O14 and M16.5 airfoils

2.1.1.3. Optimization of the Wing Planform at 10 m/s

Morphing wing optimization process is also conducted at 10 m/s based on the wing that has been optimized at 14 m/s before. Allowances are clearly expressed in Equations from **(2.1)** to **(2.6)**. Besides airfoil and planform optimization outcomes are represented for 10m/s in Figure 2-7 and Figure 2-8, respectively with the above mentioned wings which are baseline, fixed optimized wing and 16.5 m/s morphing wing. Notice that Base and M16.5 wings could not generate the necessary lift at this velocity.

Table 2-5 Optimization Results of Morphing Wing for 10 m/s

	Cr [m]	Ct [m]	b/2 [m]	Aoa [degree]	Lift [N]	Drag Total [N]
Base	0.0600	0.0600	0.30	15.000	3.944	0.4370
O14	0.0970	0.0490	0.36	11.212	5.000	0.457
M16.5	0.077	0.0490	0.354	15.000	3.624	1.094
M10	0.1000	0.0860	0.36	7.8400	5.000	0.3130

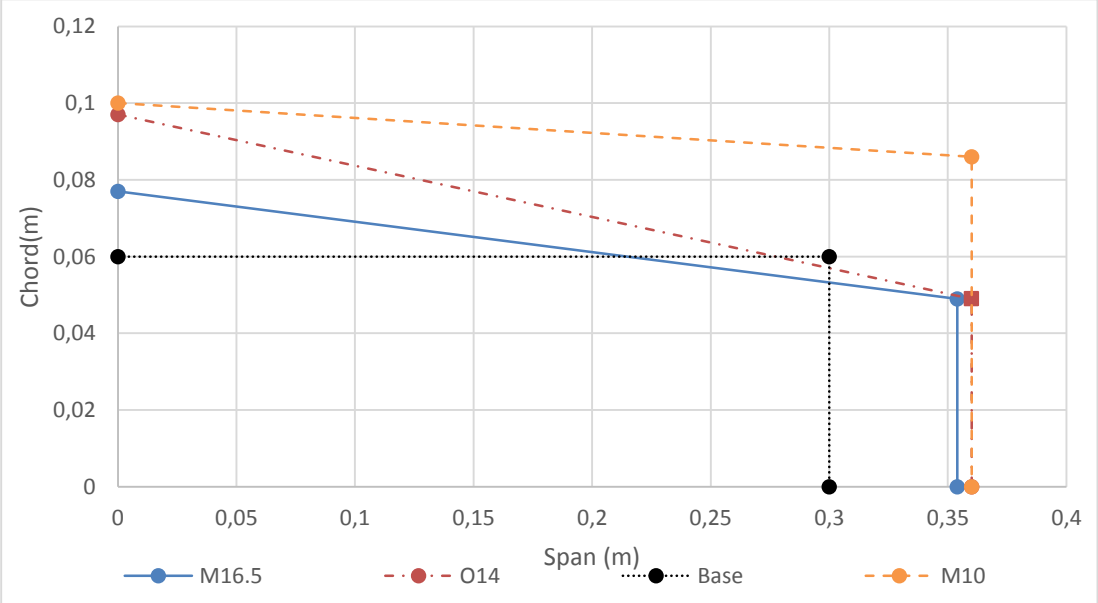

Figure 2-7 Base, O14, M16.5 and M10 Planforms

As expected, the M10 wing configuration has the largest planform area to generate the required lift. The taper is very low and the span is comparable to M16.5 and O14

wings. The airfoil has significantly higher camber in order to produce the desired lift at such a low speed.

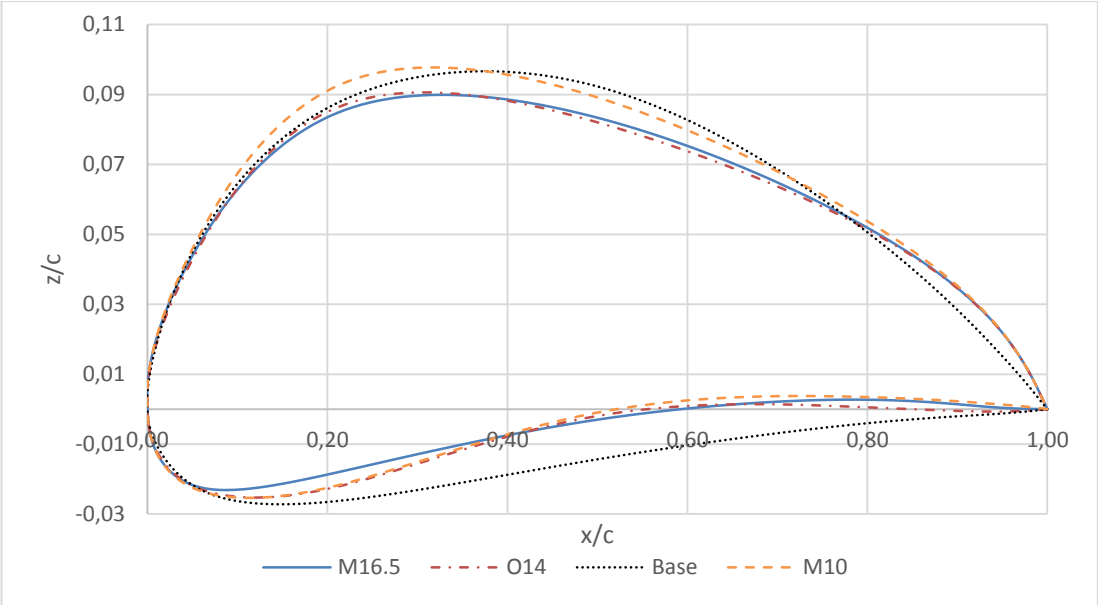

Figure 2-8 Base, O14, M16.5 and M10 Airfoils

2.1.2. CAD Design of the Wings and Test Setup

Wings and Test Setup are designed by taking compatibility to wind tunnel dimensions and experimental conditions into consideration. Therefore, wings are designed with a flange at the root chord in order to be fastened to the angle of attack plate. Then, this angle of attack plate is designed in order to be fastened to the high precision load cell. These designs are generated by CATIAV5 CAD/CAM software as seen in Figure 2-9.

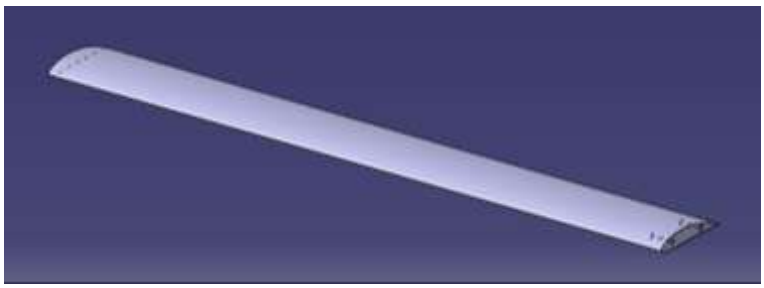

Figure 2-9 CAD Design of the baseline wing

For the measurement of different angles of attack, angle of attack plate is designed. The main concern in the design of the angle of attack plate is fixing rotating plate and wing at a certain angle. In detail, due to one plate rotating over other fixed plate and by the help of holes and a pin, rotating plate can be fixed at a desired angle with respect to angle of attack plate. The angle of attack plate (orange) and rotating plate (transparent white) are illustrated in Figure 2-10. The angle of attack plate is designed by bores drilled for a 1 degree step increase from -15 degree to 15 degree. Besides, the assembly of all of the parts including load cell can also be seen in Figure 2-11.

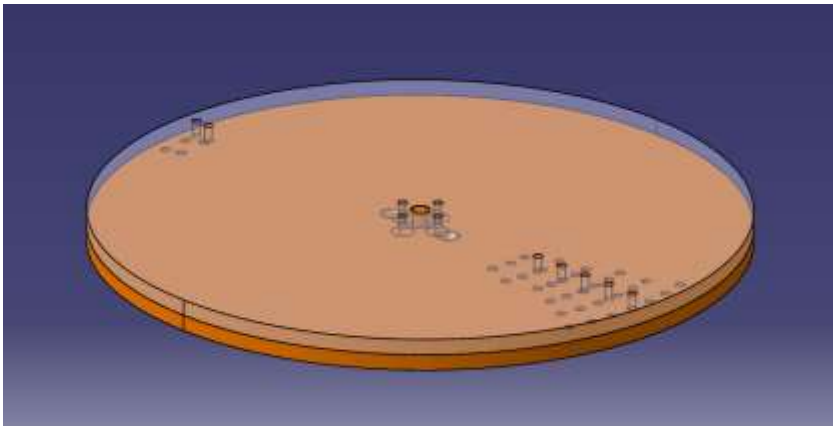

Figure 2-10 Angle of attack plate CAD design

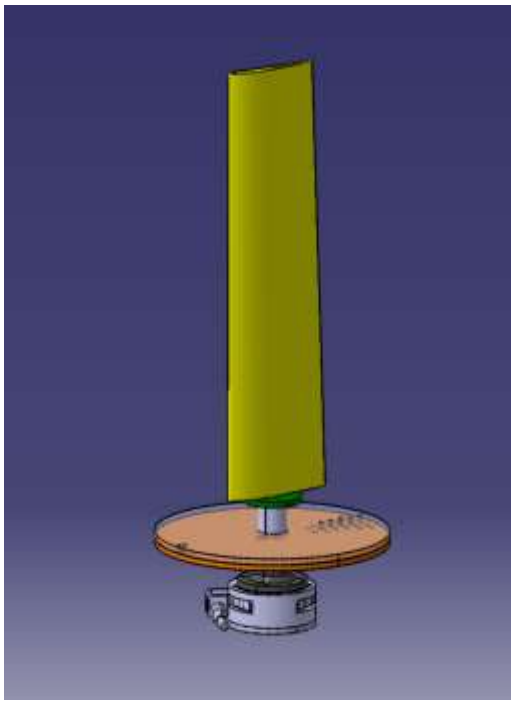

Figure 2-11 Test setup with load cell and wing mounted

2.1.3. Manufacturing of the Wings and Test Setup

Furthermore, after the completion of the design of the wings, manufacturing method is decided as CNC Milling. As precision and surface smoothness are quite important for experimental measurements, the tolerance limitation of the manufacturing method is requested within 0.05 millimeters from the manufacturer. Moreover, Aluminum 6061-T6 material is chosen due to its hardness and machinability. CNC milling process and manufactured parts are shown in Figure 2-12, Figure 2-13 and Figure 2-14. In addition, Figure 2-15 displays the full assembly mounted on the wind tunnel.

Figure 2-12 Manufacturing of the wings with CNC milling method

Figure 2-13 Manufactured M10

Figure 2-14 Manufacturing of angle of attack plate

Figure 2-15 Test setup and wing mounting in wind tunnel

2.2. Wind Tunnel Specifications and Measurement Equipment

2.2.1. Wind Tunnel Design and Specifications

Experiments are conducted in a low speed, continuous flow blower wind tunnel which is placed in Hangar facilities of Aerospace Engineering Department at the Middle East Technical University shown in Figure 2-16. This particular wind tunnel is capable of blowing 3 m/s to 17 m/s wind at the exit plane of its test section.

Figure 2-16 METU Aerospace Engineering Department Low Speed Wind Tunnel

The wind tunnel includes five main sections which are electric motor/blower, diffuser, straight chamber (settling chamber), contraction cone and test sections. Motor/Blower section of the wind tunnel consists of 0.6 meters of diameter double intake radial blower and 18.5 kW AC motor controlled by PLC frequency control module. Also, dimensions of the wind tunnel are illustrated in Figure 2-17.

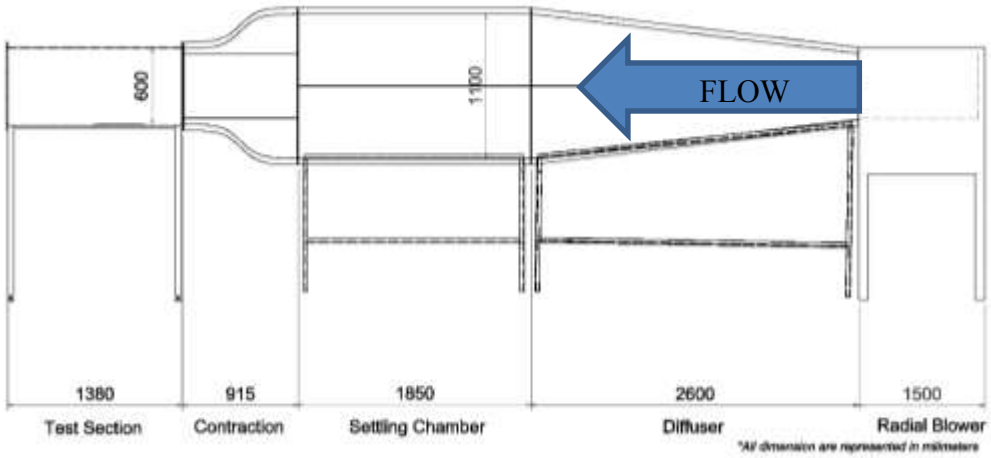

Figure 2-17 Dimensions of the wind tunnel

Figure 2-18 METU Aerospace Eng. Dept. low speed wind tunnel

2.2.2. Wind Tunnel Characterization

Wind tunnel characterization was performed with the same wind tunnel which was reported by Ostovan et. al.[43]. In this report, variations in inlet velocity, turbulence intensity and total pressure were measured at the wind tunnel exit plane geometry. This work was conducted by a Kiel probe and hot-wire probe placed perpendicular to the airstream of flow. Figure 2-19 shows major aerodynamic parameters at the exit plane

of the wind tunnel working at 10 m/s. In addition, these parameters are illustrated in Figure 2-20 along with vertical and horizontal lines placed in the middle of test section's exit plane [43].

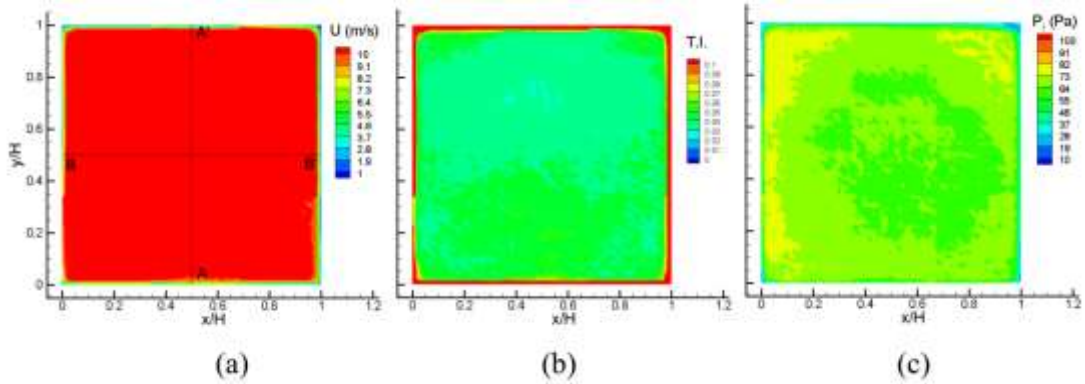

Figure 2-19 Axial velocity of flow (a), turbulence intensity (b) and total pressure (c) variations at the wind tunnel's test section inlet plane [43].

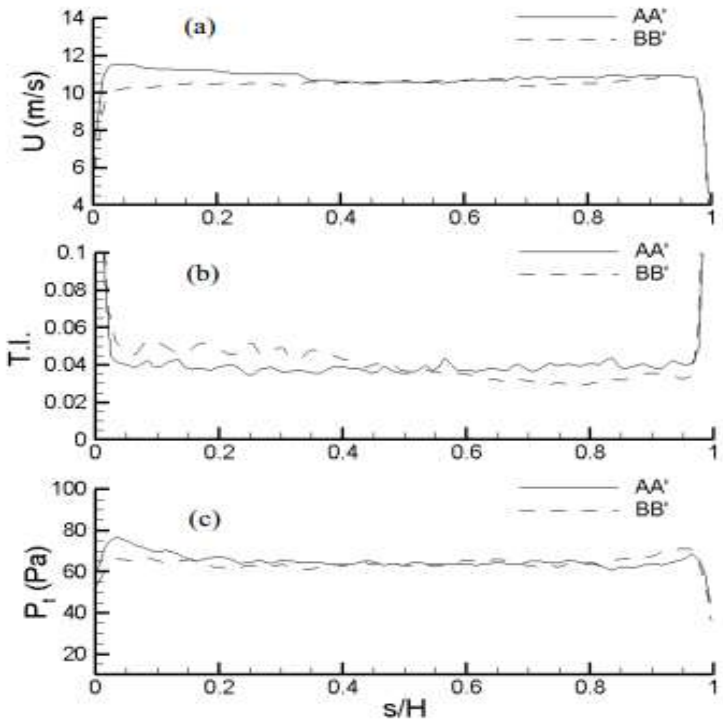

Figure 2-20 Axial velocity of flow (a), turbulence intensity (b) and total pressure (c) variations along the vertical and horizontal lines at the wind tunnel's test section inlet plane [43].

2.2.3. Anemometer

For this study, air flow speed is measured by a thermo-anemometer test instrument all throughout the experiments. Dwyer 471B is utilized in the experiments from Aerospace Engineering Department inventory because of being compact and easy-to-use. Dwyer 471B can measure 0 to 30 m/s wind speeds within an accuracy of 3% in an ambient temperature ranging from 4 to 32 ^{o}C. Also, this equipment can measure -40 to 100^{o}C and temperature measurement sensitivity is between ±0.28 ^{0}C for temperatures between 0 and 50 ^{0}C [37]. Dywer 471B can be seen in Figure 2-21.

Figure 2-21 Thermo-anemometer test instrument

2.2.4. Measurement Equipment & Chain

2.2.4.1. Measurement Chain

Measurement chain basically shows the routine of measurement steps. In this case, aerodynamic forces excite the load cell. Due to this excitation, strain gages produce electrical changes. These changes go through power amplifier box to expand the signals numerically to measurable size of units. Then, data acquisition system gathers this electrical analog data, converts them into digital units and sends them to the computer. The software collects this digital data and transforms into meaningful data with the help of known calibration curves and calculations. Fundamental flow chart of the measurement chain can be seen in Figure 2-22.

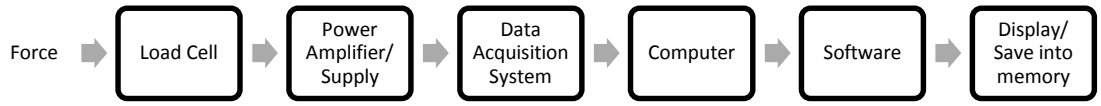

Figure 2-22 Load Cell Measurement Chain

2.2.4.2. Load Cell

6-axis loadcell is attached to the root of the wing in the experiments in order to gather force data. ATI F/T Sensor Gamma is chosen from the inventory of Aerospace Department based on its high resolution measurement rate and 6-axis measurement capability, which is shown in Figure 2-23. This sensor can measure forces up to 32 N in X and Y direction, 100 N in Z-direction which is the direction normal to the load cell's surface. In our cases, lift and drag forces are planned to measure from X and Y axes. Torques/moments can also be measured by this sensor up to 2.5 Nm with respect to X, Y and Z axes of rotations [35]. ATI load cells require a power supply and amplifier shown in Figure 2-24 to distinguish minimal voltage changes of the strain gage in load cells.

Figure 2-23 6-Axis Loadcell mounted on test setup

Figure 2-24 Load Power Amplifier/Supply

2.2.4.2.1 Load Cell Calibration

ATI F/T transducers need no calibration due to its internal systematic. However, load cell package includes the calibrated load cell and its calibration matrix only which is input into the software of the load cell. This information is provided by the vendor of the load cell with a detailed certificate of calibration. Nevertheless, a calibration run

was conducted with known masses in the facilities of the Aerospace Engineering Department. Masses of 5, 50, 100, 500 and 1000g were applied on the load cell and the corresponding data was gathered to verify calibration and biased data. In the light of this test run, load cell is proved to be fully calibrated. In Figure 2-25, calibration monitoring with 500g and 1000g can be seen. Besides, in Table 2-6, all of the measurements are summarized. The decrease of the error percentage can be easily deducted from Table 2-6. The reason of error accumulation is due to the noise originating from the vibration on the ground created by the other test equipment which were active in the test area at the time. As the weight of applied masses onto load cell are increased, noise effect on measurements become negligible due to the domination of weight. Decrease of error percentage can be seen in Table 2-6.

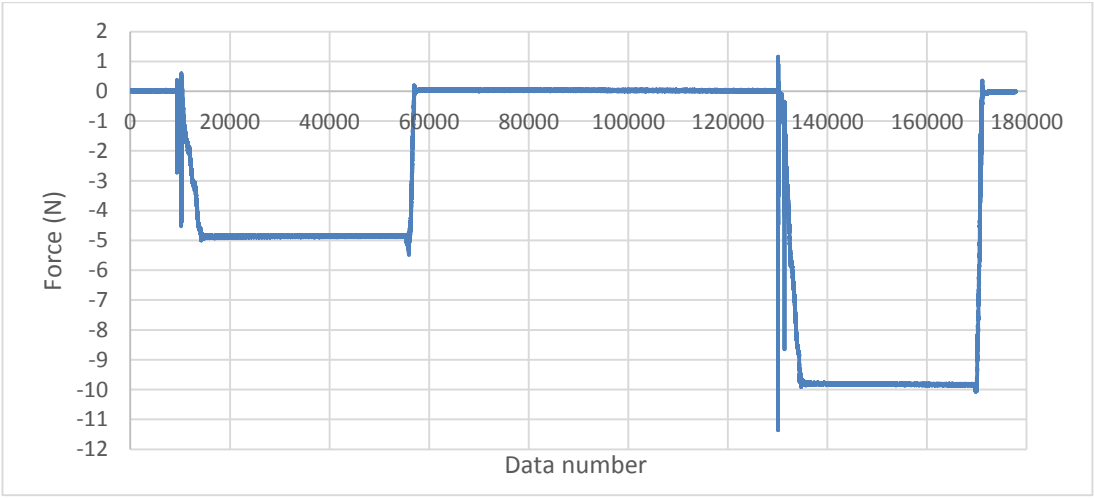

Figure 2-25 Calibration monitoring with known mass 500 gr. and 1000 gr.

Table 2-6 Known mass measurements.

Known Mass (gram)	Measurement (N)	Measurement (gram)	Error (%)
5	-0.05013	5.1209	2.4181
50	-0.47846	48.8722	-2.2556
100	-0.99438	101.5712	1.5712
500	-4.86599	498.0547	-0.38906
1000	-9.81095	1002.14	0.214025

2.2.4.2.2 Eccentric Load Sensitivity (Crosstalk)

Eccentric load sensitivity, also referred to as off-center loading error, is the bias in measurement due to eccentric force loading onto load cell. This phenomenon occurs because of the imperfections in machining, assembly, gage location [38] and bridge type. In order to comprehend this, a simple test was carried out, as shown in Figure 2-26. This test included various known masses and a long cantilevered beam. By the use of these items, the deviations in the measured force were intended to be investigated. Furthermore, the test setup is a good example to simulate lift and drag measurement errors owing to off axis loading for this study.

Figure 2-26 Eccentric load sensitivity test

Table 2-7 Eccentric load sensitivity test measurements

Mass Distance	Fx	My
0	-0.96921	0
24	-0.97378	-0.0230175
50	-0.98408	-0.048605652
100	-0.99115	-0.095998406
200	-1.01792	-0.193075728
300	-1.0421	-0.287057846

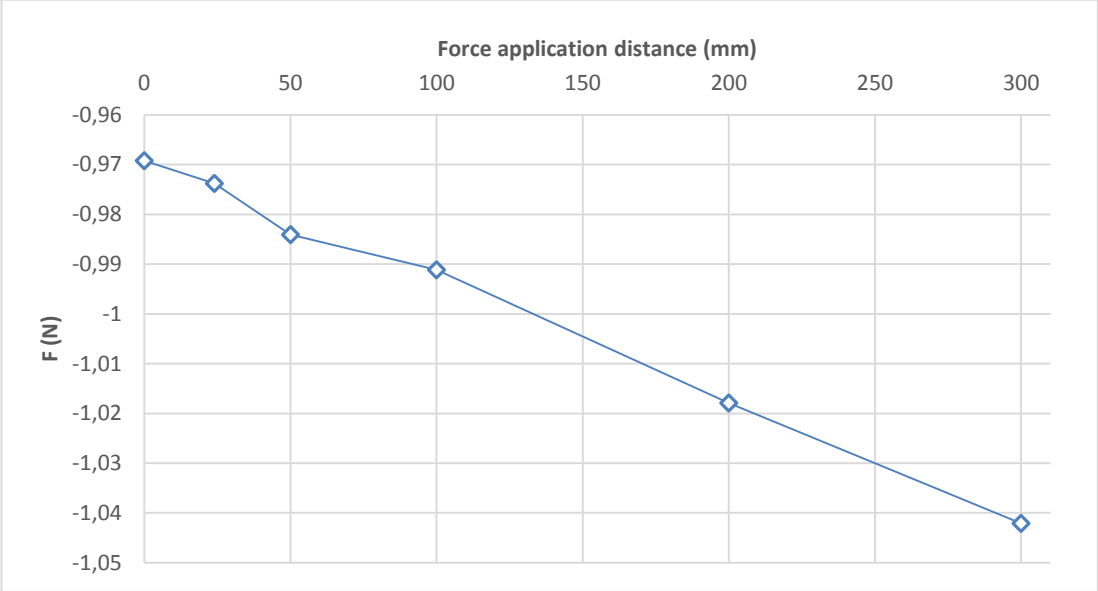

Figure 2-27 Force measurement change with force application distance

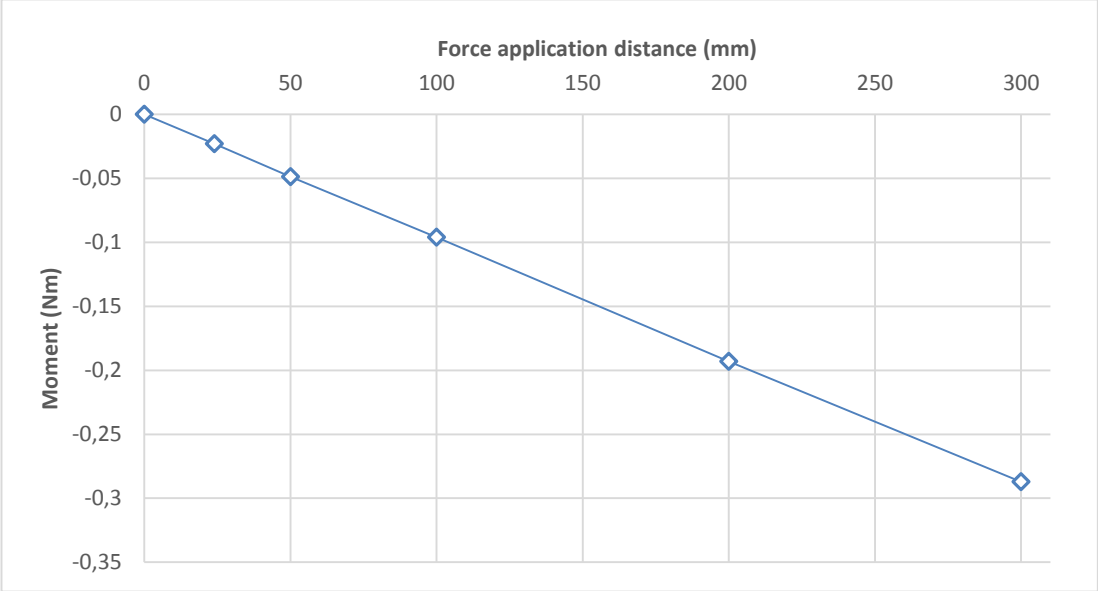

Figure 2-28 Moment measurement change with force application distance

The parameters required to eliminate eccentric load error were deducted from this test. The trends of data in Figure 2-27 is almost linear. This linearity helps to remove bias with some basic calculations. As expected, the trend of Figure 2-28 is measured to be completely linear. The eccentric load bias in force measurement is found to exist while there was no sign of eccentric load bias in moment measurements. The following

equations from **(2.7)** to **(2.11)** explain how to resolve bias error originating from off-axis loading.

F_m: $Measured\ force$

F_r: $Real\ force$

M_m: $Measured\ moment$

x: $Distance\ from\ axis\ center$

e: $Eccentric\ load\ senstivity\ parameter\ (\frac{\%}{mm})$

$$F_m = F_r + F_r * x * e \quad \textbf{(2.7)}$$

$$M_m = F_r * x \quad \text{or} \quad M_m/x = F_r \quad \textbf{(2.8)}$$

$$F_m = M_m/x + M_m * e \quad \textbf{(2.9)}$$

$$x = \frac{M_m}{F_m - M_m * e} \quad \textbf{(2.10)}$$

$$F_r = F_m - M_m * e \quad \textbf{(2.11)}$$

Based on the test data, "e" is calculated as 0.0002575 mm^{-1}.

In the beginning, Table 2-8 and Figure 2-29 the known mass was measured as 0.96921N.

Table 2-8 shows the measurements and the calculations in the test with respect to distance from the axes origin of the load cell.

Table 2-8 Eccentric load sensitivity analytical bias calculation

Distance (mm)	Measured Force	Measured Moment	Calculated Real Force (N) Eqn. (2.11)
0	-0.96921	0	-0.96822
24	-0.97378	-0.02302	-0.96785
50	-0.98408	-0.04861	-0.97156
100	-0.99115	-0.096	-0.96643
200	-1.01792	-0.19308	-0.96821
300	-1.0421	-0.28706	-0.96818
Mean			-0.96840

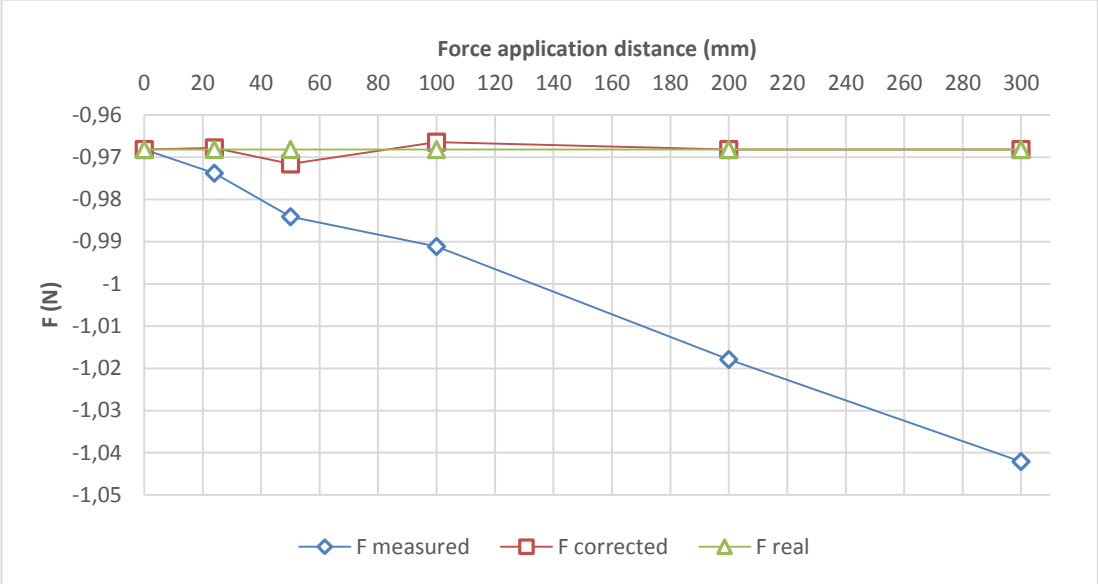

Figure 2-29 Eccentric load sensitivity resolved graph

2.2.4.3. Data Acquisition System

In order to gather measurement data, National Instruments, NI-USB-6211 data acquisition system was used as shown in Figure 2-30. This equipment is able to measure 16 inputs ranging from -10 Volt to +10 Volt simultaneously at sampling rates up to 10,000 Hz. This equipment can also be connected to a computer with universal serial bus protocol [36].

Figure 2-30 Data Acquisition System used in experimental work

2.2.4.4. Computer and Software

For the experiments, a typical desktop PC and National Instrument's Labview software specialized by ATI Sensors were used in order to gather data from the load cell. The calibration matrix, sampling rate have to be selected in the window of this specialized software. Thereby, gathering the data of the experiments could be customized. Also, instantaneous data can be tracked down on the graphs of the software. In addition, data can be stored in the desired directory by the help of "collect data" button on request.

2.3. Uncertainty Estimates

The uncertainties in the experiments were determined from the tolerances and resolution factors of the equipment that were used in the tests. Therefore, in the context of statistical works, the error thresholds in the equipment were investigated and noted for calculation of the error estimates in the measurements. In the experiments with load cells, load cell resolution data gathered from the manufacturer's technical data sheet was used. Force resolutions were 0.00625 N in X and Y direction, 0.0125 N in Z direction. Moreover, torque resolutions are 0.0005 Nm with respect to all three axes [35]. Force and torque values obtained in the experiments were expected to be no more than 10 N in force and 0.075 Nm in torque measurements. Therefore, maximum expected error values could be no more than 0.125% in force measurements and 0.667% in torque measurements.

Table 2-9 6-Axis Load Cell Calibration Properties [35]

	Sensing Range	Resolution
Fx, Fy	32 N	1/160 N
Fz	100 N	1/80 N
Tx, Ty, Tz	2.5 Nm	1/2000 Nm

Wind tunnel is capable of blowing air ranging from 3 m/s to 17 m/s; however, due to the ambient conditions and heating issues, it is possible to maintain flow speed for a

long time duration when the intended speed of airflow is not greater than 14 m/s. Therefore, the duration of data gathering is kept short considering this fact.

Moreover, thermo-anemometer – Dwyer 471B- has the capability of measuring up to 30 m/s within the error threshold of 3%.

Furthermore, bias error and noise conditions were analyzed. During the operations of the ambient equipment, load cell measurement noise and measured bias after the load removal can be seen in Figure 2-31. This scenario was investigated because of the having highest error percentage among the other cases which can be seen in Table 2-9. And the total error that stated in this work, calculated considering case that have the highest error occurrence possibility which is no load case. No load case has the highest error percentage due to noise dominance in the absence of load.

Bias error should be eliminated since the expected drag measurements range from 0.01N to 0.2 N. In detail, magnitude of the noise was almost measured to be of the same with the lowest expected force measurement in this study. Hence, a test was conducted to validate the measurements. The test was utilized considering three different issues, first of them is determining the number of data that should be gathered in order to diminish noise effects on measurements. Second purpose of this test was calculating error originating from noise. Finally, this test was conducted in order to investigate drift in the measurement for the removed load condition.

In Table 2-10, random uncertainty levels are shown. Mean values of the measurements are almost zero, so it can be said that number of data which was taken from this experiment is enough to diminish the effects of noise, and drift of the measurements is negligible. The random uncertainty of the mean is calculated as only the 0.5316% of the mean values. These calculations were performed by using formulas **(2.12)**, **(2.13)** and **(2.14)** at 95.44% confidence level which is found as $\pm 2\sigma$ confidence interval in t distribution table [42]. Therefore, measurements can be claimed as completely trustworthy if the number of samplings are sufficient.

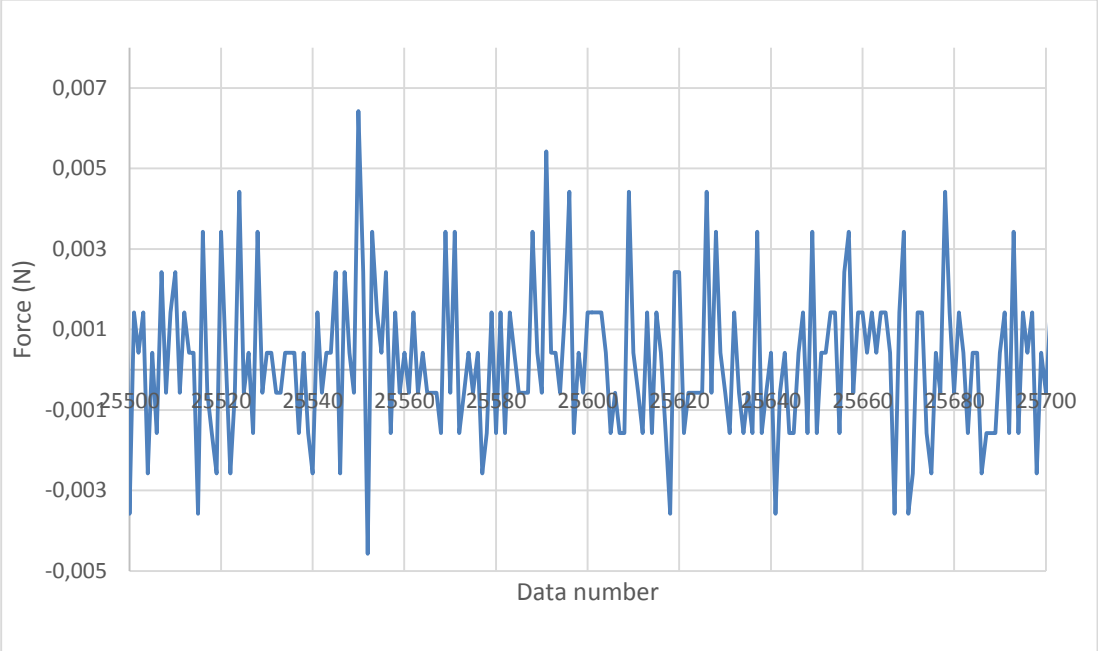

Figure 2-31 A random set of data from measurement of bias and noise

Table 2-10 Uncertainty estimates for load cell (95% level of confidence)

Mean	Std. Deviation	Max	Min	Random Uncertainty	RU of the Mean
0.0045735	0.00192236	0.0074265	-0.0075735	0.0038447	2.4316E-05

Uncertainty of the multiple-measurement is calculated by following formulas.

The expression used for calculating the average of the measurements is [42]:

$$\bar{R} = \frac{1}{M}\sum_{j=1}^{M}(R_j) \quad \textbf{(2.12)}$$

where, R is the measured value

M is the number of data recorded/taken

The expression used for calculating the standard deviation of the measurements is [42], **(2.13)**

$$S_{\bar{R}} = \left[\frac{\sum_{j=1}^{M} \left(R_j - \bar{R}\right)^2}{M-1} \right]^{1/2}$$

The expression used for calculating the random uncertainty of the measurements is [42],

$$P_{\bar{R}} = t * S_{\bar{R}} = \mathrm{t} * \frac{S_R}{\sqrt{M}} \quad \textbf{(2.14)}$$

where t is obtained from t-distribution table,
and the degrees of freedom, $\upsilon = M - 1$

The expression used for calculating the systematic uncertainty formula of the measurements is [42],

$$B_R = \left\{ \sum_{i=1}^{n} \left(B_i \frac{\partial R}{\partial x_i} \right)^2 \right\}^{1/2} \quad \textbf{(2.15)}$$

The expression used for calculating the combine systematic and total uncertainty of the measurements is [42], **(2.16)**

$$W_{\bar{R}} = (B_R^2 + P_R^2)^{1/2}$$

Errors were calculated for each equipment as 0.5316% for load measurement error and 3% anemometer measurement error. Velocity is second order term in the formula and derivative of this term should be taken, for that reason anemometer error is multiplied by 2.

$$W_{\bar{R}} = (6^2 + 0.5316^2)^{1/2} = 6.0235 \quad \textbf{(2.17)}$$

Consequently, load cell originated uncertainties is too low with respect to the anemometer measurements. Therefore, total expected error in force measurements can be calculated as 6.0235% based on thermo-anemometer measurements.

CHAPTER 3

CFD ANALYSIS & RESULTS

3.1. 3D Modelling & Boundary

In this chapter, computational fluid dynamic analyses of the optimized wing are explained. As a CFD software, Ansys Fluent was used. In order to simulate our cases, real boundary conditions were considered and applied to FLUENT models. Wind tunnel's test sections dimensions were applied to the Fluent CFD model. Besides, interior zone was created in order to improve mesh grid to gather more precise data from where the pressure distribution changes the most. Interior zone was designed considering different angle of attacks varying from -5 to 15 degree which is the reason of back cone region seen in Figure 3-1. Based on this design, there is no need to remesh the geometry for each design point.

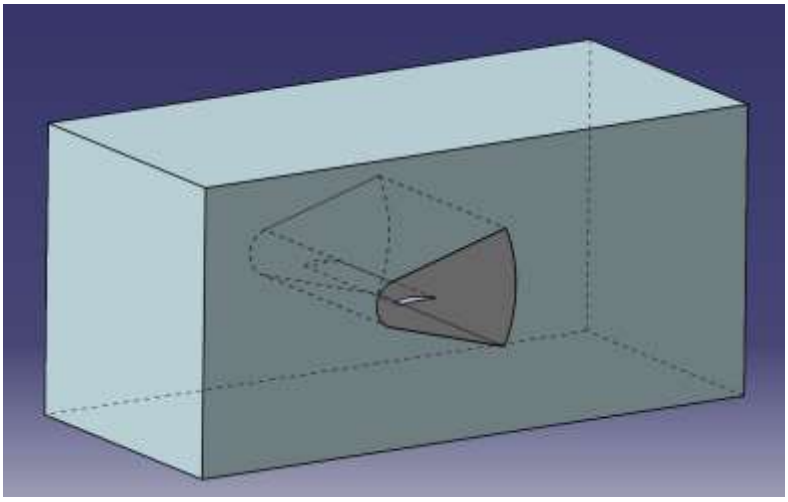

Figure 3-1 CAD Modeling of CFD model

Velocity inlet profiles of this CFD model were assigned parametrically to easily changing velocity and angle of attack for each design point. The list of velocity magnitude, velocity components and angle of attack was inserted into Ansys's design

point list in order to gather solution automatically with one click for each wing configuration.

3.2. Mesh Generation

Mesh geometry was generated by using Ansys meshing tool. Besides, wing surfaces and interior zone were also sized in order to obtain the best solutions. These sizings were performed with the consideration of intensity of pressure differentiation over wing. This mesh geometry is shown in Figure 3-2.

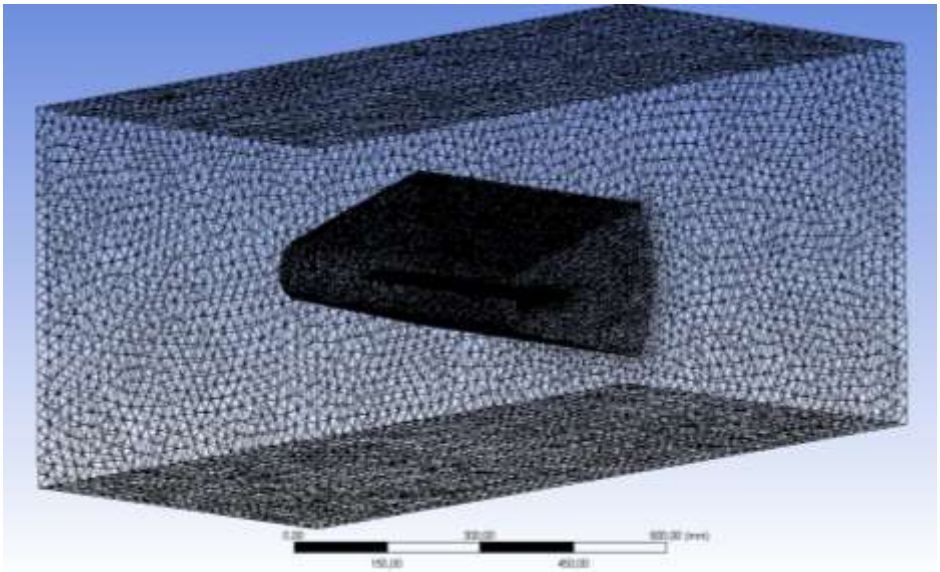

Figure 3-2 Mesh Geometry

In order to gather realistic solution for viscous flows at near wall zones, y^+ calculations were done for each airfoil by using equations **(3.1) - (3.5)**. According to outcome of y plus results, wall thickness is determined. Then, inflation/ boundary layer mesh geometry is generated which is seen in Figure 3-3 .

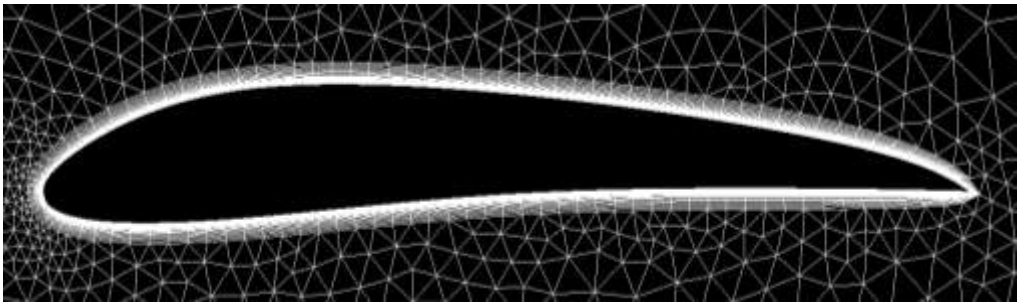

Figure 3-3 Boundary layer mesh geometry

Reynolds Number can be calculated from **[46]**:

$$Re = \frac{\rho \cdot U_{freestream} \cdot L_{boundary\ layer}}{\mu} \quad \textbf{(3.1)}$$

The calculation of the skin friction by Schlichting correlation is **[46]**:

$$C_f = [2\log_{10}(Re_x) - 0.65]^{-2.3} \text{ for } Re_x < 10^9 \quad \textbf{(3.2)}$$

Wall shear stress can be calculated from:

$$\tau_\omega = C_f \cdot \frac{1}{2} U_{freestream}^2 \quad \textbf{(3.3)}$$

The friction velocity is given by:

$$u_* = \sqrt{\frac{\tau_\omega}{\rho}} \quad \textbf{(3.4)}$$

Finally, the wall distance can be computed from:

$$y = \frac{y_+ \mu}{\rho u_*} \quad \textbf{(3.5)}$$

3.3. Turbulence & Solver Model

3.3.1. Solver Model

Fluent contains two kinds of solvers, one of them is Pressure-based solver other one is density-based coupled solver (DBCS). Pressure-based solver, also referred to as segregated solver uses pressure and momentum terms as primary variables. Segregated solver is based on continuity equation terms. In this part of the study, segregated solver is chosen as a solver model because of its low memory requirement and compatibility with low Reynolds number fluid flow cases.

In addition, as a discretization method second-order upwind is selected for pressure, momentum and modified turbulent viscosity selection. The reason of assigning this

discretization method is getting more precise and accurate solutions. Also, Green-Gauss node based interpolation method is selection in the solution segment page of CFD model for its accurate specialty and congruency with mesh geometry which is used in the study.

Pressure-velocity coupling is the numerical algorithm which solves continuity and momentum equations for pressure while pressure based solver is conducted. There are different methods for pressure-velocity coupling. For this study, semi-implicit method for pressure-linked equations (SIMPLE) is assigned for its robustness and adaptability in the study [39].

3.3.2. Turbulence Model Selection

Numerous turbulence models are offered by the commercial CFD software. It is really a work subject independently. For this study, turbulence models are investigated by taking into consideration compatibility with low Re flows and accuracy at predicting lift and drag forces. Three different turbulence models are utilized for the same case in order to compare the results which are seen in Figure 3-4 and Figure 3-5. These three turbulence models are Spallart-Almaras, k-epsilon and k-omega. Also low memory requirements and CPU load is taken into account due to. Nevertheless, among these three turbulence models, Spallart-Almaras model is chosen because of its superior accuracy among 1-equaion models, low memory requirement, being an effective low-Re model and good drag predictions. Spalart-Allmaras turbulence model is a widely used method for the analysis of aerodynamic cases with boundary constraints. In particular, Spalart-Allmaras turbulence model is favored to simulate the aerodynamics with reverse pressure gradient in the boundary layer [47]. This turbulence method is also good at predicting wing-tip vortices [41]. This is another reason for use in this study because drag for such low Re number flows mostly caused by induced drag. Furthermore, Spallart-Almaras model is a reliable model for a flow over wing cases with coarse and fine mesh configurations. Its reliability and mesh independence is verified with experimental studies [40].

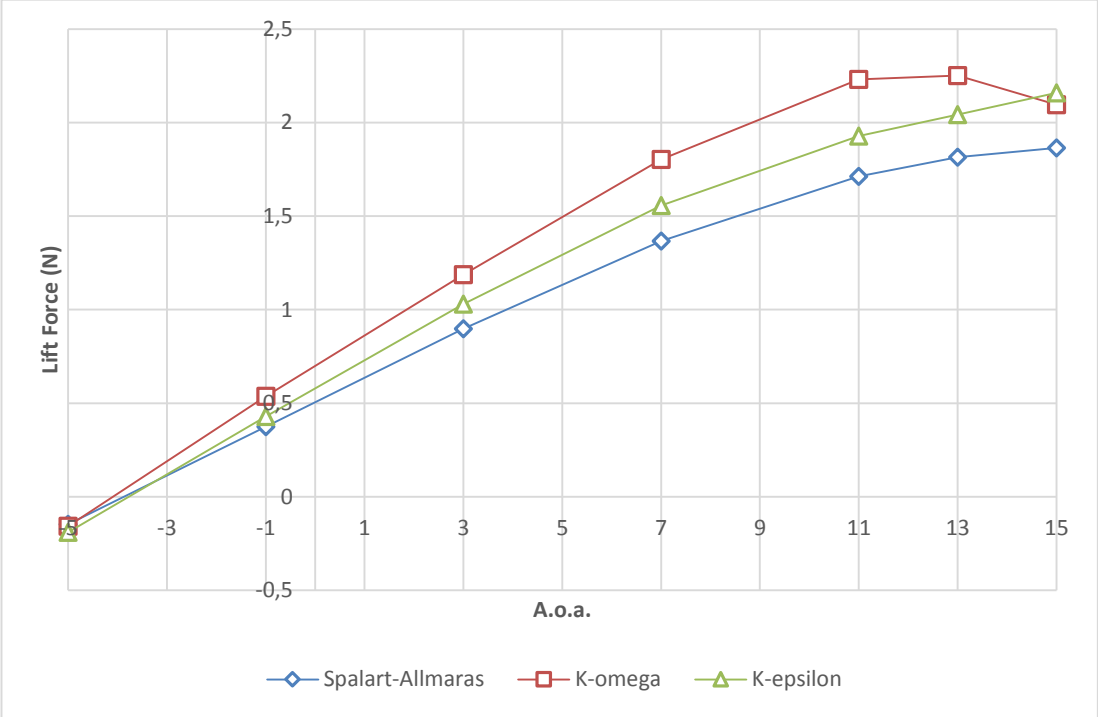

Figure 3-4 Base lift curves for different turbulence models

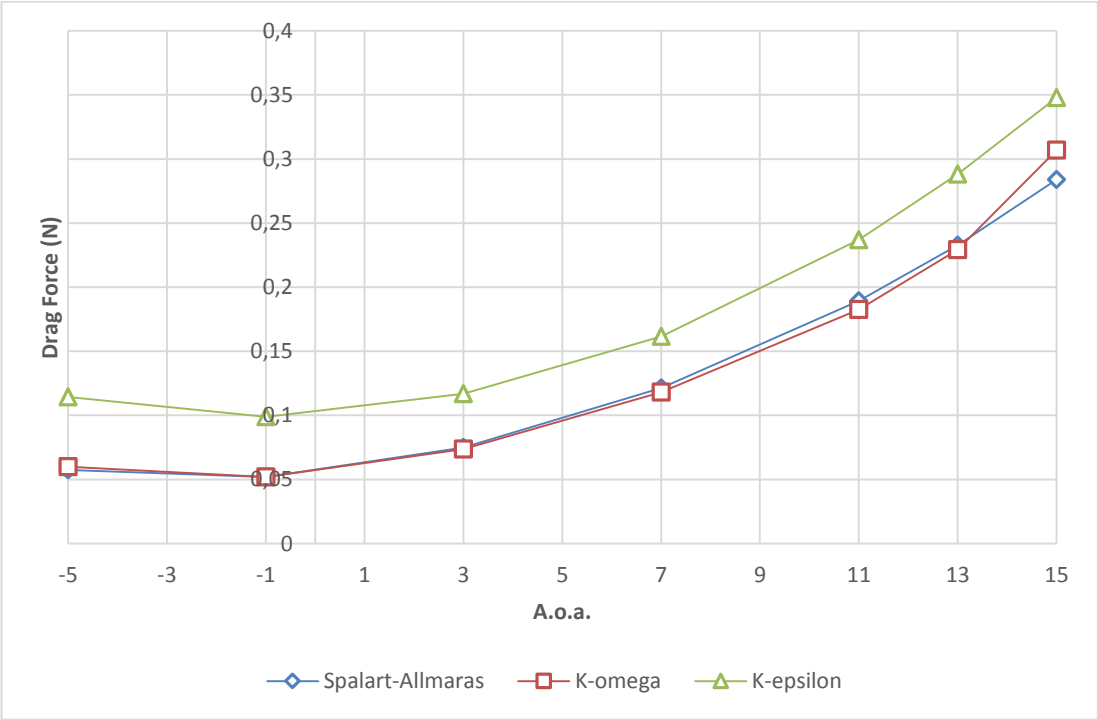

Figure 3-5 Base lift curves for different turbulence models

3.4. CFD Results

CFD simulations are undertaken for each wing configuration mentioned in this study. However, all of the angle of attack calculations could not be performed due to inadequacy of CPU workload and time limitations. Thus, -5,-1, 3, 7, 11, 13 and 15 degrees angle of attacks are investigated for each wing and velocity. Outcomes of CFD analysis are summarized in Figure 3-6 to Figure 3-13.

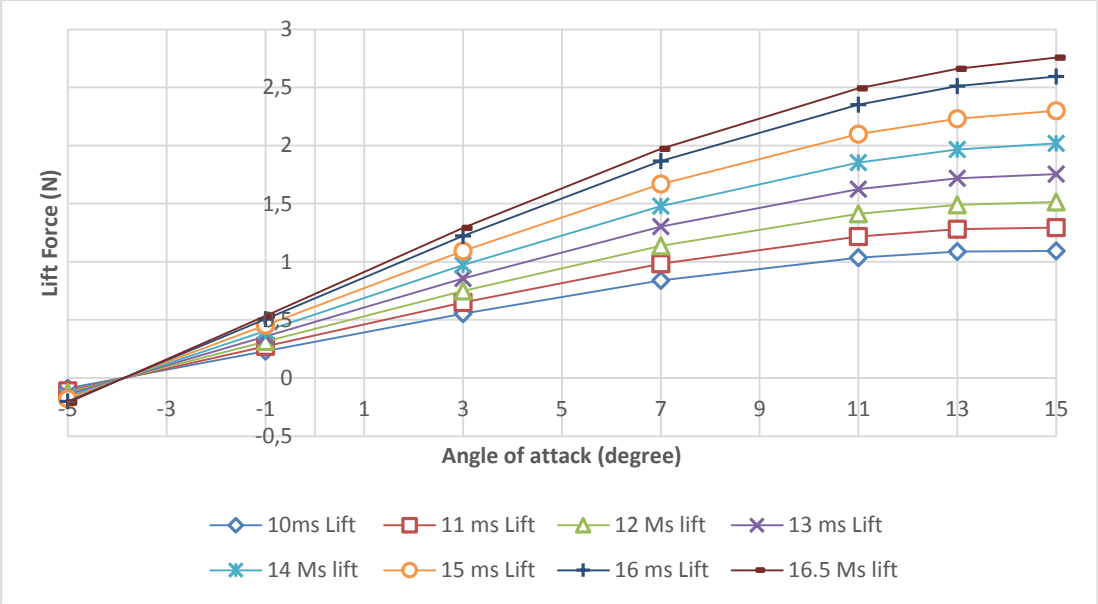

Figure 3-6 CFD analysis of Base lift force vs. a.o.a.

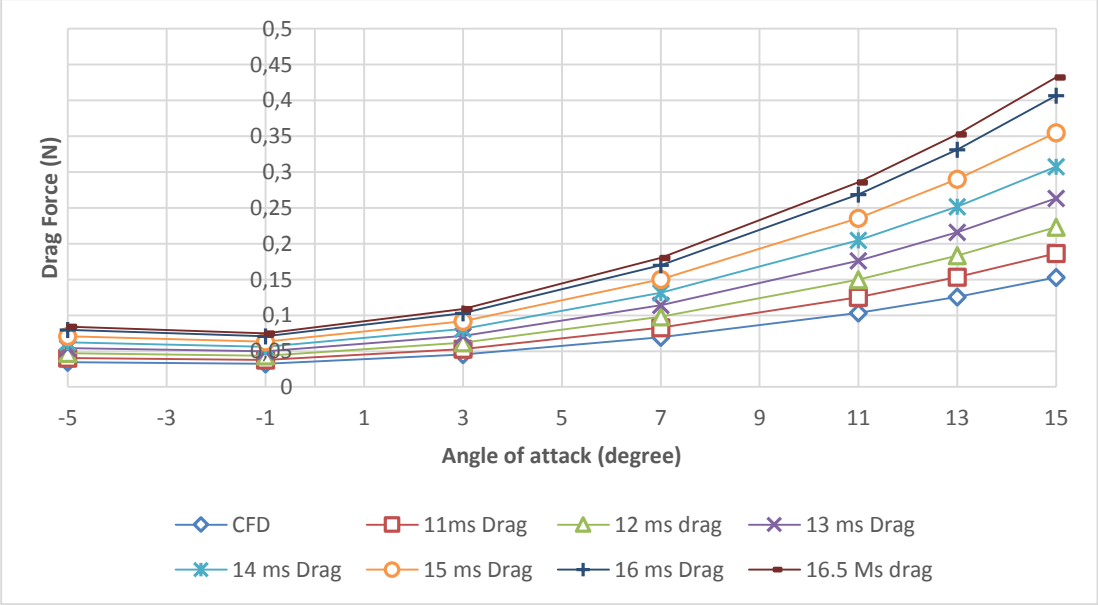

Figure 3-7 CFD analysis of Base wing drag force vs. a.o.a.

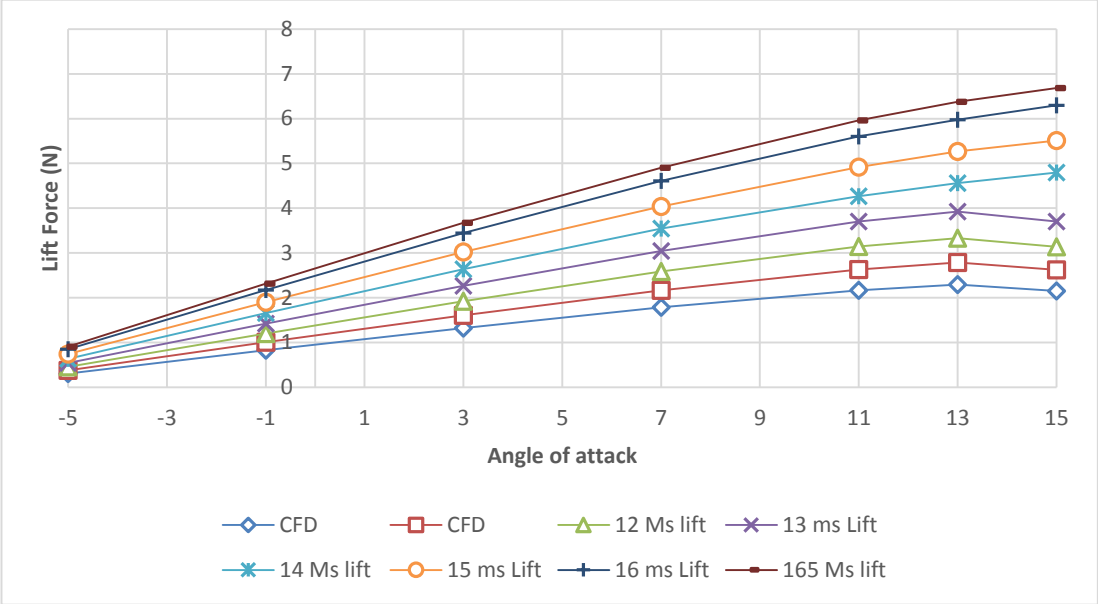

Figure 3-8 CFD analysis of O14 lift force vs a.o.a

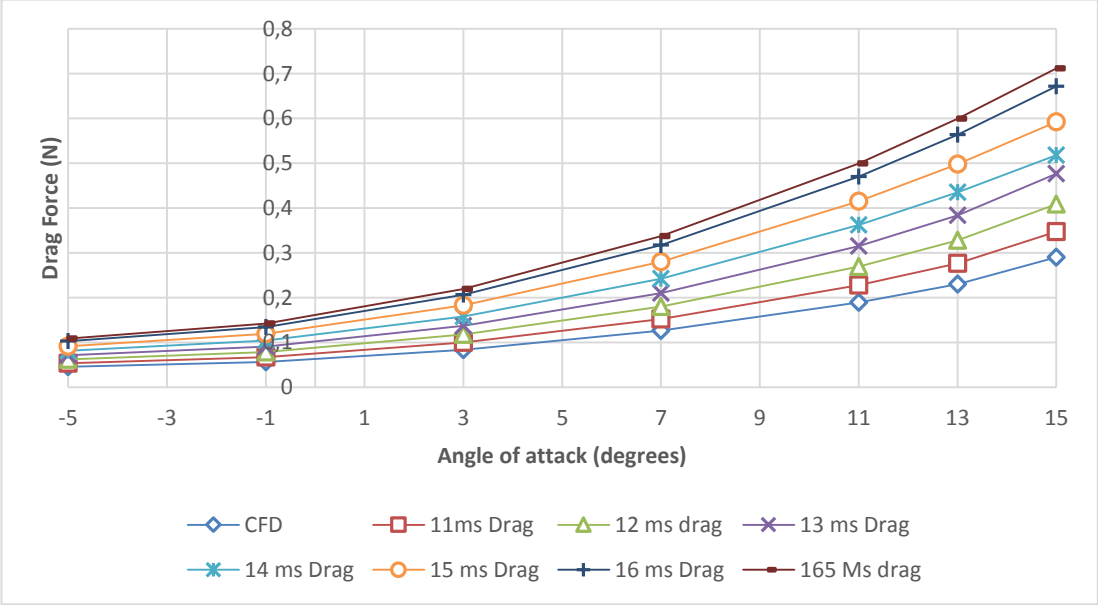

Figure 3-9 CFD analysis of O14 drag force vs. a.o.a

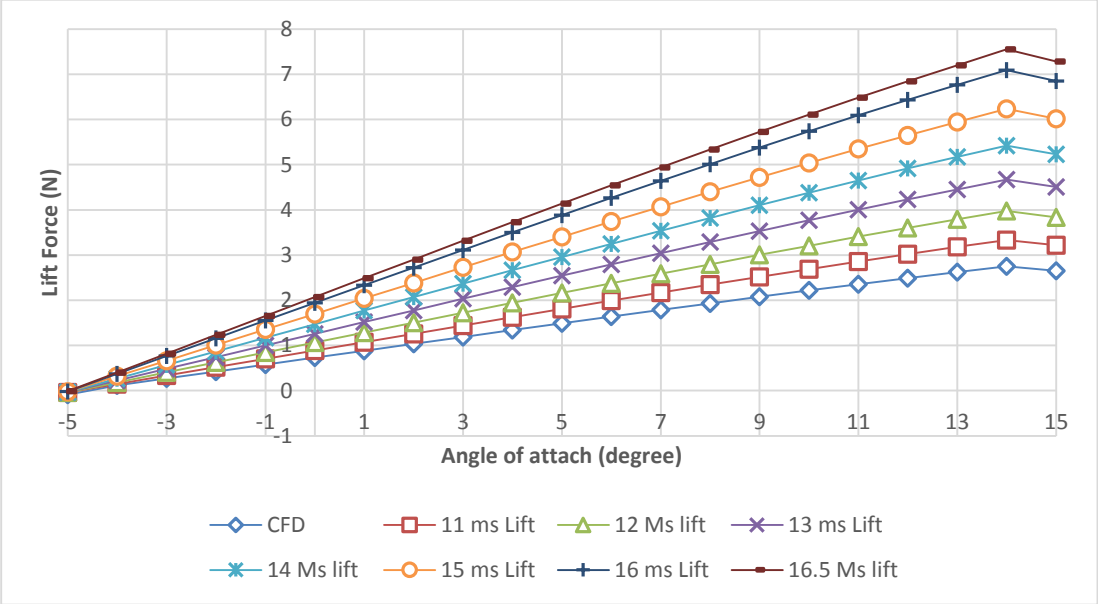

Figure 3-10 CFD analysis of M10 lift force vs. a.o.a.

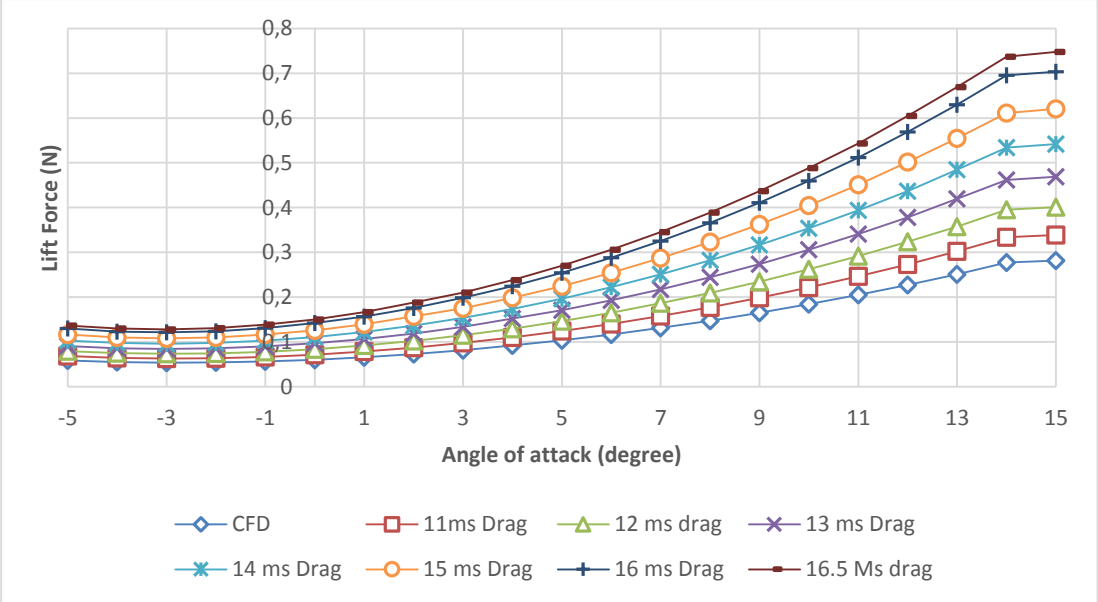

Figure 3-11 CFD analysis of M10 drag force vs. a.o.a.

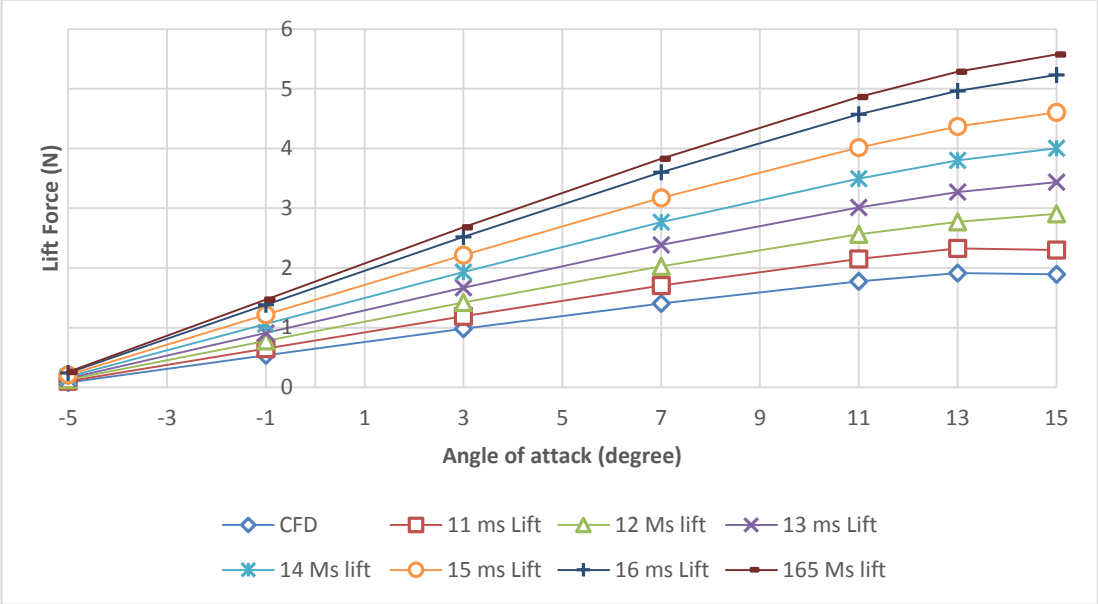

Figure 3-12 CFD analysis of M16.5 lift force vs. a.o.a.

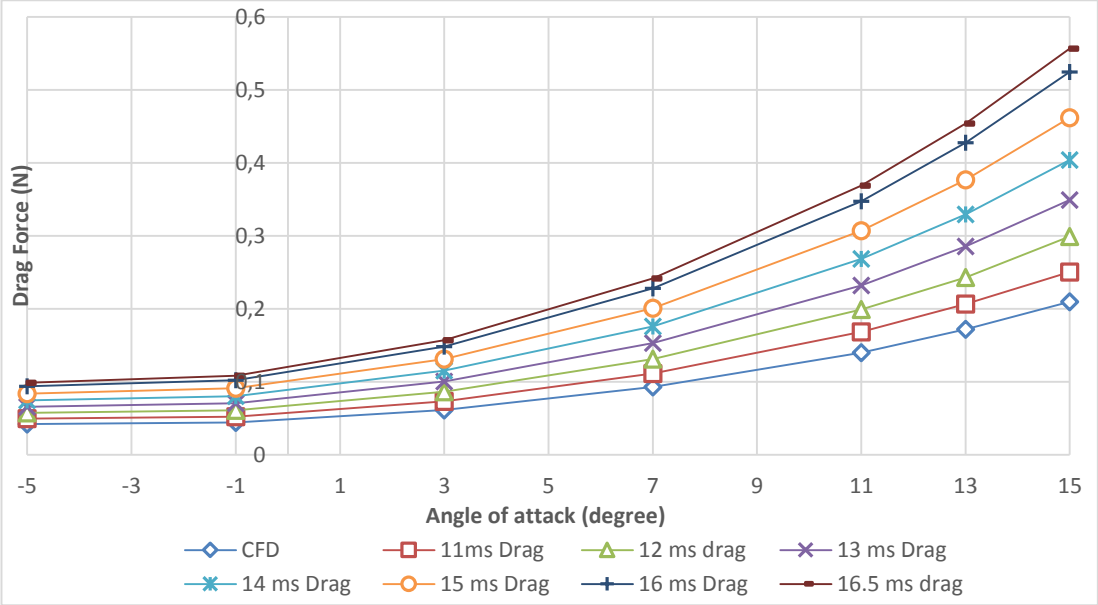

Figure 3-13 CFD analysis of M16.5 lift force vs. a.o.a.

CHAPTER 4

RESULTS & DISCUSSION

4.1. Theoretical Results

4.1.1. Boundary & Conditions

For this study, optimization analysis is performed for 3 different boundary conditions. First of all, full wing optimization analyses are done and all of the outcomes of the tool are divided into 2 in order to render the data comparable with wind tunnel measurements named “Split Half Condition” seen in Figure 4-1. Second approach to this case is half wing analyzed by optimization tool, and this condition named as “No Tunnel Condition” seen in Figure 4-2. Last case of the analysis is full wind tunnel resemblance. This resemblance is provided by assigning all of the boundary conditions as wall boundary condition, except inlet and outlet sections. Besides, dimensions of the boundary conditions are adjusted exactly to the real dimensions of wind tunnel which is used in this experimental study. Final approach of the theoretical analyses is called “Tunnel Condition” These approaches are utilized in order to distinguish the differences of aerodynamic behavior at different boundary conditions and geometry. Boundary conditions and locations can be envisaged in Figure 4-3.

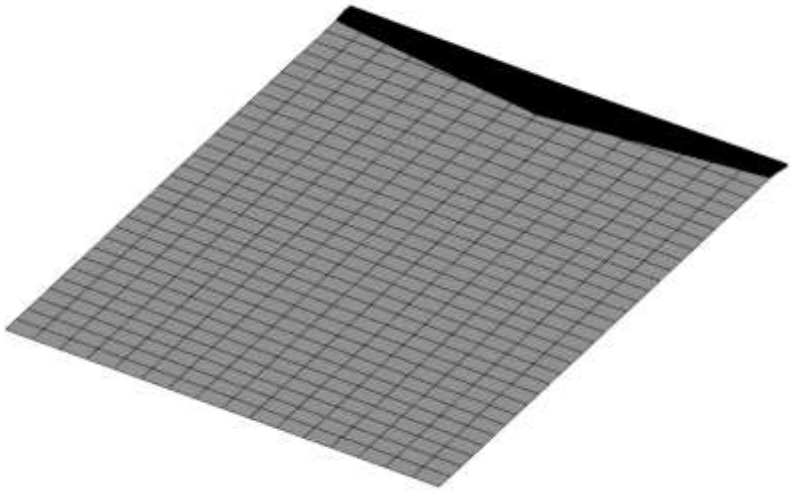

Figure 4-1 Split half condition mesh visualization

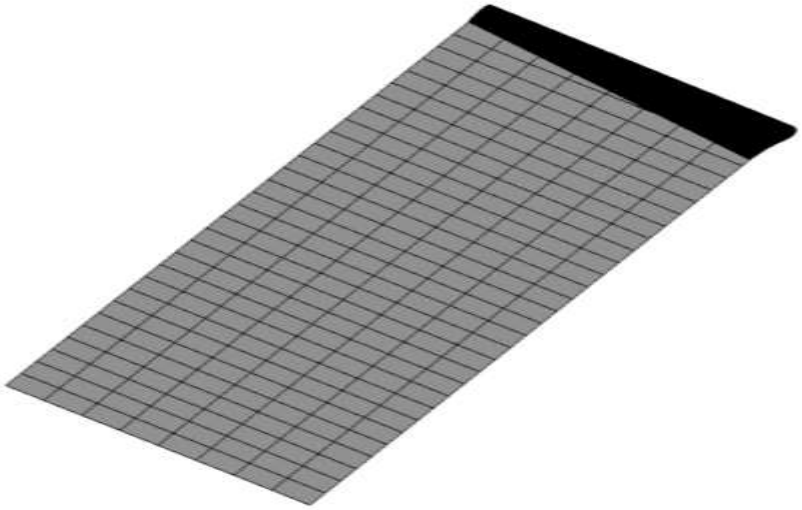

Figure 4-2 No tunnel Condition mesh visualization

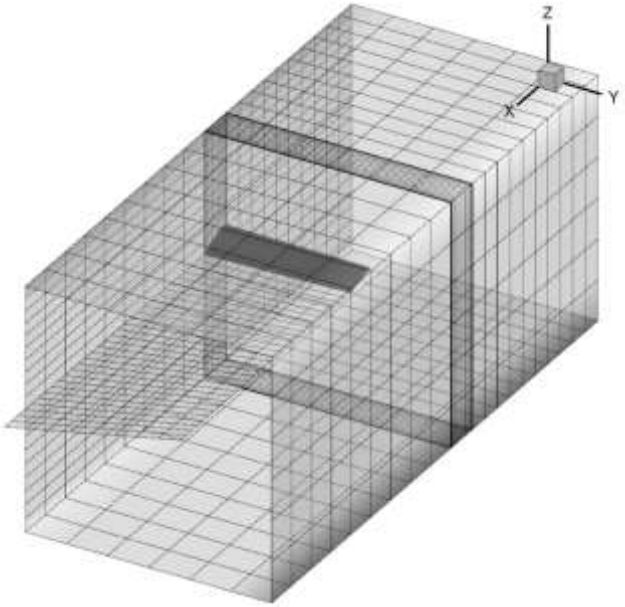

Figure 4-3 Tunnel condition mesh visualization

4.1.2. Optimization Tool Analyses

Analyzes are performed for each wing configuration which are discussed in the previous chapter for different airstream velocities and angle of attacks. Airstream velocities are chosen as 10, 11, 12, 13, 14, 15, 16 and 16.5 m/s. Angle of attack values are assigned between -5 degrees to 15 degrees by 1 degree increment. Whole analysis comprises 4 different wing shapes, 8 different airstream velocities and 21 different angles of attack. In addition to these works, mesh independency test is conducted with three different mesh configurations. To sum up, 672 different cases and 3 mesh cases are analyzed and investigated in this part of this thesis.

4.1.3. Mesh Independence

In order to comprehend the mesh induced result changes, mesh independence work is conducted. Three different mesh configurations are chosen, coarse, medium and fine meshes which are 35 x 4, 35 x 8 and 35 x 37 mesh configurations, respectively. These numbers are the mesh configurations of the plane that are placed on the root chord of the wing, in other words root wall includes 140, 270 and 1295 mesh elements, respectively. This work is utilized with “Tunnel Condition” in order to yield closer

results to measurements of wind tunnel experiment. Lift and drag force results are shown in Figure 4-4 and Figure 4-5.

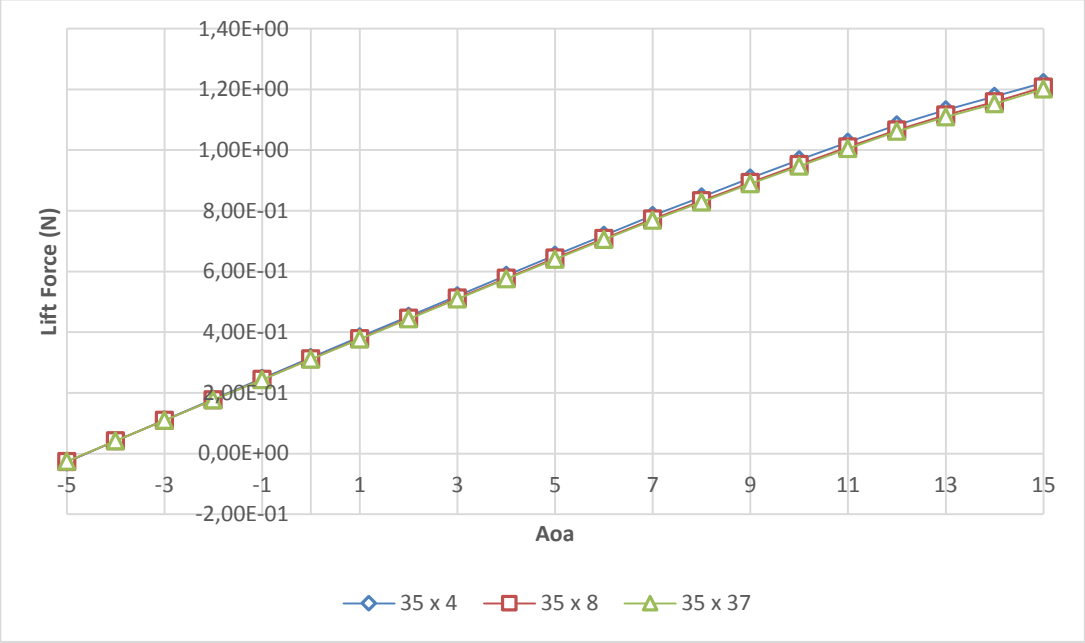

Figure 4-4 Theoretical Lift Forces for different mesh quality

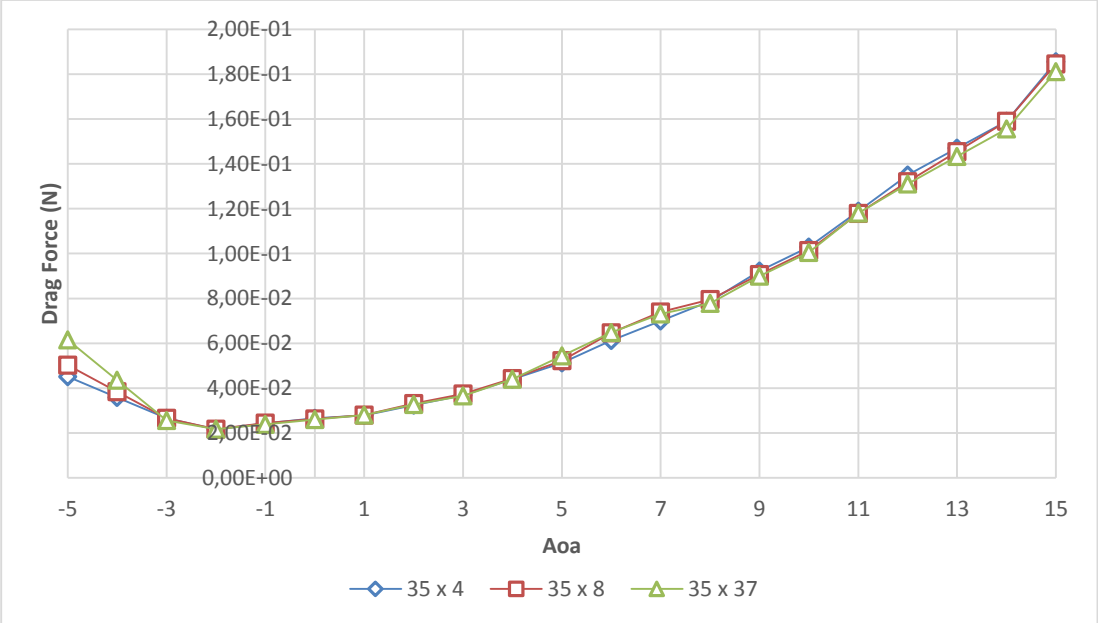

Figure 4-5 Theoretical Drag Forces for different mesh quality

In the consideration of this work, fine (35 x 37) mesh configuration is found more trustworthy and applicable when the results are compared with CFD results.

4.2. Wind Tunnel Experiments

Wind tunnel experiments are conducted at the facilities of METU Aerospace Department's Hangar. Hangar is a temperature controlled indoor zone, thanks to this condition, ambient temperature does not change dramatically during the experiments. Also, invariability of air properties alleviate to reduce repeatability errors. The air properties given in Table 4-1 are used for all theoretical analyzes. Besides, Reynolds number range for each wing configuration is provided in
Table 4-2 in order to enhance comprehension of the aerodynamic condition of each wing configuration exposed.

Table 4-1 Ambient Air Properties

	Min	Max
Ambient Temperature (^{0}C)	18.6	21.9
Flow Temperature (^{0}C)	17.3	20.2
Ambient Pressure (hPa)	1007	1012
Relative Humidity (%)	44	56
Density of air (kg/m^3)	1.17032	1.18888

Table 4-2 Reynolds number range for each wing configuration

	Base	O14	M16.5	M10
10 m/s	42232.80	48511.57	42241.41	61836.52
14 m/s	59125.92	67916.20	59137.97	86571.13
16.5 m/s	69684.12	80044.10	69698.32	102030.26
Min.	42232.80		**Max.**	102030.26

4.2.1. Data Acquisition Determination

Before the wind tunnel experiments, data acquisition determination test was conducted in order to optimize the frequency and the duration of data measurements. This test includes 7 different durations and 6 different frequencies. These measurements are inspected so as to determine the best combination of measurements for the shortest

duration. Relative errors (multiplied by 1000) are expressed in Figure 4-6 and Figure 4-7 as 3D graphs in order to make the selection more comprehensible.

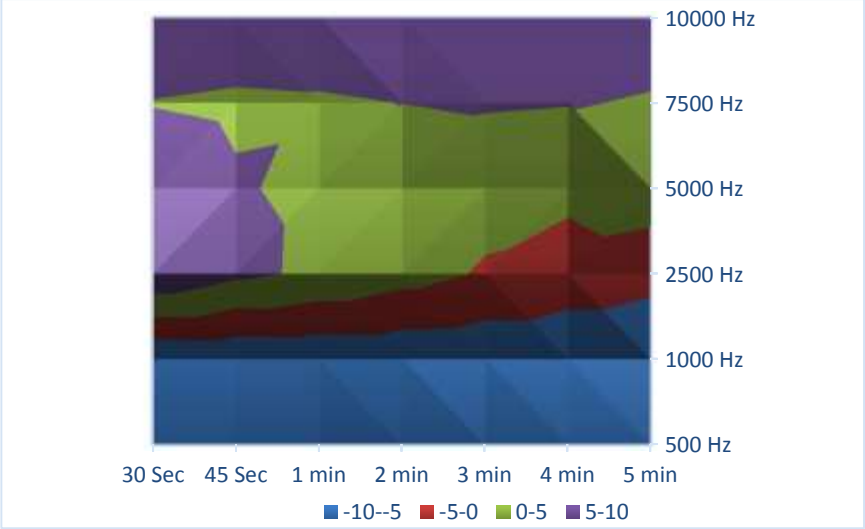

Figure 4-6 Relative error of Lift measurement at different frequency and durations

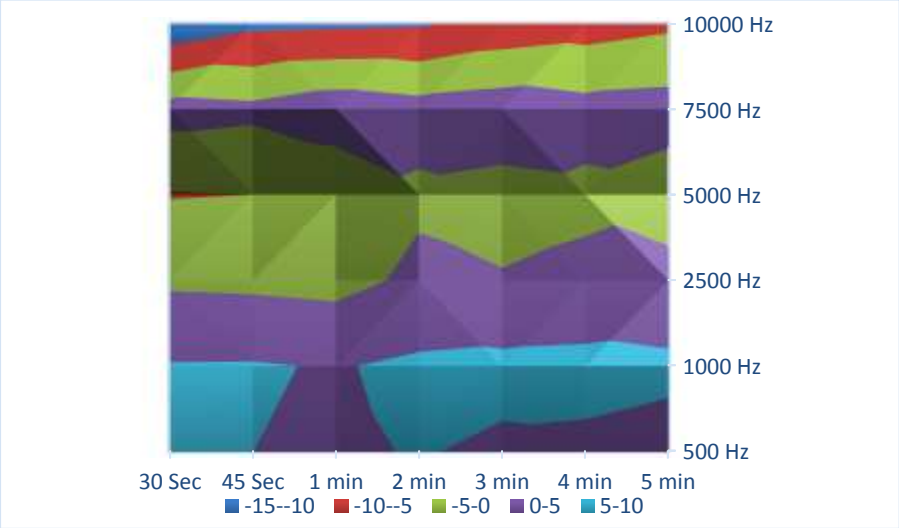

Figure 4-7 Relative error of drag measurement at different frequency and durations

In the consideration of both corresponding graphs, 2500 Hz and 30 seconds data gathering is agreed on, not only for the relative error but also lowering the error originating from steep decrease of wind tunnel airflow speed at high speeds and high run durations.

4.2.1.1. Data Validation

Measurements which were gathered from the experiments, were transformed into meaningful data by averaging all of the measurements for corresponding case. However, a calculation issue was raised owing to round off errors. Two methods can be used for this validation. One of them is conventional averaging and other one is moving average method. Conventional average is simply adding all of the values of measurements and dividing total sum to number of measurements. Moving average method is a little bit more sophisticated method that works by taking average for a limited number of measurements and then all of the partial averages are again averaged. By the help of this method, errors such as truncation and round-off errors can be minimized. For this work, both of the methods are investigated and averaging method was determined for further calculations .This work was conducted on the raw measurement data of the Base configuration for 10 m/s. Maximum difference was calculated as no more than 2%, therefore, conventional averaging method was chosen because of its simplicity and lower run time shown in Figure 4-8.

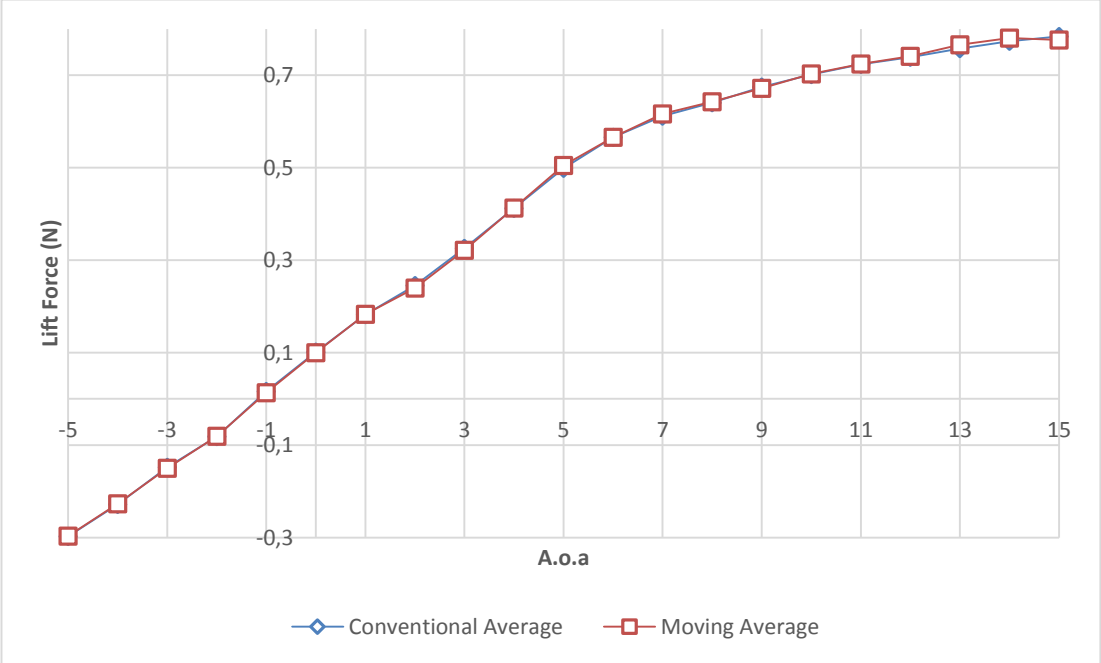

Figure 4-8 Averaging method selection

4.3. Results

In this chapter, all of the results are represented for parameters discussed. Lift and drag force measurements are compared by CFD and theoretical results for each wing configuration.

4.3.1. Base

As experimental work progressed, measurements gathered from the experiments were validated and compared with the results from the optimization tool. It can be observed that experimental results of the lift force are lower than the numerical results and their trend is more likely to stall earlier as can be deducted from Figure 4-10, Figure 4-12, Figure 4-14 and Figure 4-16. Except the Split Half Condition, none of the optimization tool results show stall behavior at high angles of attack. Besides, experimental results show agreement with other results in terms of drag and lift measurements even though there is no overlapping at low speeds. As the airflow speed increases, lift and drag force measurements become similar at angles of attack that are greater than 3 degrees. This incidence could be explained by the increase in momentum of the flow by increasing angle of attack and velocity of the flow. In addition to this, at lower angle of attack interval between -5 and 3 degree, trends of lift and drag curves of baseline wing losses the similarity between Tunnel condition and experimental results. For this range of angles of attack, drag forces are comparably higher than optimization tool and CFD results and lift measurements are lower than expected. It is worthy to note that, there was a strong acoustic noise that occurred in the experiments for the mentioned interval of angle of attacks. Also, manufacturing imperfections and surface roughness may have caused this particular incidence. Furthermore, another interpretation for this incidence is the separation of the flow at low angles of attack that cannot be modeled in theoretical or CFD analyses. Separations at low angles of attack are common for high cambered airfoils as well as airfoils that have noticeable back cusps. Figure 4-9 illustrates this circumstance in an exaggerated manner.

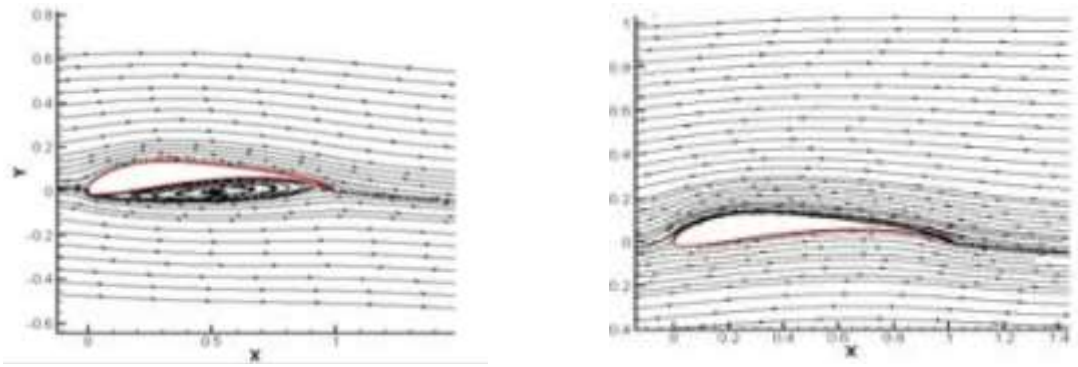

Figure 4-9 Streamline diagram of S1223 Airfoil at -2 a.o.a. (left) and 2 a.o.a (right) [47]

CFD results are in agreement with No tunnel and Tunnel Conditions, except the early stall behavior seen in Figure 4-10. However, drag force curves of CFD, Tunnel Condition and No Tunnel Conditions always overlap. This behavior of numerical results prove that optimization tool is a trustworthy robust tool as a fast and accurate numerical solver.

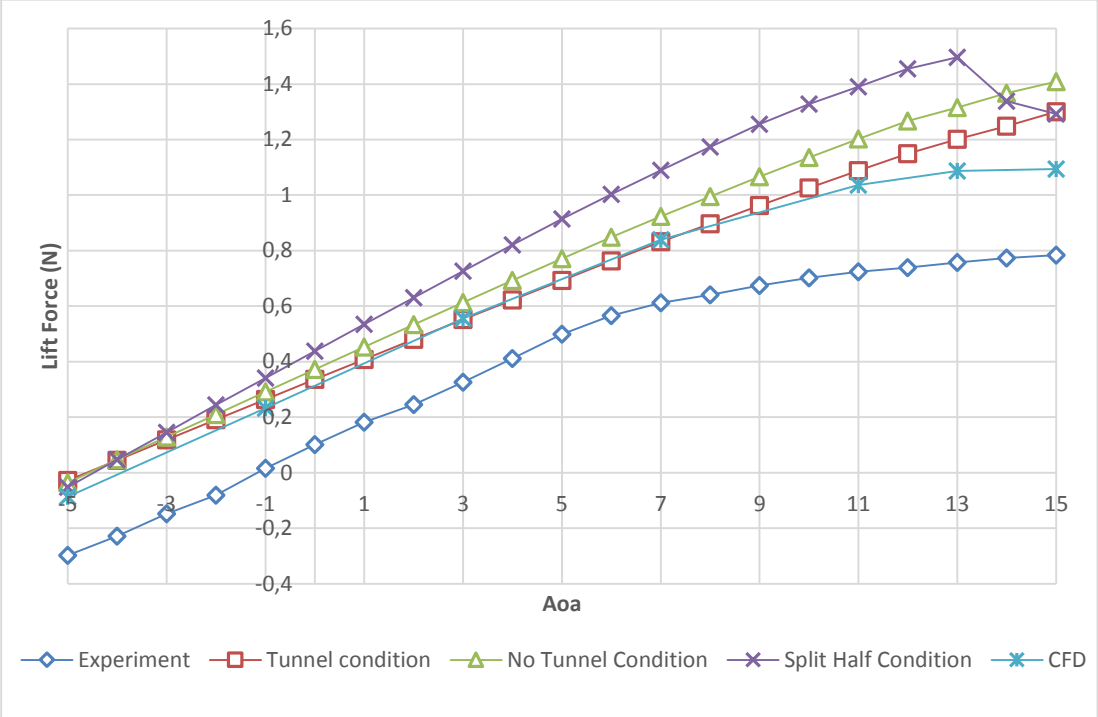

Figure 4-10 Base lift for 10 m/s

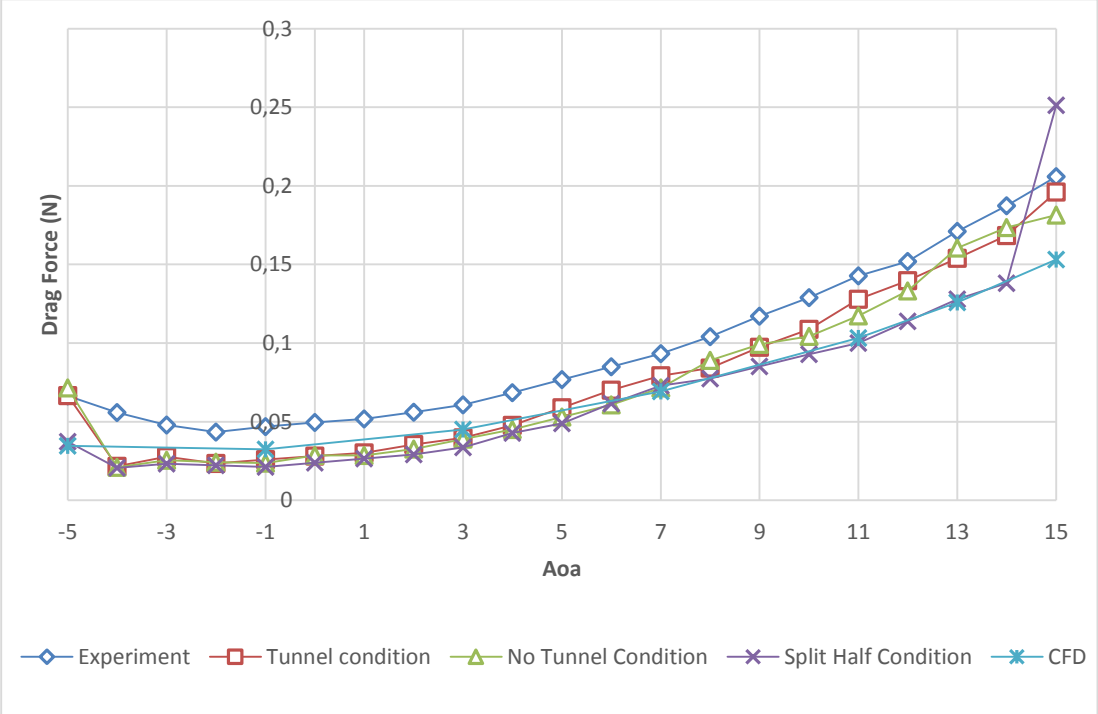

Figure 4-11 Base drag for 10 m/s

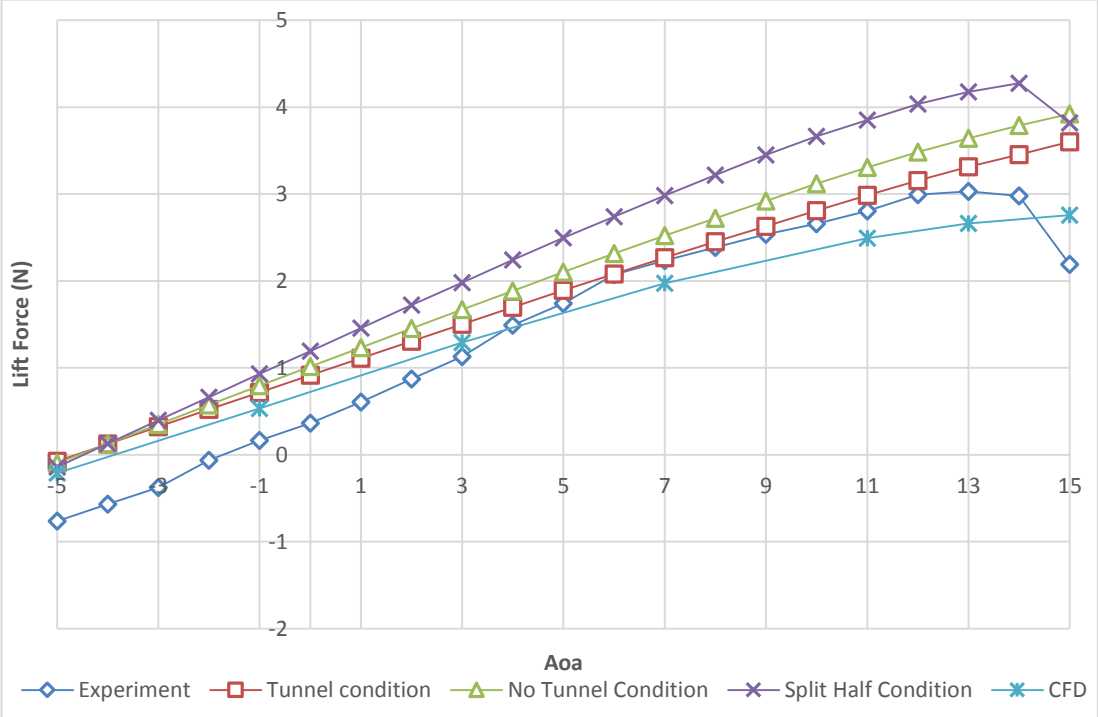

Figure 4-12 Base lift for 11 m/s

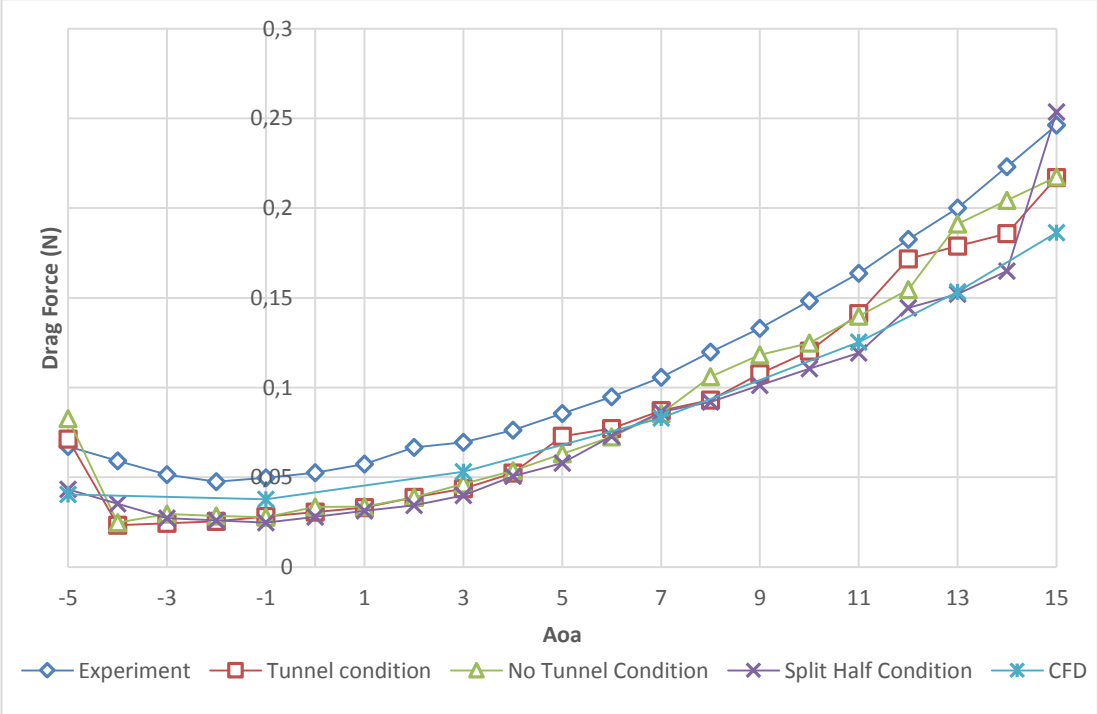

Figure 4-13 Base drag for 11 m/s

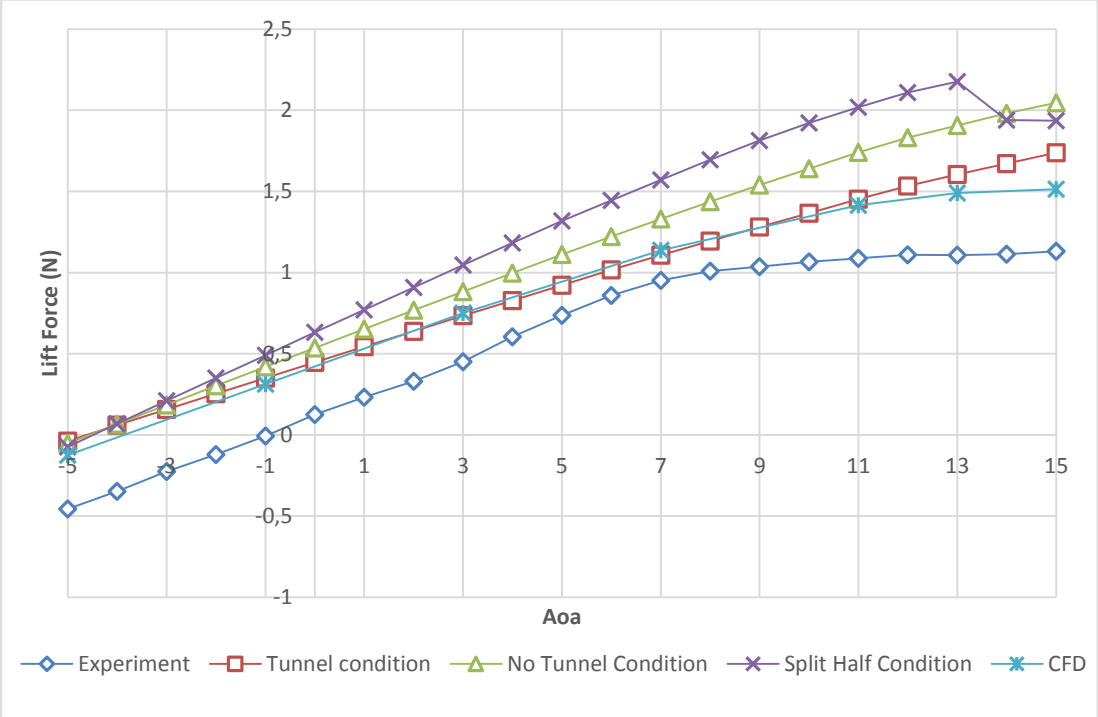

Figure 4-14 Base lift for 12 m/s

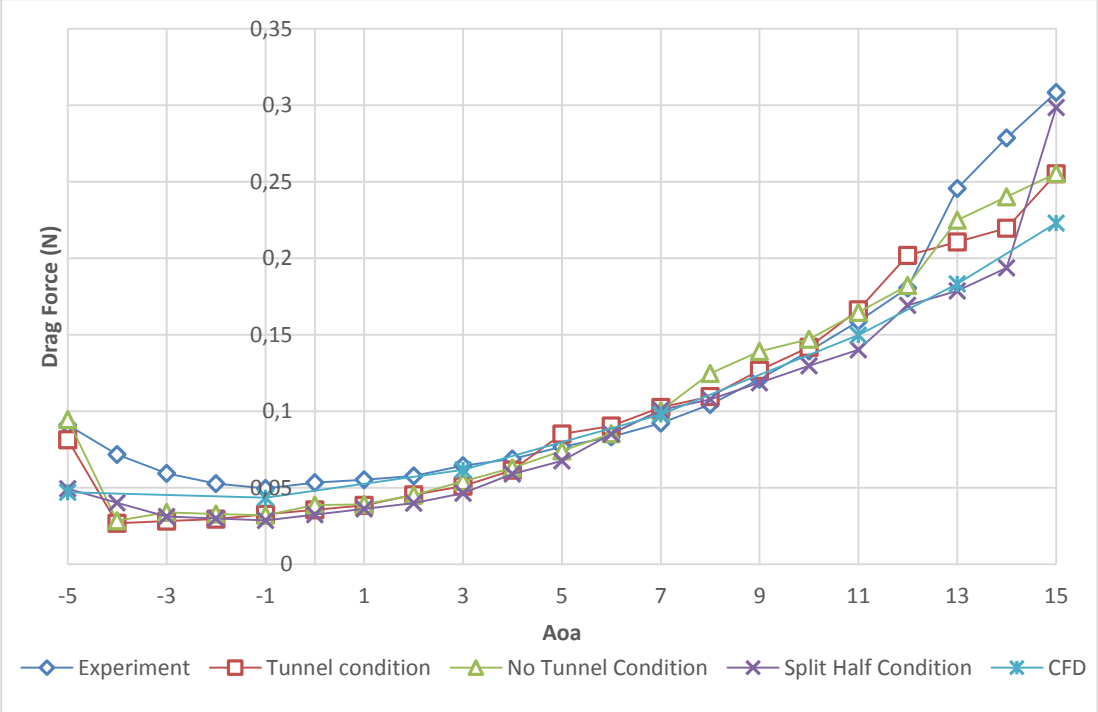

Figure 4-15 Base drag for 12 m/s

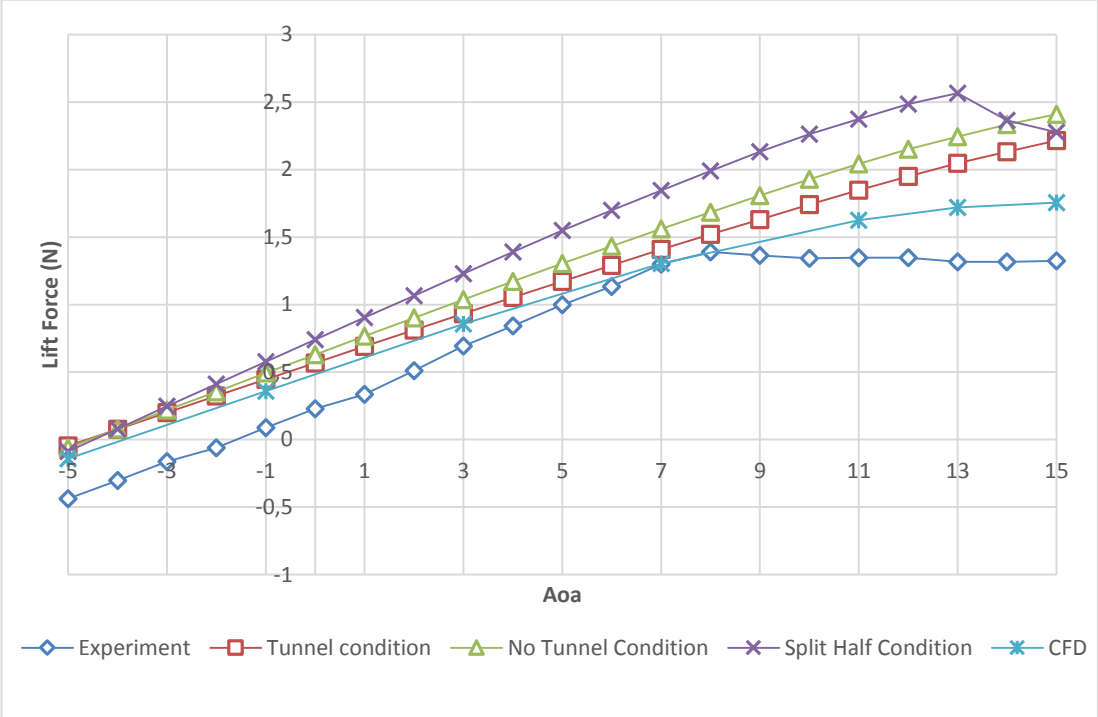

Figure 4-16 Base lift for 13 m/s

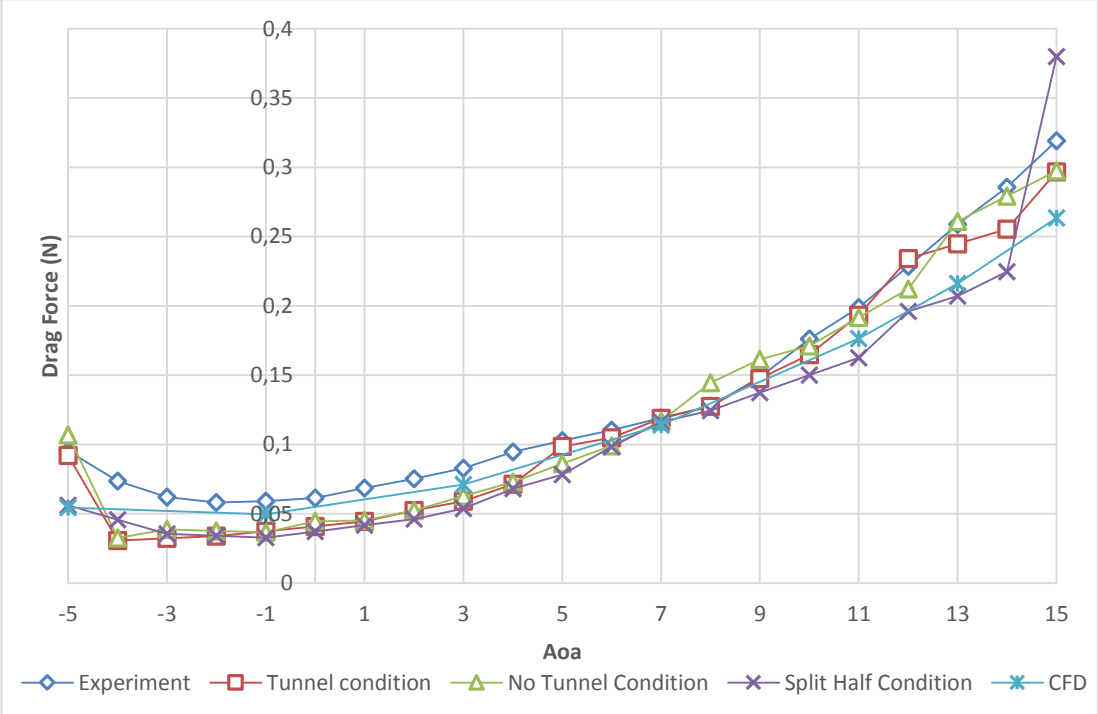

Figure 4-17 Base drag for 13 m/s

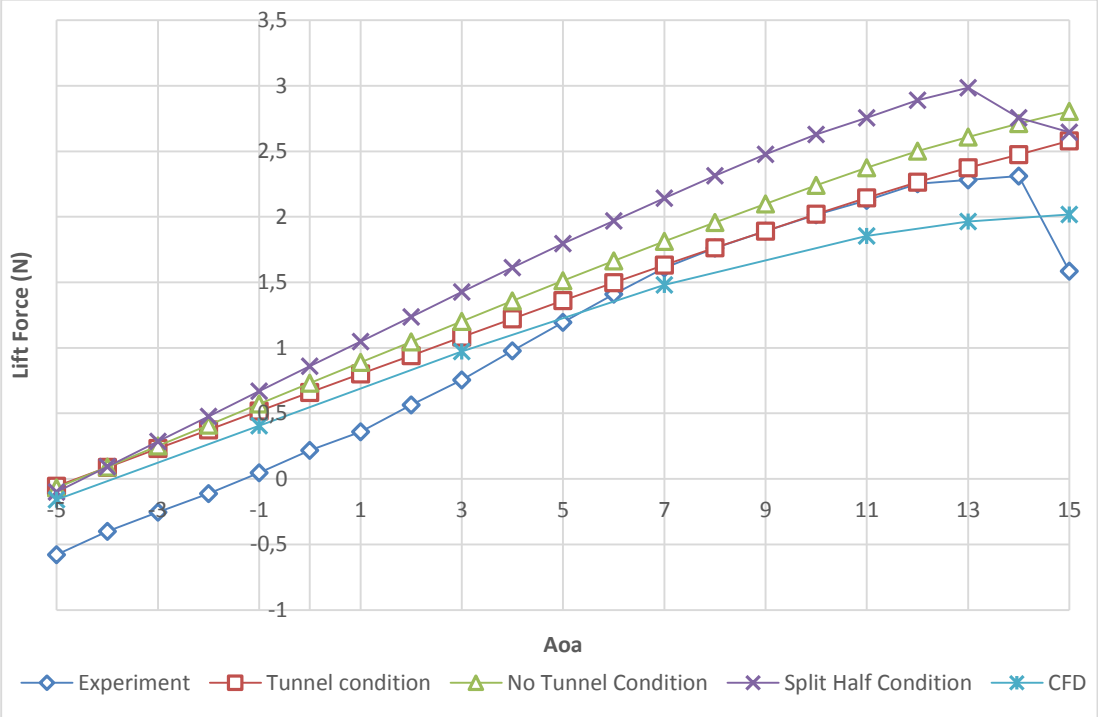

Figure 4-18 Base lift for 14 m/s

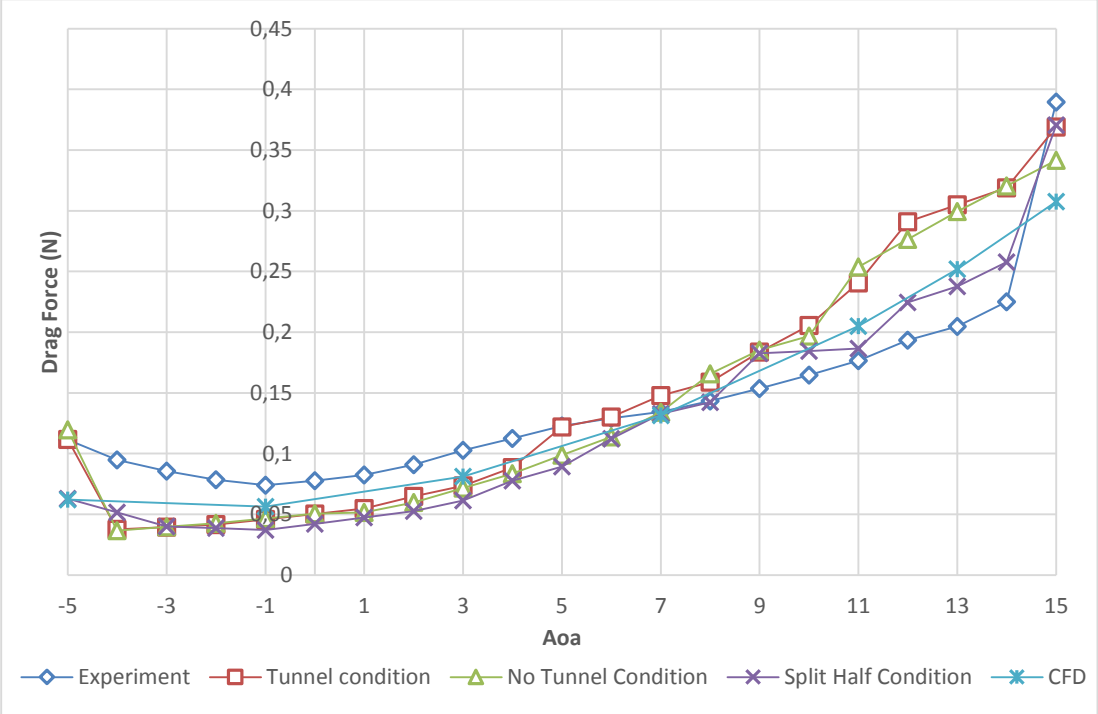

Figure 4-19 Base drag for 14 m/s

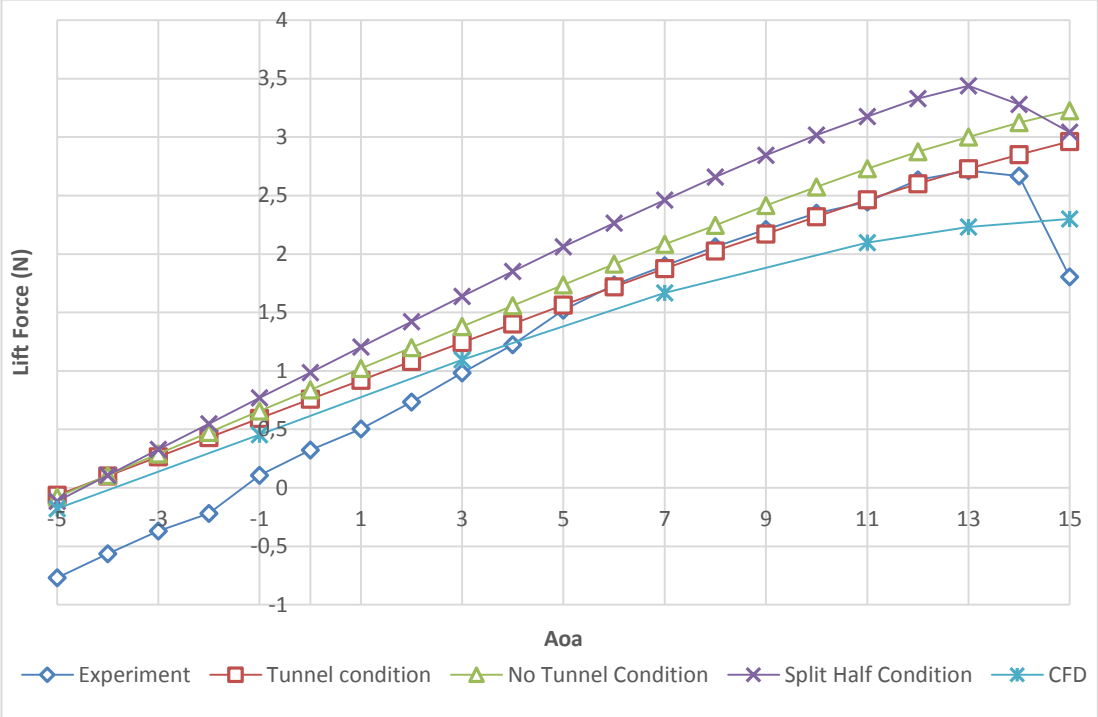

Figure 4-20 Base lift for 15 m/s

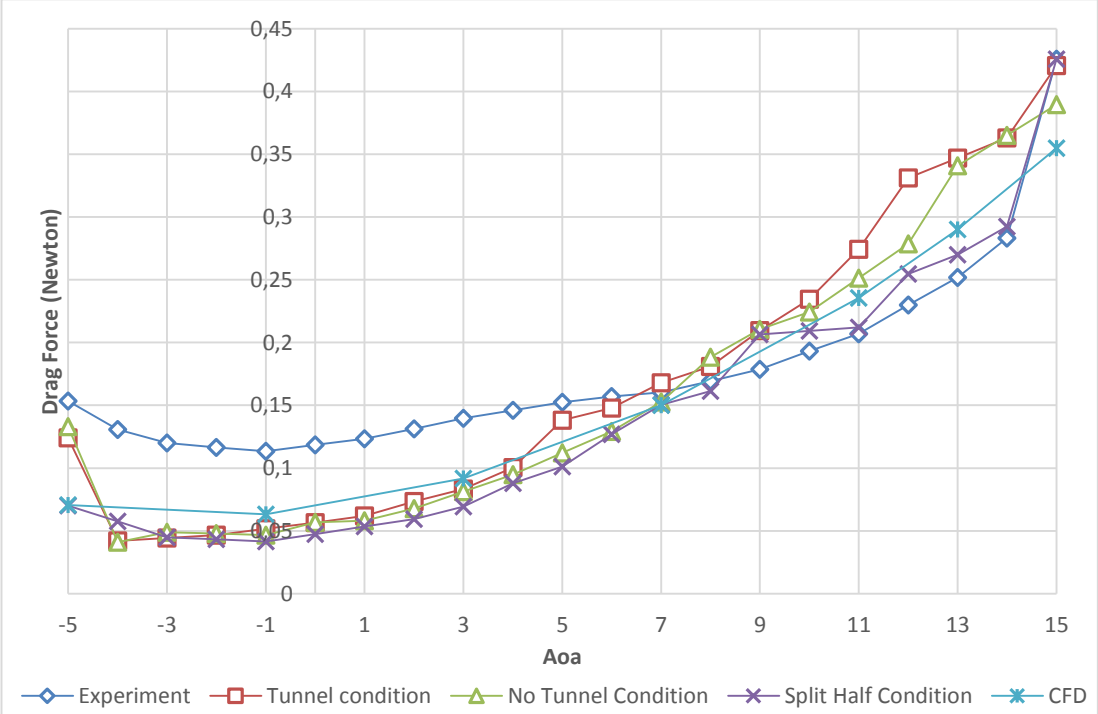

Figure 4-21 Base drag for 15 m/s

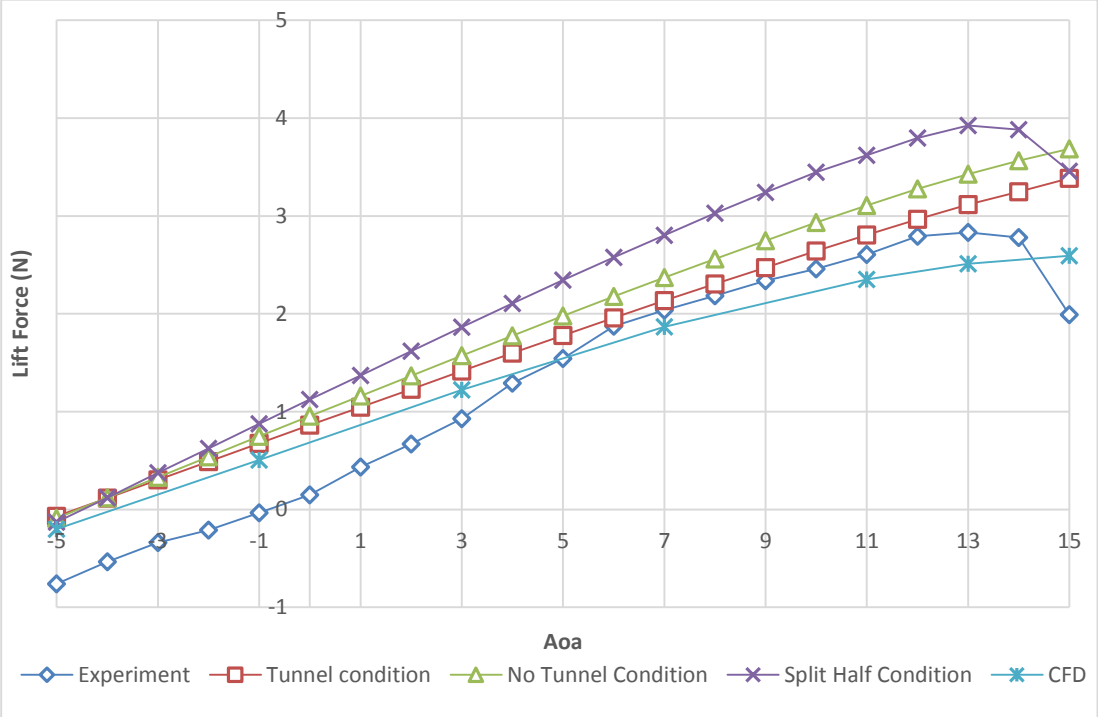

Figure 4-22 Base lift for 16 m/s

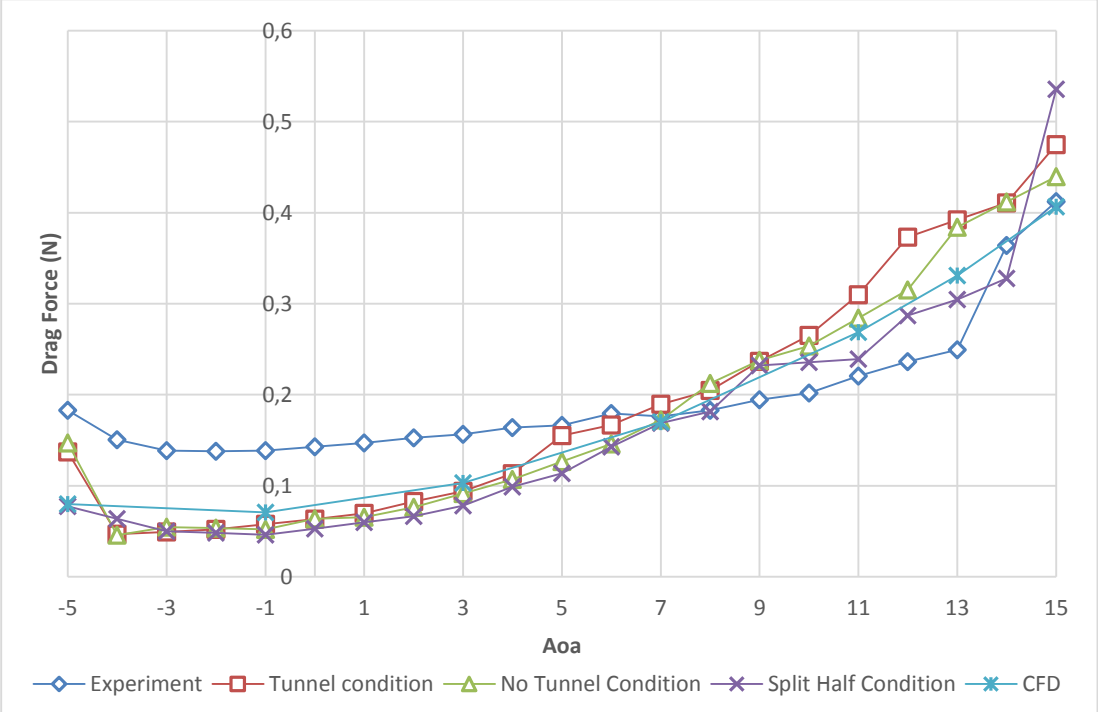

Figure 4-23 Base drag for 16 m/s

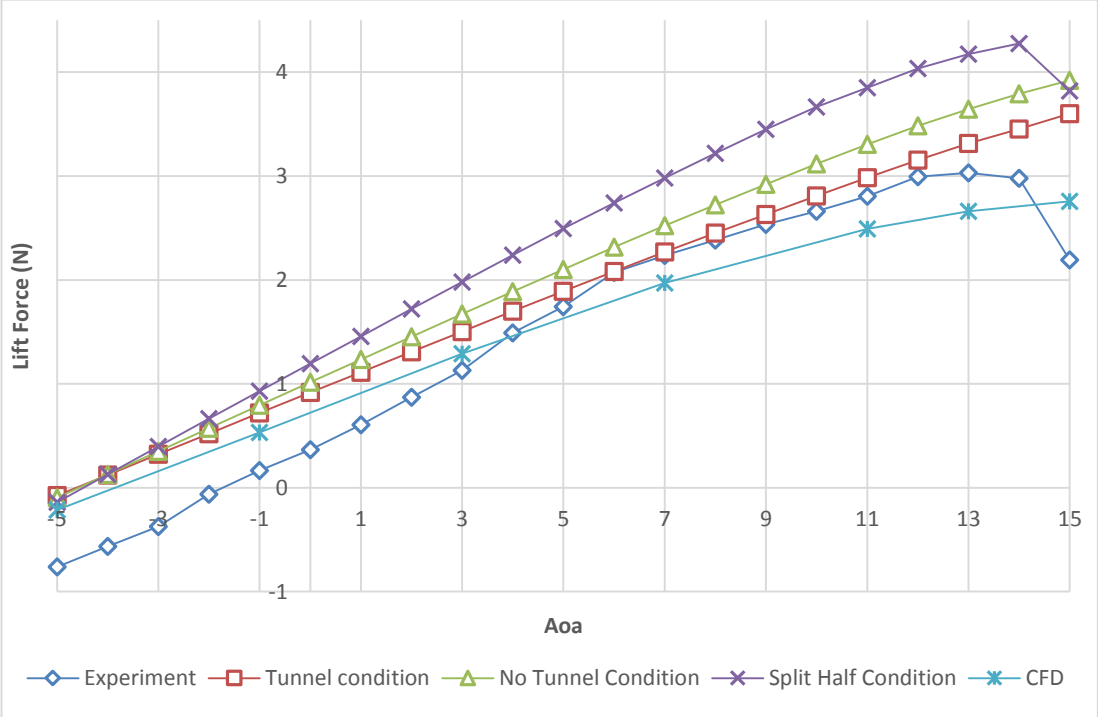

Figure 4-24 Base lift for 16.5 m/s

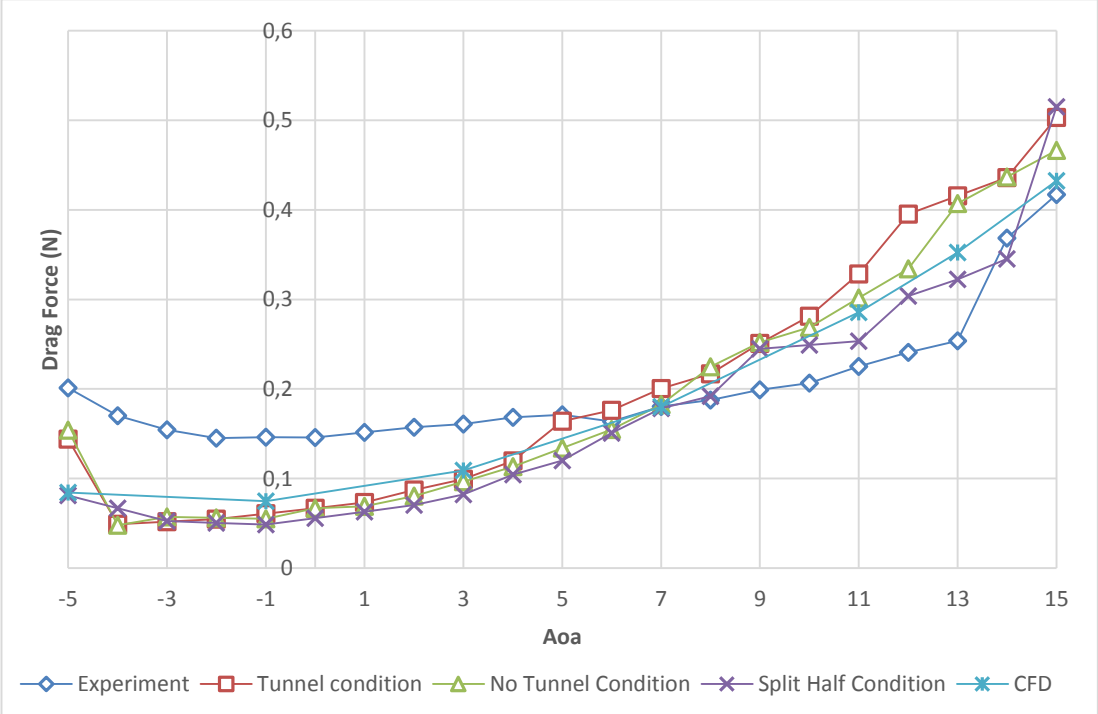

Figure 4-25 Base drag for 16.5 m/s

4.3.2. O14

Besides, the issues mentioned above, abnormality is encountered in the behavior of lift curve slopes of airfoils generated by the optimization tool. This particular phenomenon is called “drop and recovery characteristic of low Re number airfoils”. This incidence is caused by the separation and then reattaching of the flow, named laminar separation bubble. These separation bubbles occur under the influence of adverse pressure gradient, where the laminar boundary layer over the airfoil detaches the airfoil. Then, the flow becomes translational and the separated flow attaches on the airfoil surface again when the sufficient vortex strength of the flow could be attained in the near wall region, as shown in Figure 4-26 . This phenomenon is called “laminar separation bubble (LSB)”. Such incidences generally occur when the adverse pressure gradient is higher or when the airfoil geometry changes suddenly, such as the cases with trailing edge and leading edge of the airfoil. In detail, laminar boundary layer is compelled to separate, because due to the inadequacy in flow momentum, the effects of traverse adverse pressure gradients could not be undone. These types of separated boundary layers are defined as free shear layers and they are extremely unstable [48]. Such bubbles are commonly experienced in thin airfoils of micro air vehicles at low Re number like 10^4 to 10^6 [44].

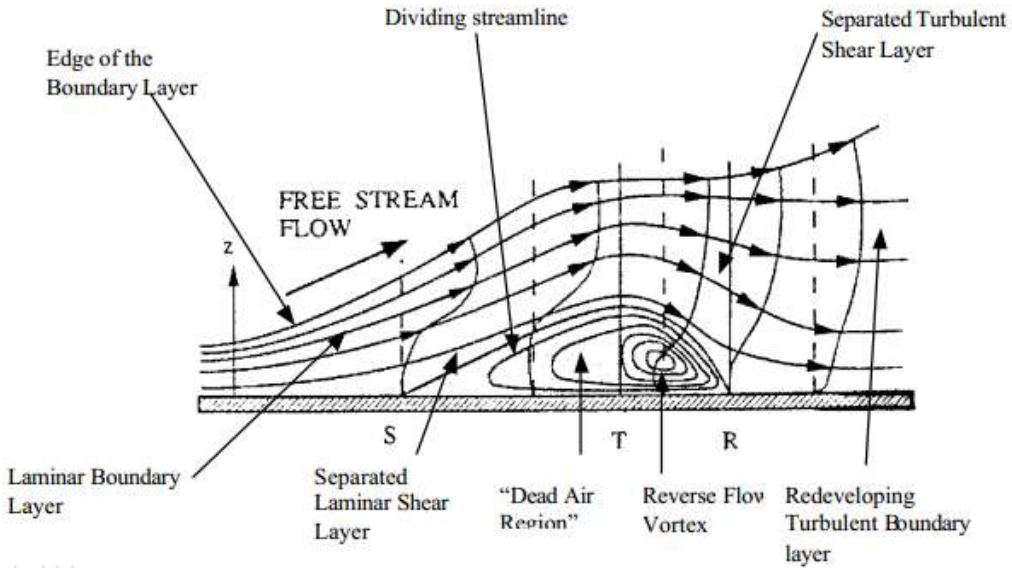

Figure 4-26 Laminar Separation Bubble [45]

Laminar separation bubbles have influence over airfoils' lift parameters because of the alteration of pressure gradient on upper or lower surfaces of airfoils in the chord-wise direction. The pressure alteration causes abnormal behavior in lift coefficient as shown in Figure 4-27. This is the exact phenomena that is experienced through experimenting on optimized and morphing wing configurations. Due to the trend of the lift curve slope, this issue is named as "recover lift curve slope". This situation can be seen in Figure 4-34, Figure 4-36, Figure 4-38, Figure 4-64 and Figure 4-68. Also, the recovering of the laminar separation bubble can be deducted from the graphs as the airspeed velocity and Reynolds number increase. This is the reason why it is not the case for M10 wing configuration. Among the all of the wing configurations, M10 has the biggest Reynolds number.

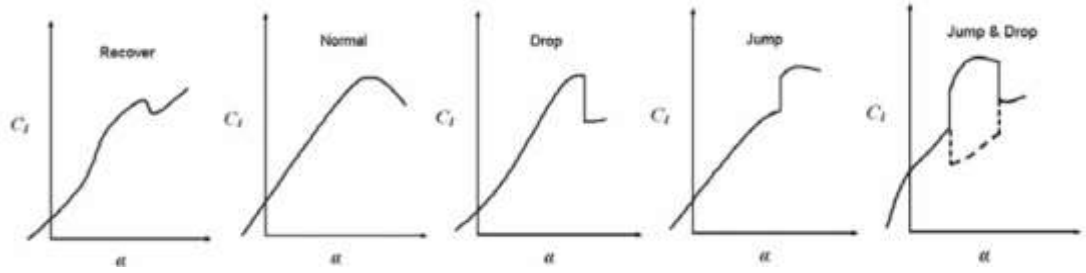

Figure 4-27 Classification of lift curve slopes [45]

Lee et .al. investigated this issue in terms of airfoil parameters for camber location and leading edge radius. Their numerical study indicates that camber is the dominating factor in recovery-type lift curve slopes, as well as back cusps of airfoil and the leading edge radius influences the character of lift curve slope [45]. This can be one of the reason why separation of the flow is only experienced in optimized wing configurations but not in baseline configuration. It is worthy to note that airfoil products of the design tool have more camber and their maximum camber point location is afore when compared to the baseline airfoil. The airfoil design parameters are the main parameters that should be added into the optimization tool as constraints. Moreover, the optimization tool is programmed to reattach the flow if separation occurs before the expected locations which is another constraints input to the code.

For the fixed optimized wing configuration, experimental results of lift and drag forces agree with the numerical results for high angles of attack, especially for the tunnel

condition. This is a proof of optimization tool's robustness except separation and low angle of attack conditions. If experimental issues at low angles of attack could be resolved, the curves obtained from tunnel condition and experimental result are expected to overlap for moderate Reynolds numbers.

In addition, CFD and optimization tool overpredict the drag force at moderate angles of attack and at low speeds as shown in Figure 4-37. Over-prediction of drag is acceptable for such low Reynolds number solutions.

Unfortunately, 16 m/s and 16.5 m/s experiments could not be performed for this particular wing configuration due to the technical issues with the wind tunnel's motor.

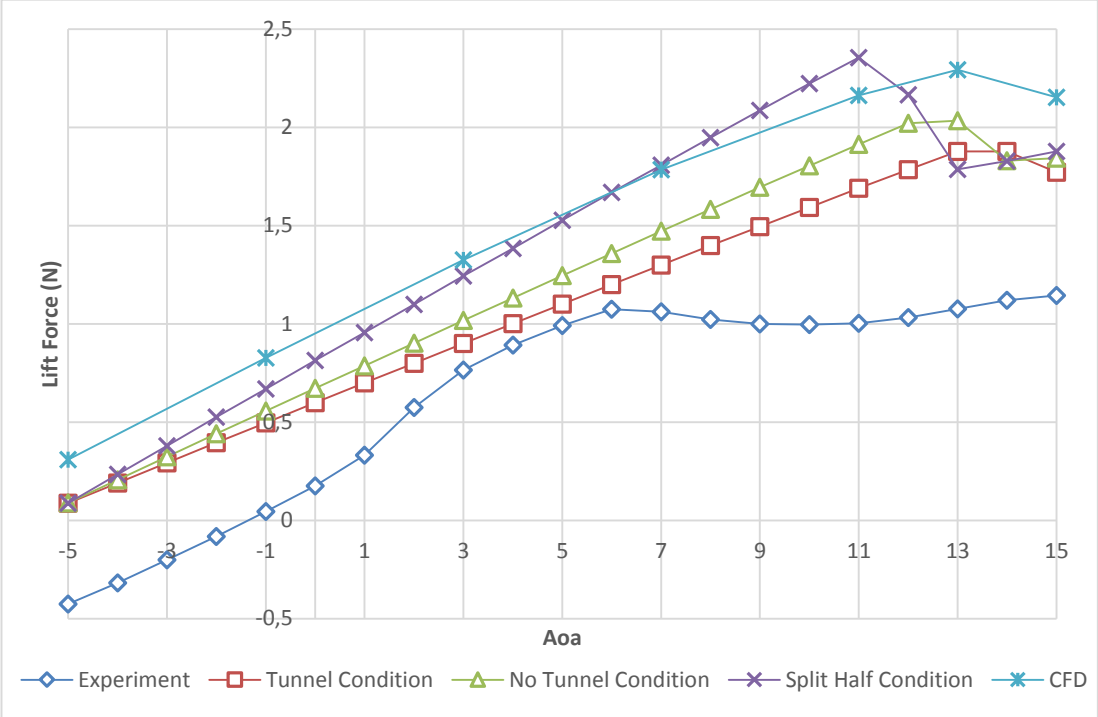

Figure 4-28 O14 lift results for 10 m/s

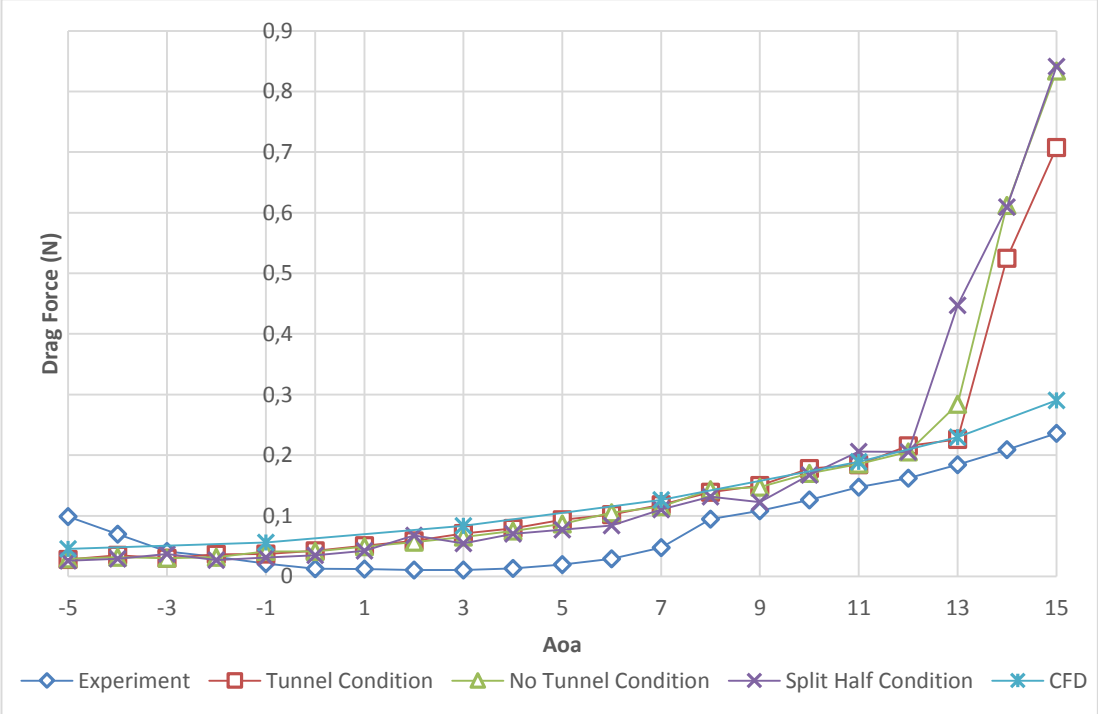

Figure 4-29 O14 drag results for 10 m/s

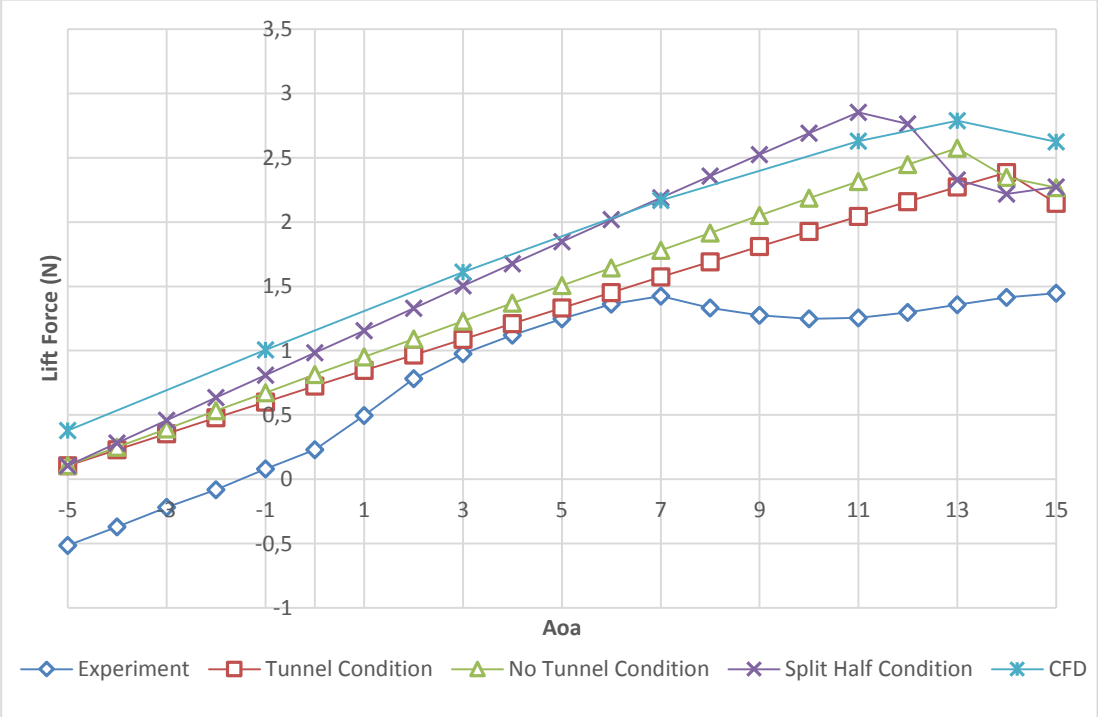

Figure 4-30 O14 lift results for 11 m/s

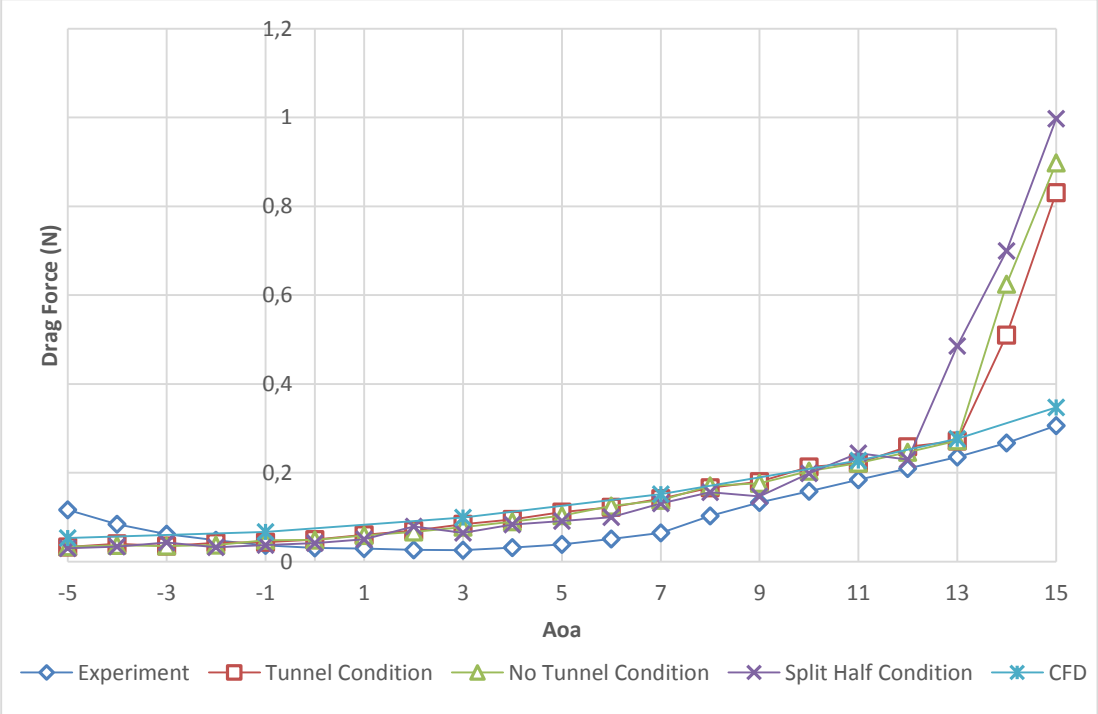

Figure 4-31 O14 drag results for 11 m/s

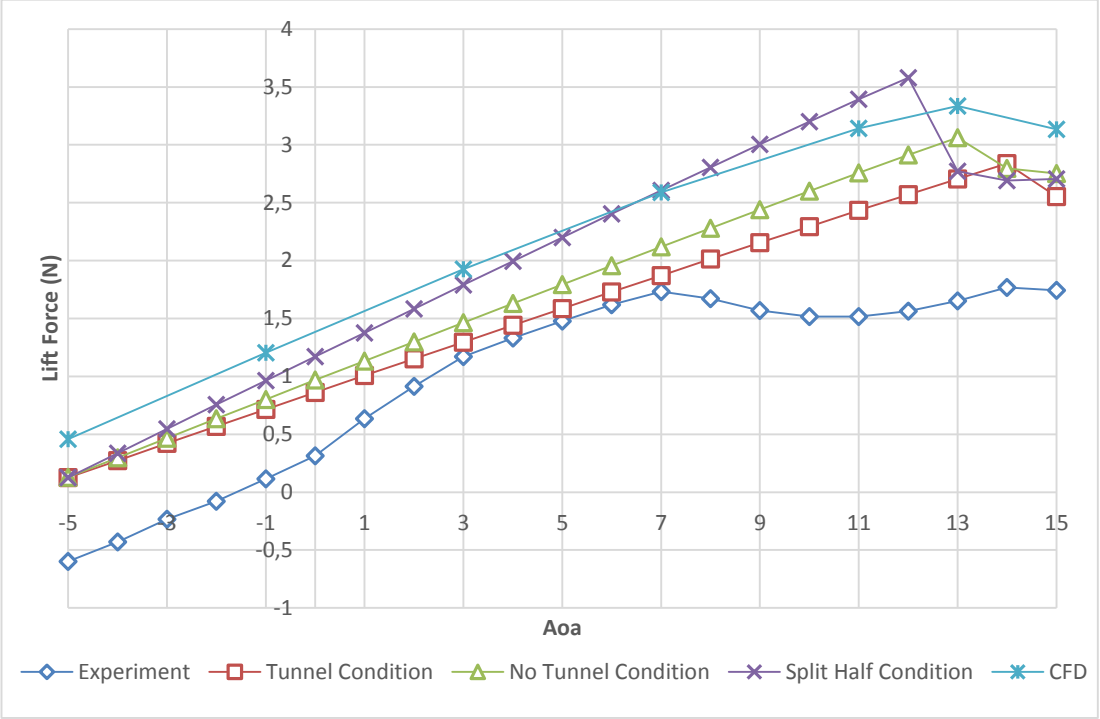

Figure 4-32 O14 lift results for 12 m/s

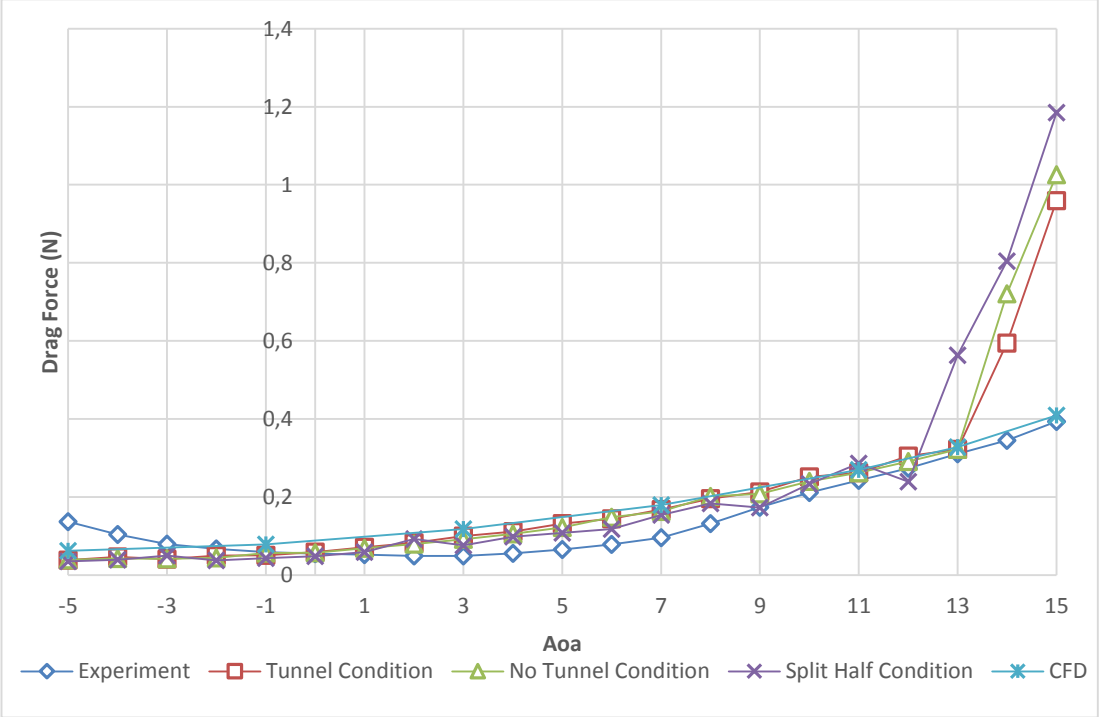

Figure 4-33 O14 lift results for 12 m/s

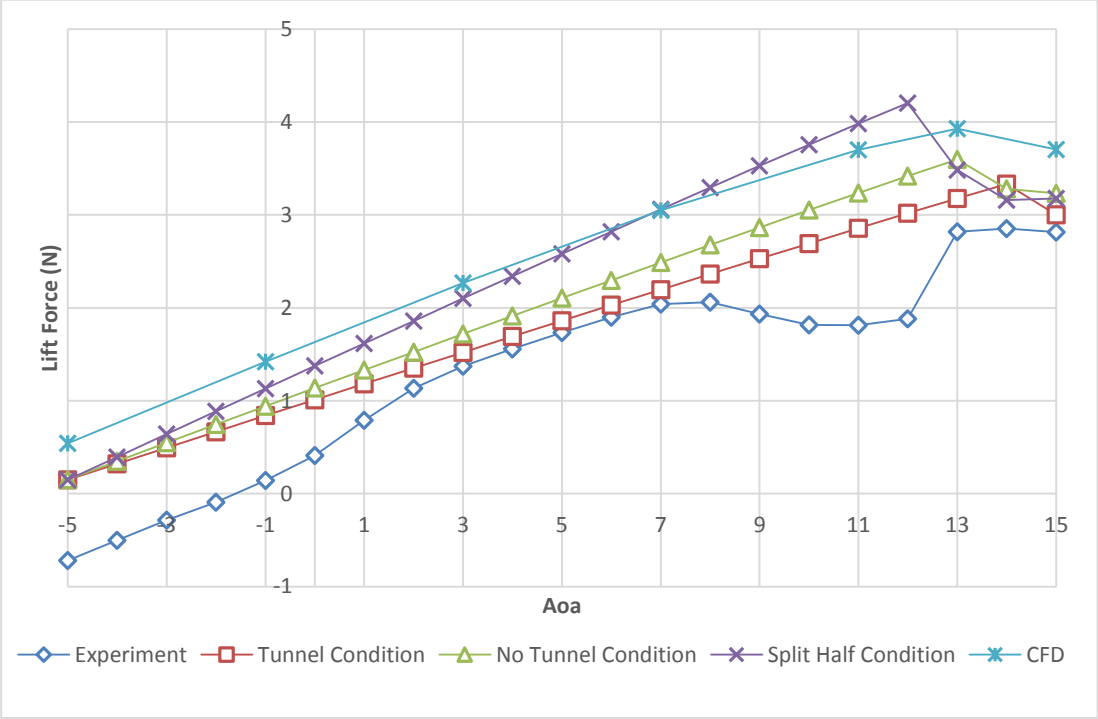

Figure 4-34 O14 lift results for 13 m/s

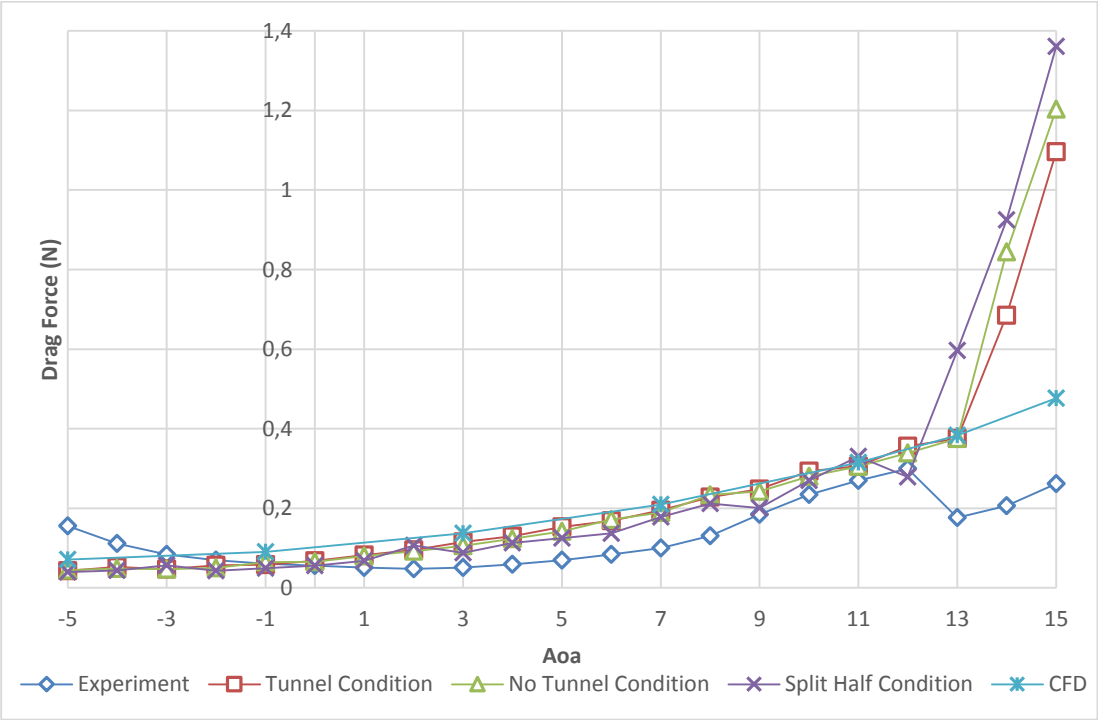

Figure 4-35 O14 drag results for 13 m/s

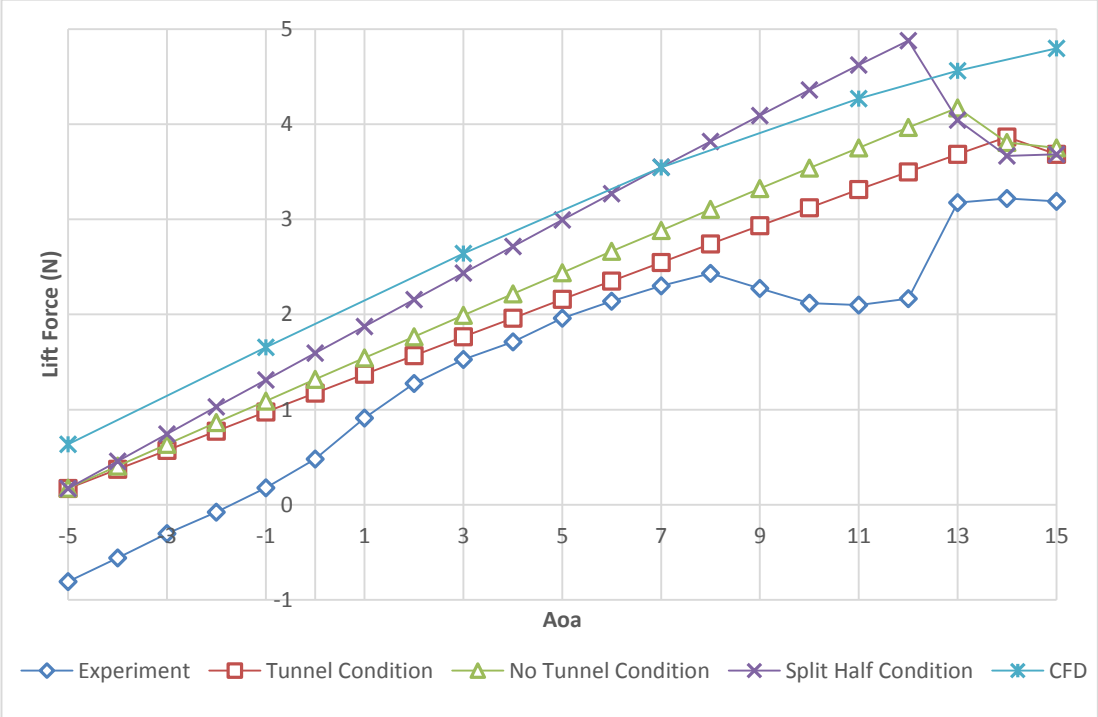

Figure 4-36 O14 lift results for 14 m/s

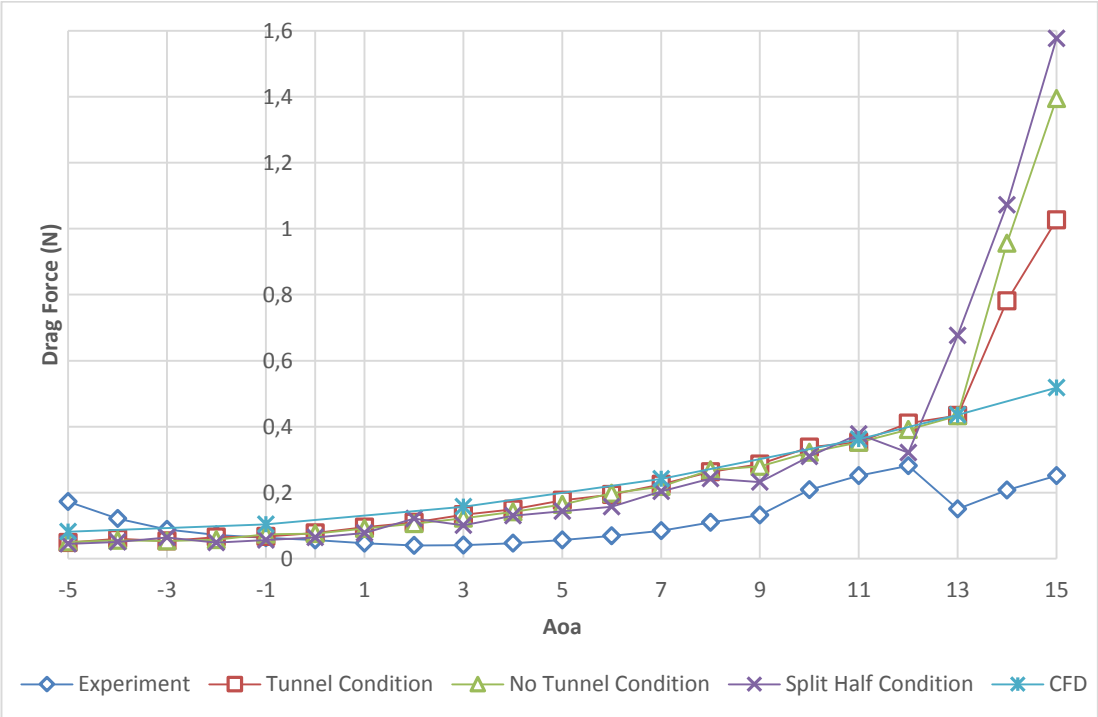

Figure 4-37 O14 drag results for 14 m/s

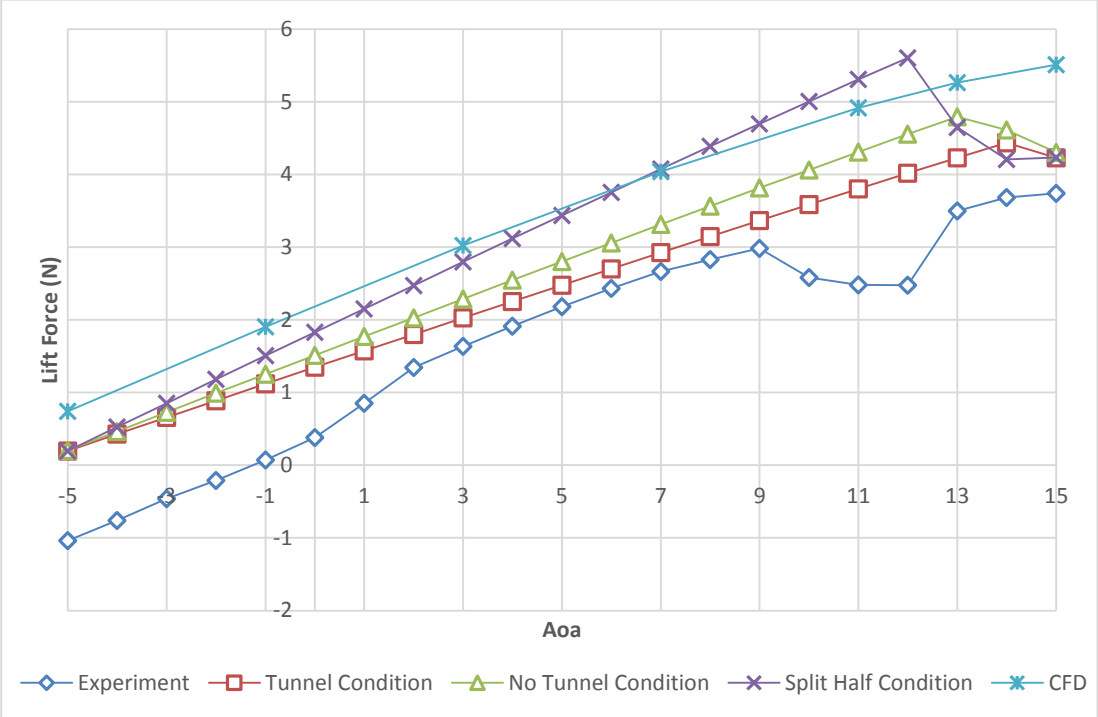

Figure 4-38 O14 lift results for 15 m/s

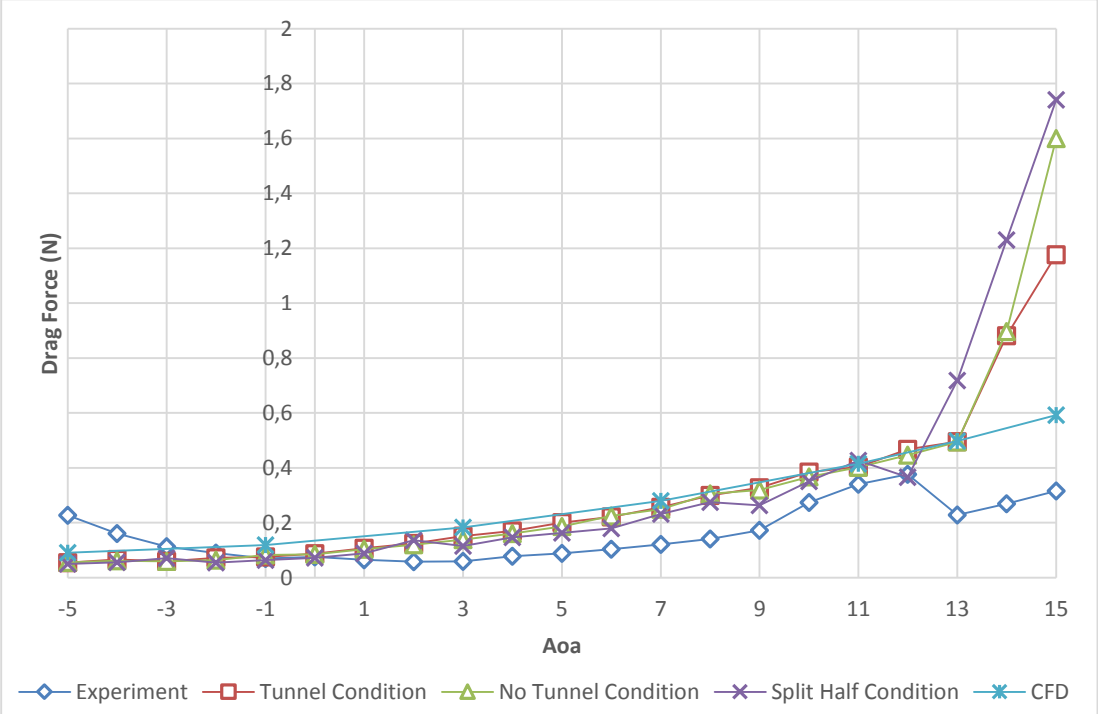

Figure 4-39 O14 drag results for 15 m/s

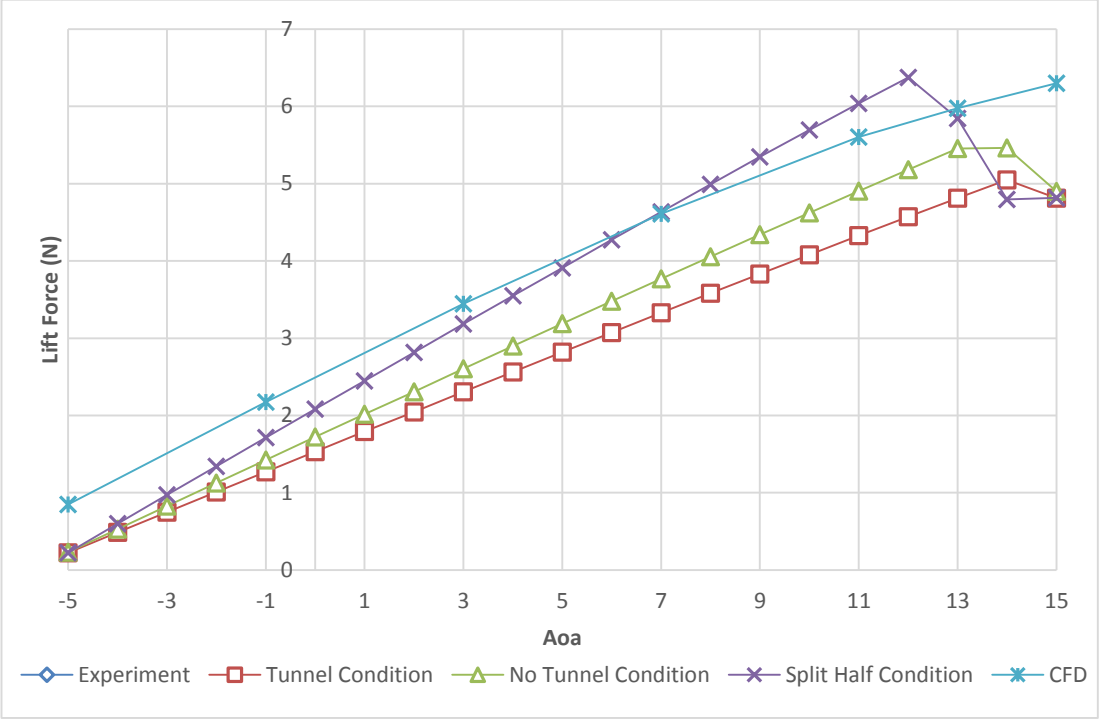

Figure 4-40 O14 lift results for 16 m/s

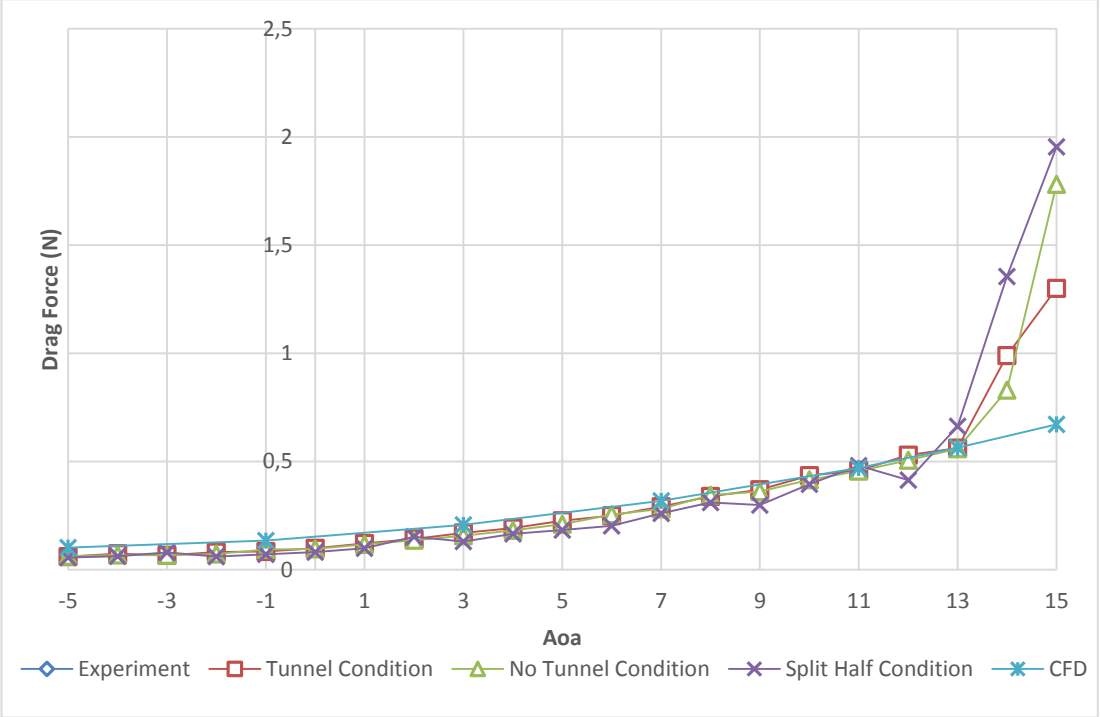

Figure 4-41 O14 drag results for 16 m/s

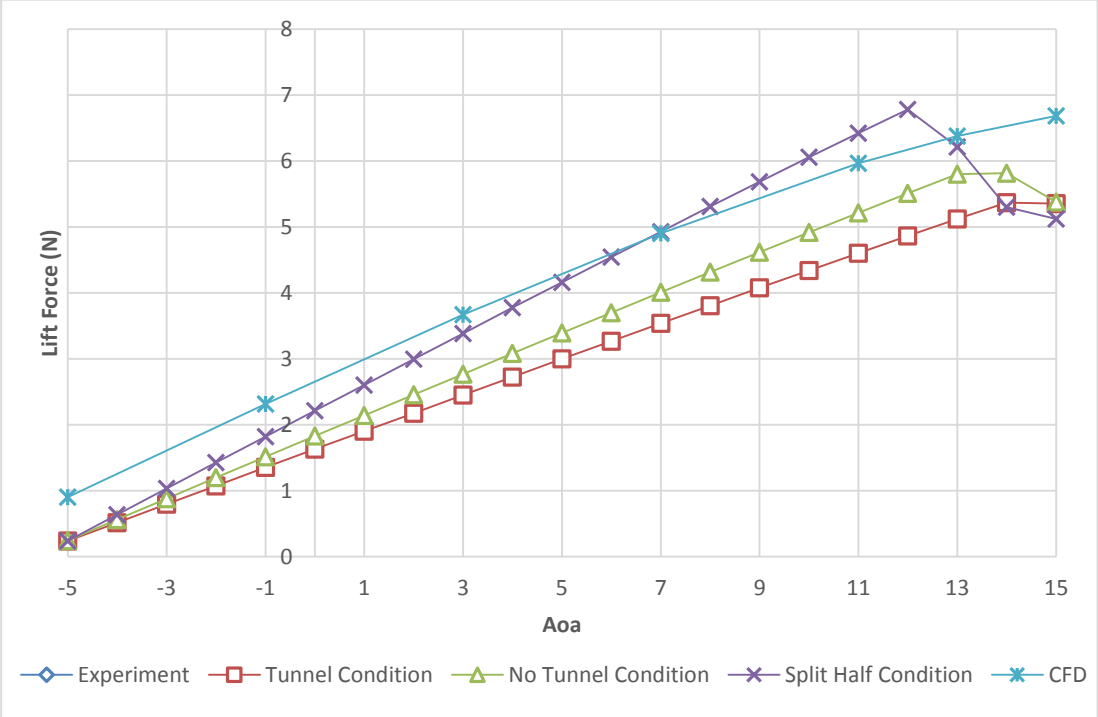

Figure 4-42 O14 lift results for 16.5 m/s

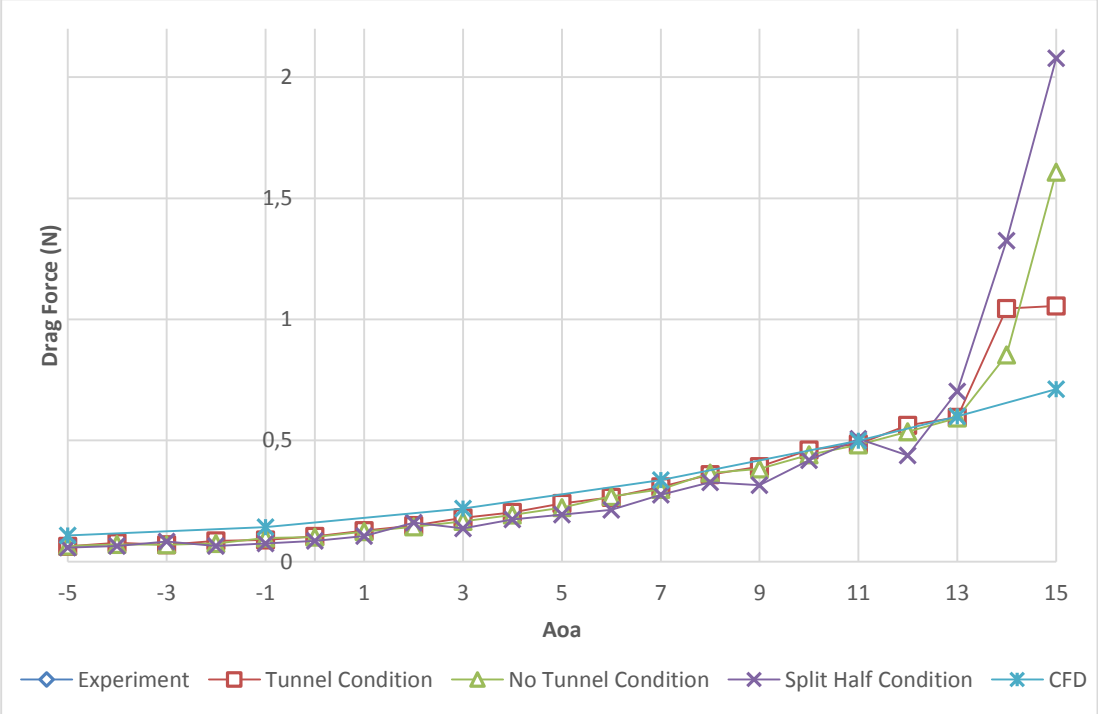

Figure 4-43 O14 drag results for 16.5 m/s

4.3.3. M10

10 m/s Morphing wing configuration yields the most compatible results with the "Tunnel Condition" results with the exceptions of lift curve slope differences at low angles of attack and early separation issues, among all wing configurations This compatibility occurs as a consequence of 10m/s morphing wing having the biggest planform area and the highest Reynolds number which is ranging from 62,000 to 102,000.

Early stall characteristics are represented for this cases at comparably low Reynolds numbers seen in Figure 4-44 and Figure 4-46. This issue occurs due to transition of the flow to turbulent flow [45]. Whereas, drag curve trends show dissimilarity at moderate angle of attacks shown in Figure 4-45 and Figure 4-47.

As the Reynolds numbers have greater values than 70,000, experimental results draw an excellent lift curve trend which are matching with the tunnel conditions except the low angle of attack region. This issue can be explained by having extensive laminar flow at Reynolds numbers ranging 70,000 to 200,000. Therefore, airfoil performance enhances [45] and aerodynamic forces become more predictable by the numerical tools. These graphs can be seen in Figure 4-48, Figure 4-50, Figure 4-52, Figure 4-54, Figure 4-56 and Figure 4-58. Besides, drag overprediction is still an issue that is experienced in many cases for the corresponding drag curves shown in Figure 4-49, Figure 4-51, Figure 4-53, Figure 4-55, Figure 4-57 and Figure 4-59.

To sum up, for the lift results, CFD, optimization tool and experimental results match well with each other except some minor defects. Discrepancies between Tunnel Condition and experimental results can be explained by the imperfection of wind tunnel and the manufacturing as well as the boundary layer effects originating from walls of the tunnel.

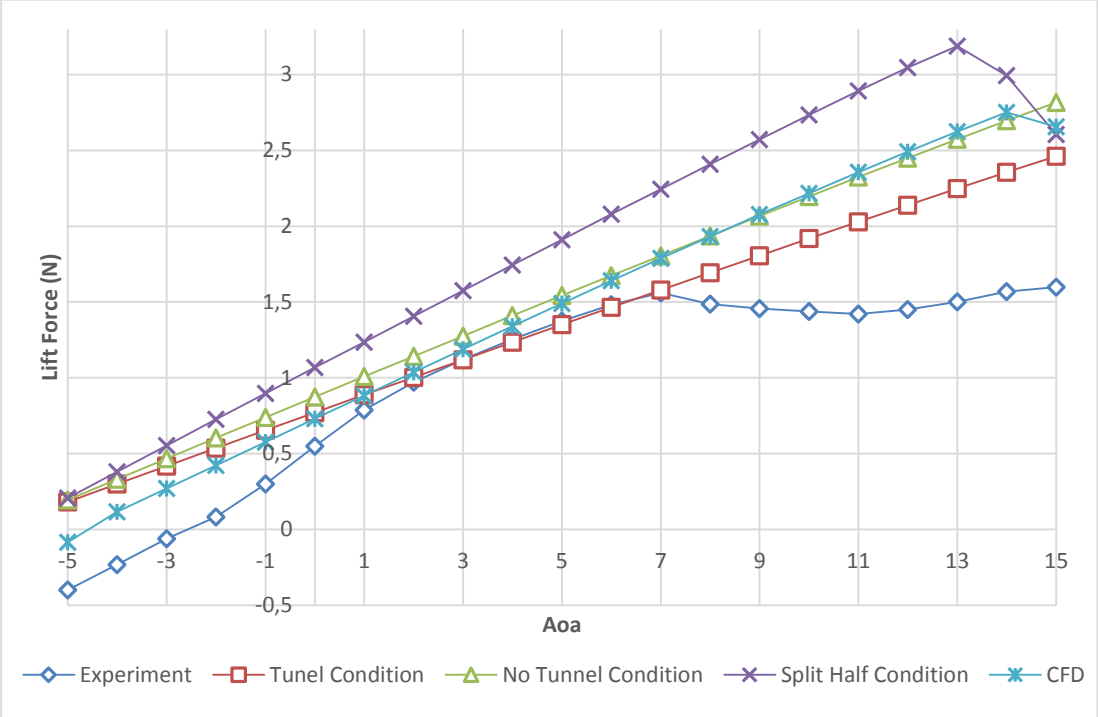

Figure 4-44 M10 lift results for 10 m/s

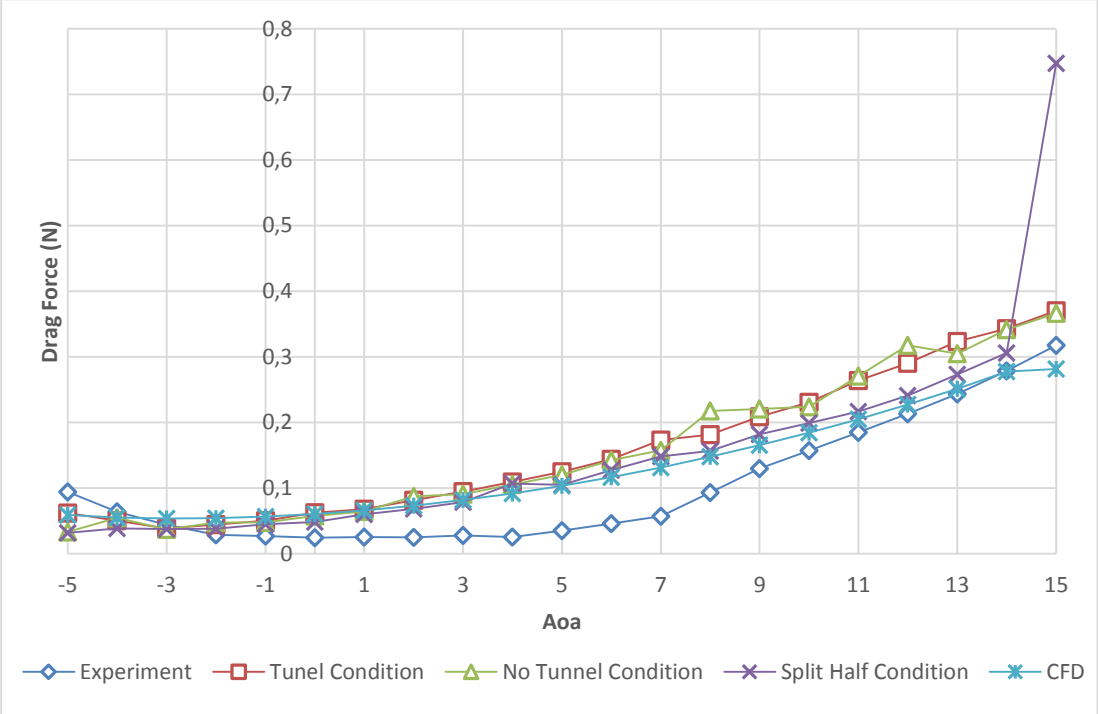

Figure 4-45 M10 drag results for 10 m/s

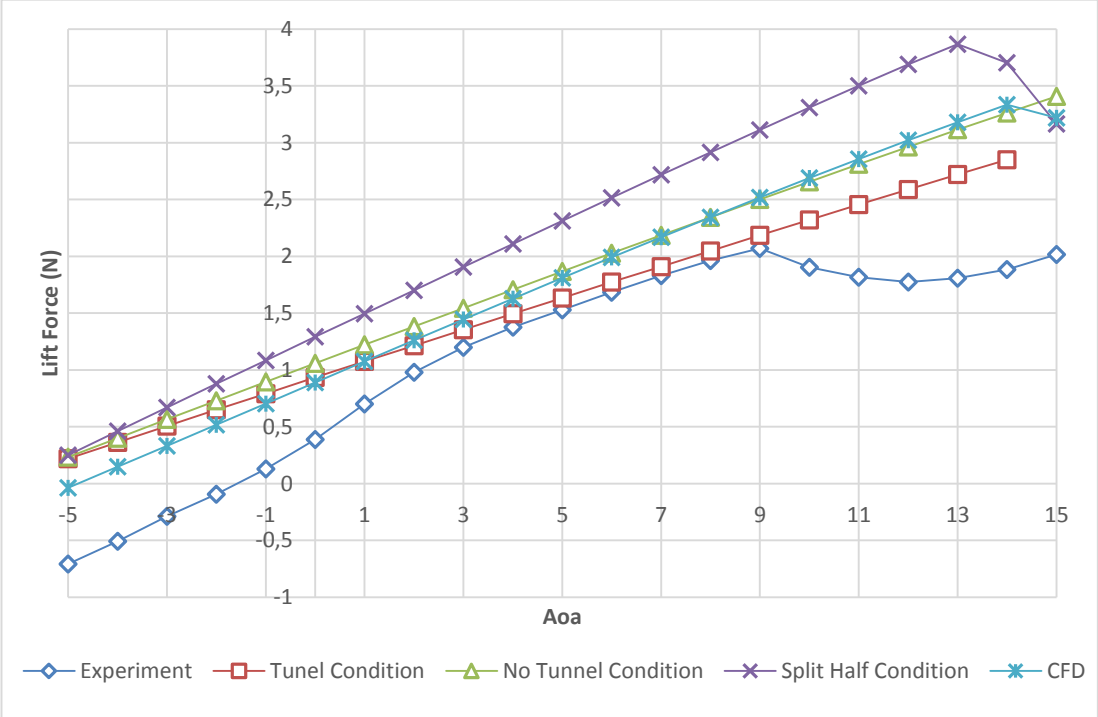

Figure 4-46 M10 lift results for 11 m/s

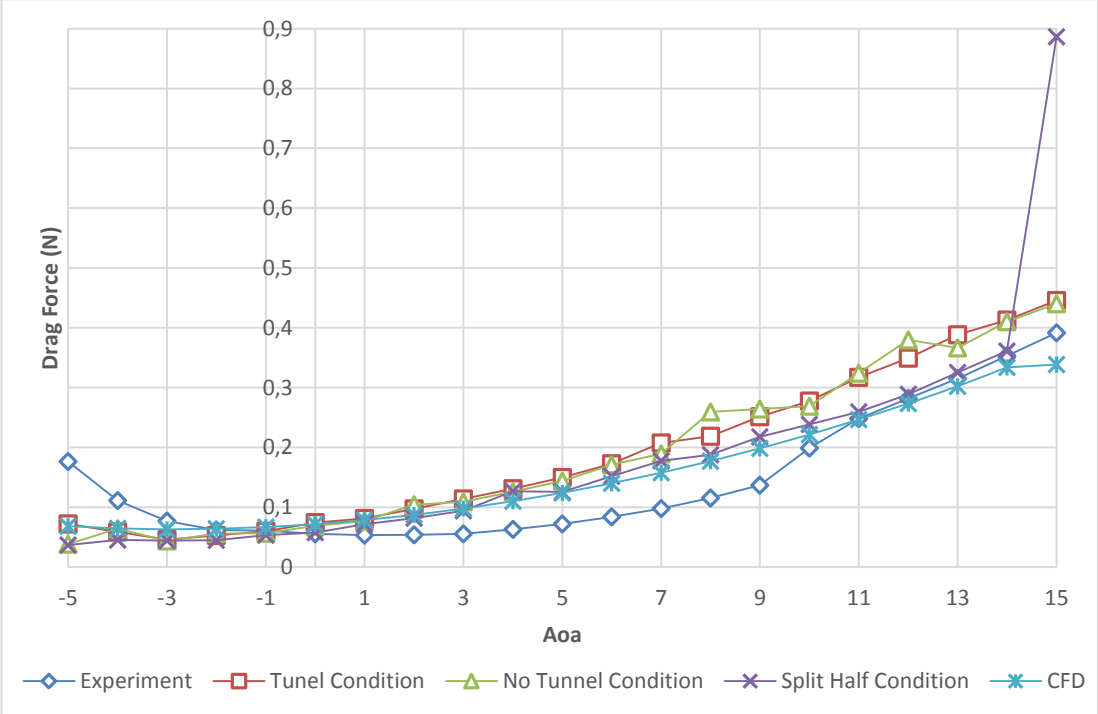

Figure 4-47 M10 drag results for 11 m/s

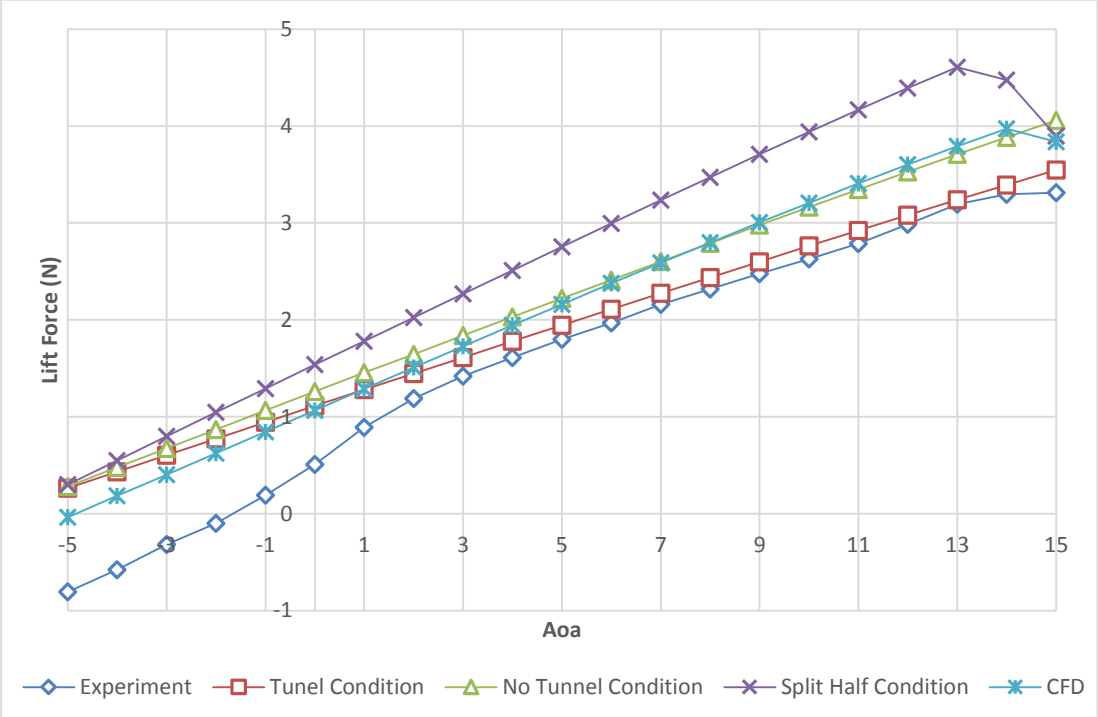

Figure 4-48 M10 lift results for 12 m/s

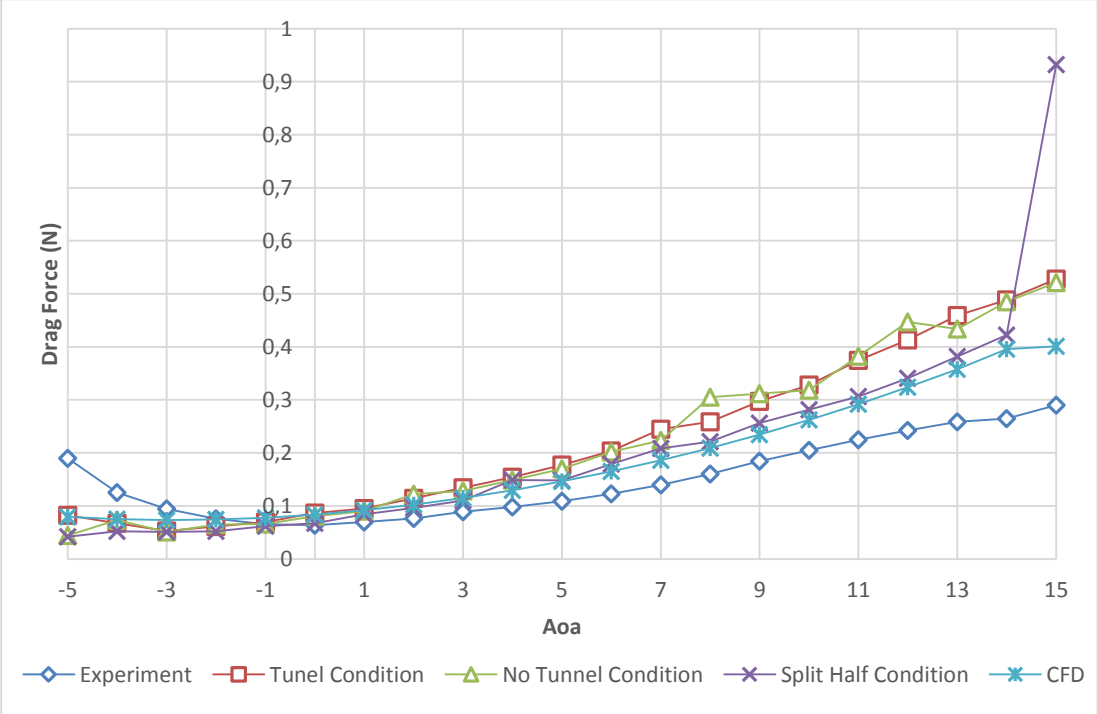

Figure 4-49 M10 drag results for 12 m/s

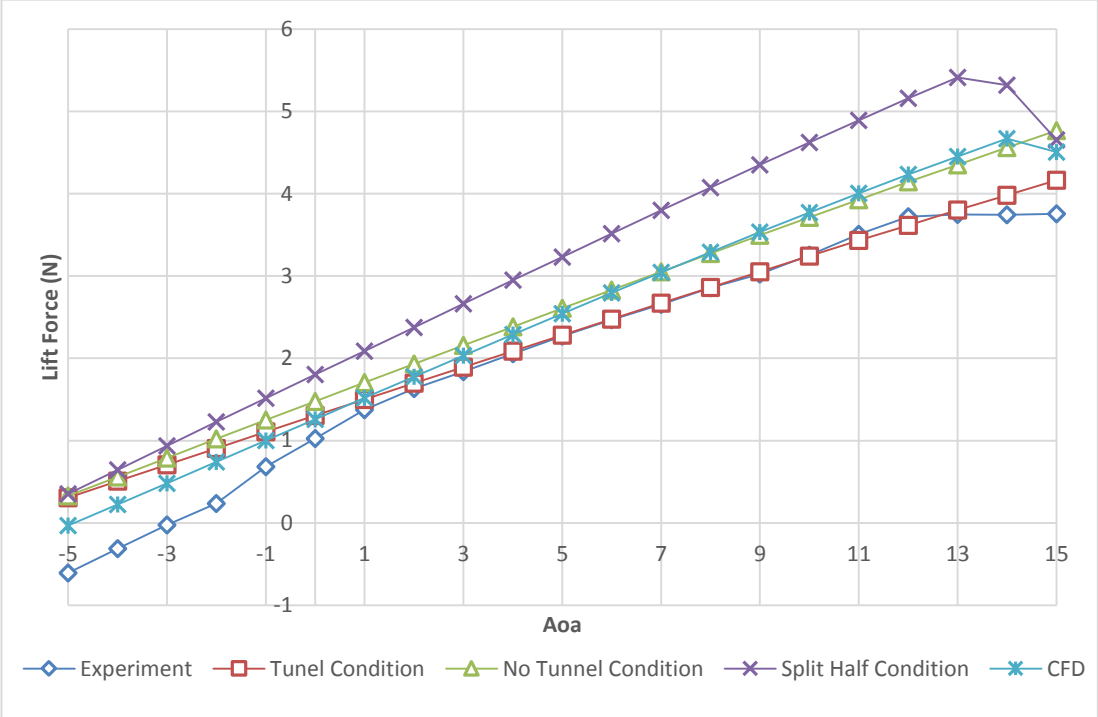

Figure 4-50 M10 lift results for 13 m/s

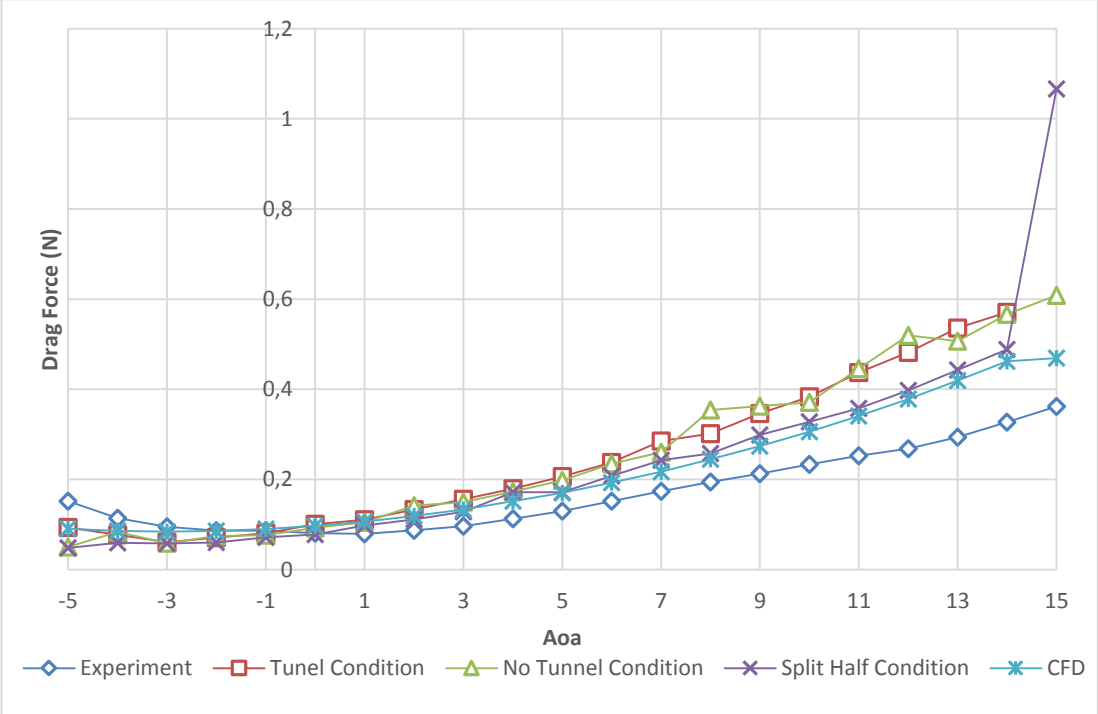

Figure 4-51 M10 drag results for 13 m/s

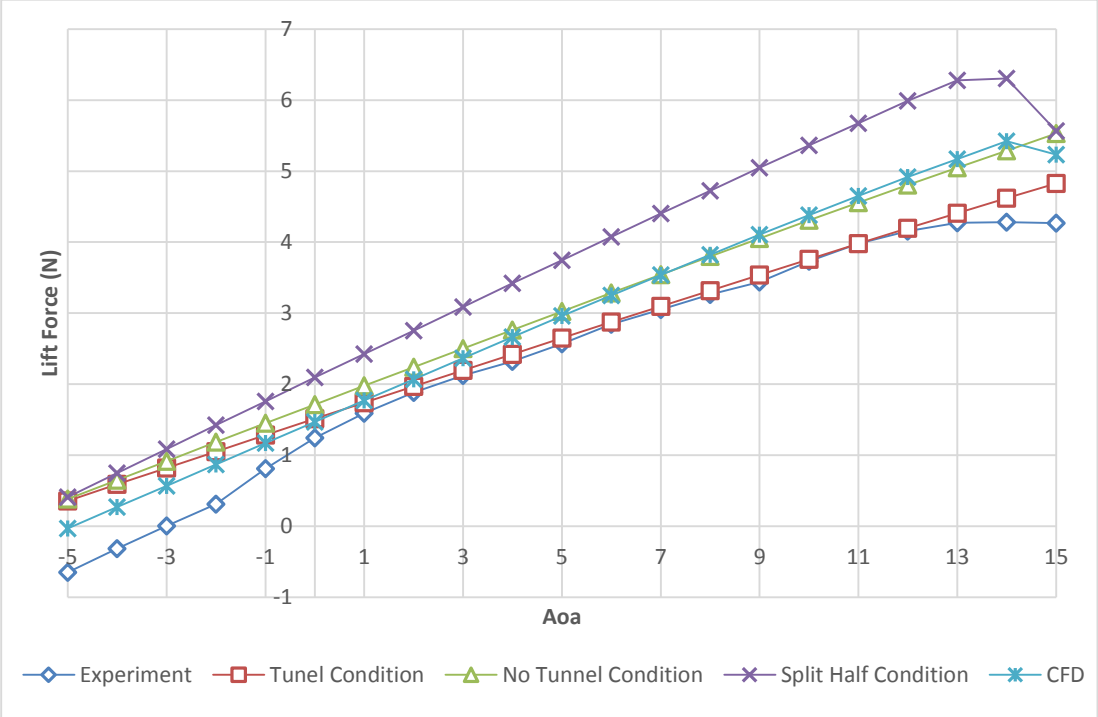

Figure 4-52 M10 lift results for 14 m/s

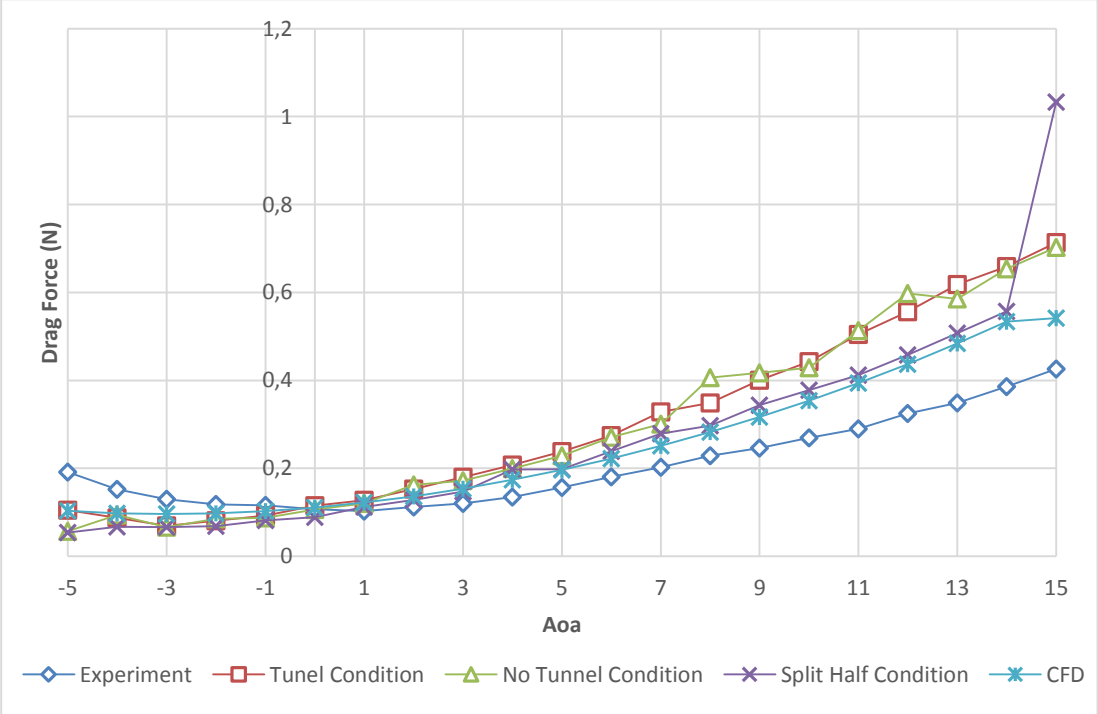

Figure 4-53 M10 drag results for 14 m/s

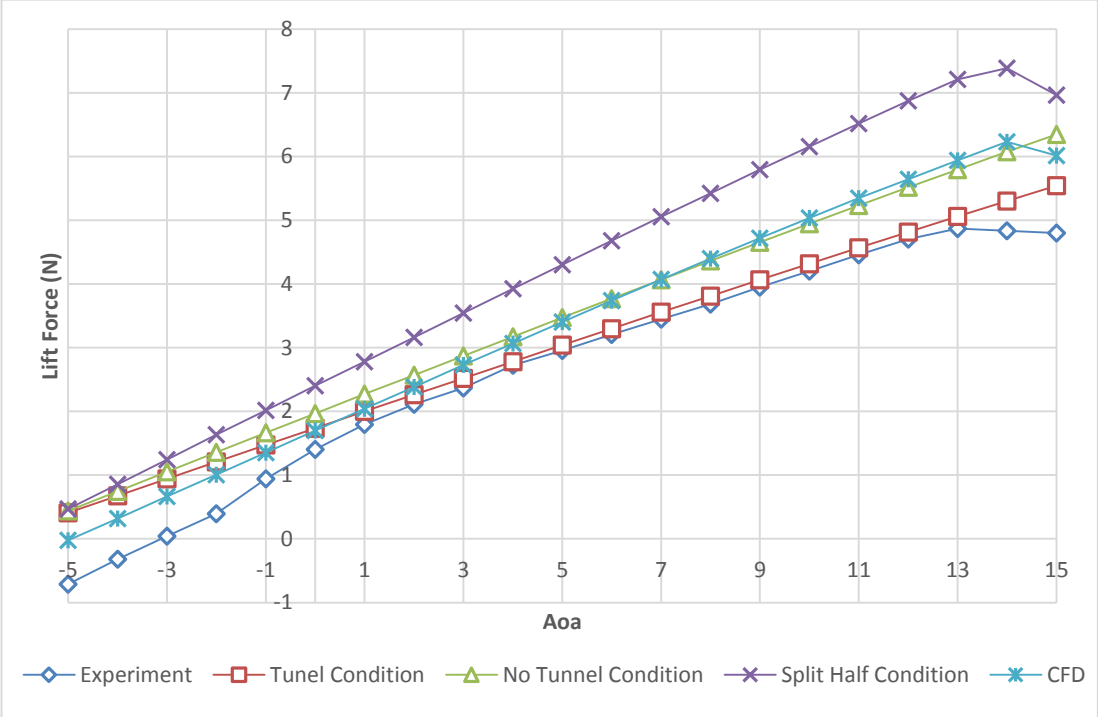

Figure 4-54 M10 lift results for 15 m/s

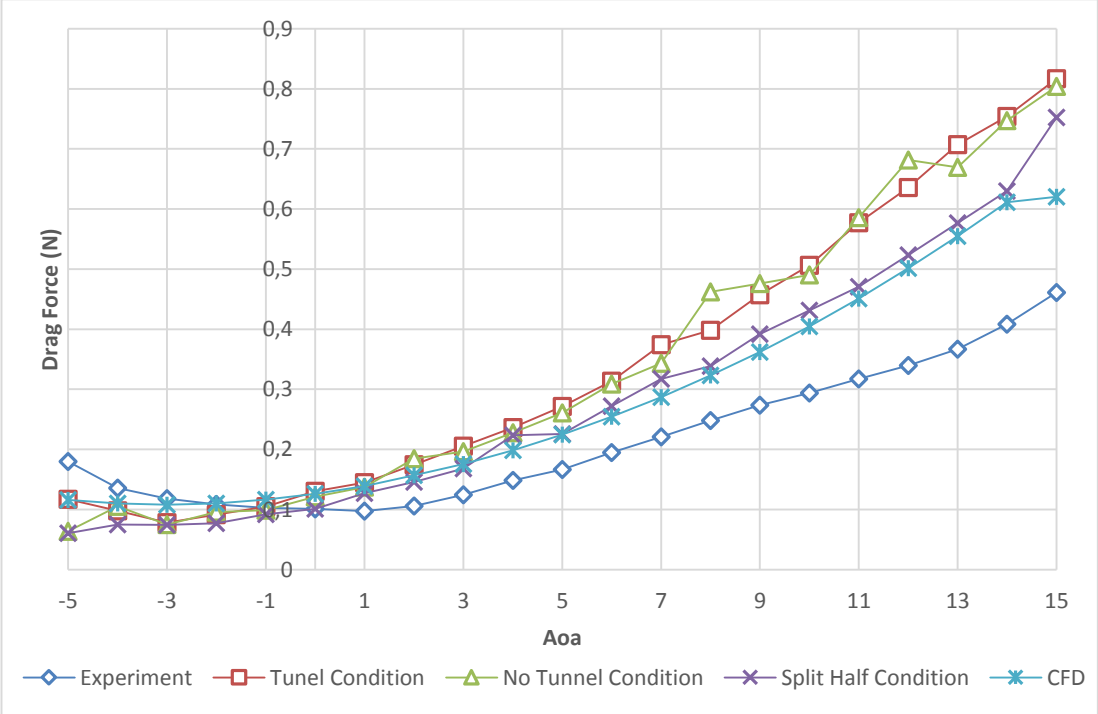

Figure 4-55 M10 drag results for 15 m/s

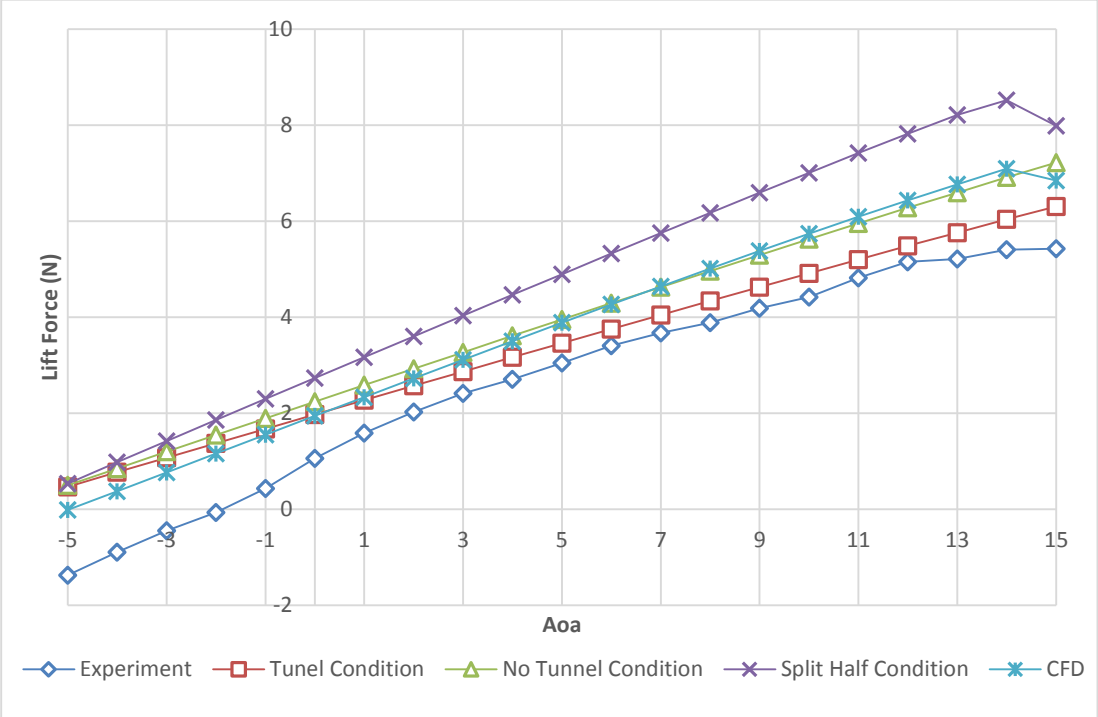

Figure 4-56 M10 lift results for 16 m/s

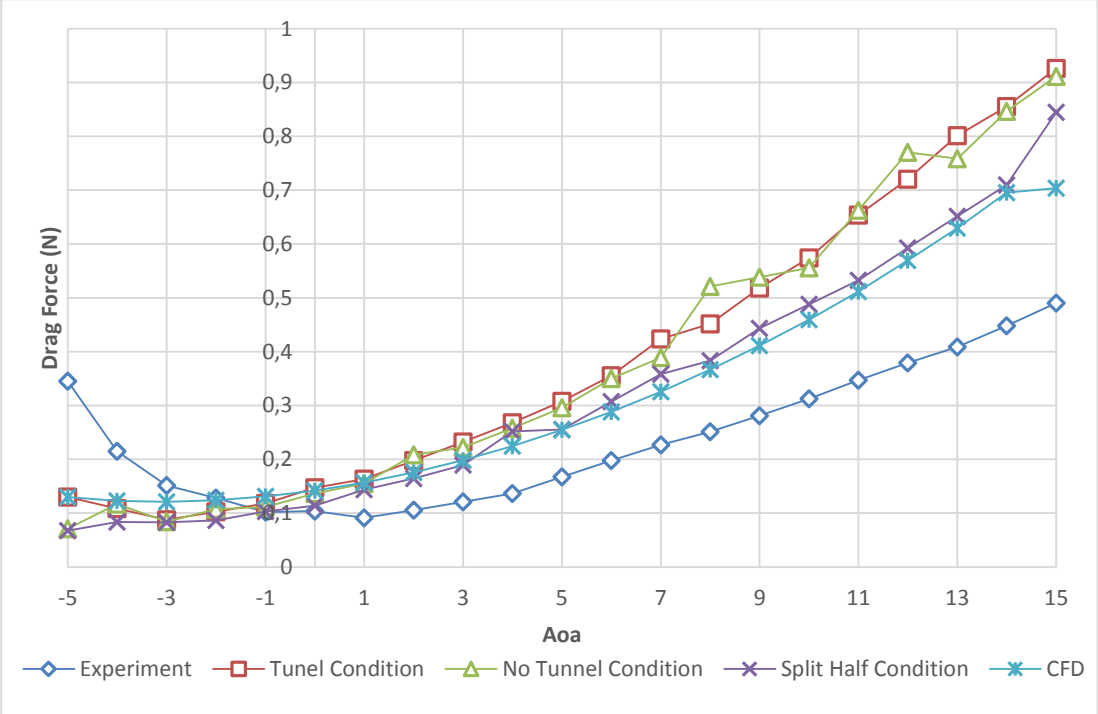

Figure 4-57 M10 drag results for 16 m/s

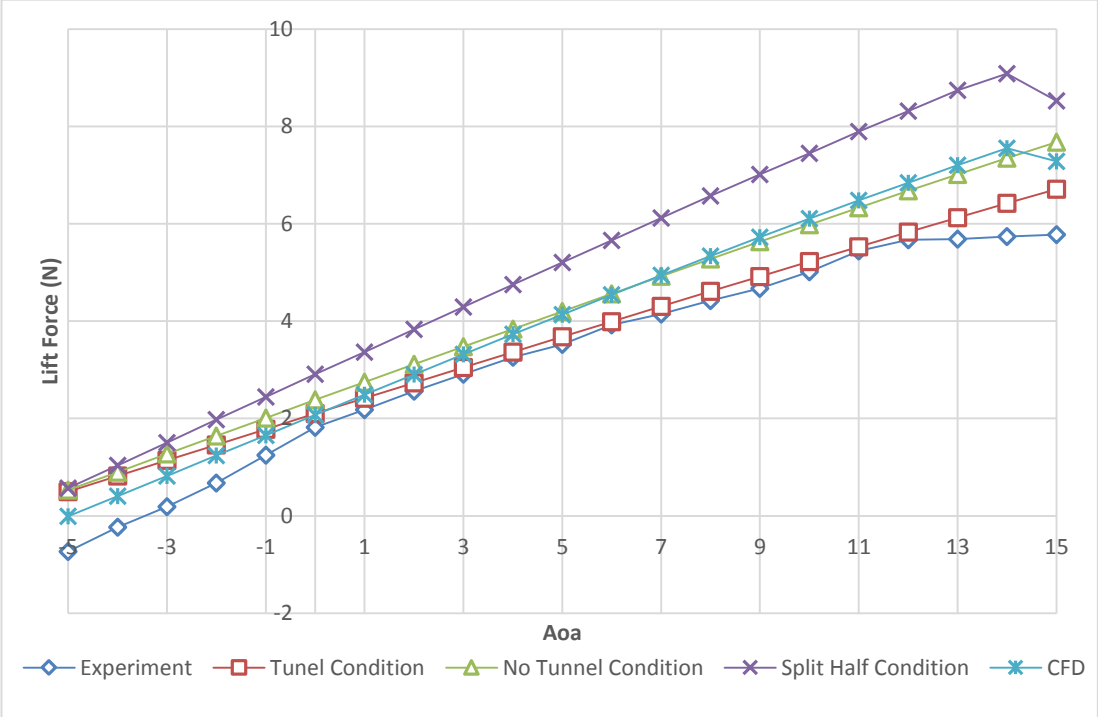

Figure 4-58 M10 lift results for 16.5 m/s

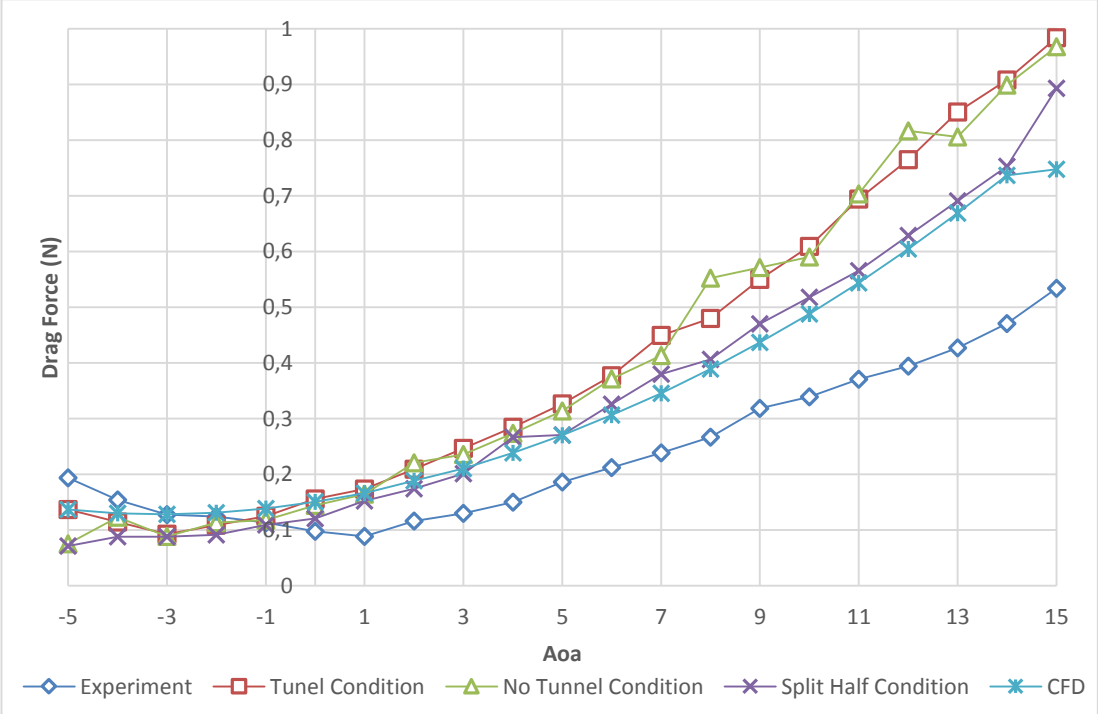

Figure 4-59 M10 drag results for 16.5 m/s

4.3.4. M16.5

M16.5 has the lowest wing area among all wing configurations. Therefore Reynolds number is lower with respect to corresponding cases with other wing configurations. This is one of the reason why results of the experiments are not matching and worse compared to other cases.

Nevertheless, same issues with the aforementioned cases are still valid such as lift curve slope incompatibility at low angle of attacks. Abnormal lift curve slope trends owing to laminar bubble separation occurred at the trailing edge region. Besides, low Reynold number conditions (Re#:42000 – 46000) still results in early stall behavior but drag curves are good and agreement with the numerical calculations, shown in Figure 4-60, Figure 4-61, Figure 4-62 and Figure 4-63. As the flow velocity increases, effects of separation become more visible in the trend of lift curve slope. Lift curve slope of the corresponding cases has the recovering trend shown in Figure 4-64, Figure 4-66 and Figure 4-68. Besides, drag curves of the corresponding cases start to diverge from numerical results at high angles of attack. Also, recovery of the laminar bubble separation at the trailing edge can be understood by looking at the drag curves of cases where the stall behavior occurs, sudden decrease of the drag force at the high angles of attack refers to overcoming separation of the flow. This phenomenon can be seen at Figure 4-65, Figure 4-67 and Figure 4-69.

As the Reynolds numbers have the values over 60000, lift curve slope trends are becoming more similar to numerical results. Notwithstanding, there is bias in the results and early stall behavior is experienced at high angles of attack seen in Figure 4-70, Figure 4-72 and Figure 4-74. Besides, numerical drag results are overpredicted also for this wing configuration. Dissimilation of the drag results at the low and negative angle of attacks could be explained by lower surface separations which was explained in the above sections seen in Figure 4-71, Figure 4-73 and Figure 4-75. To sum up, It was realized that prediction of the aerodynamic forces are troublesome but as the Reynolds number passes the 60000 limit, predictions of the aerodynamic forces become more dependable. Also, Lee et. al. states that 70,000 is the critical value for the prediction by numerical tools [45].

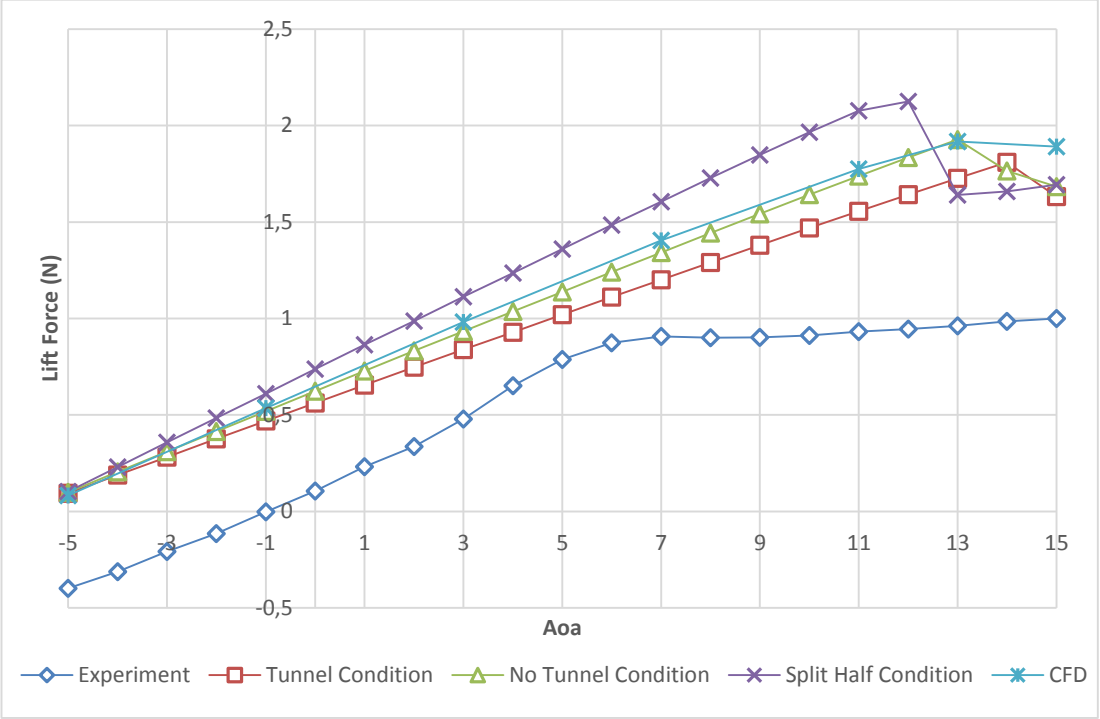

Figure 4-60 M16.5 lift results for 10 m/s

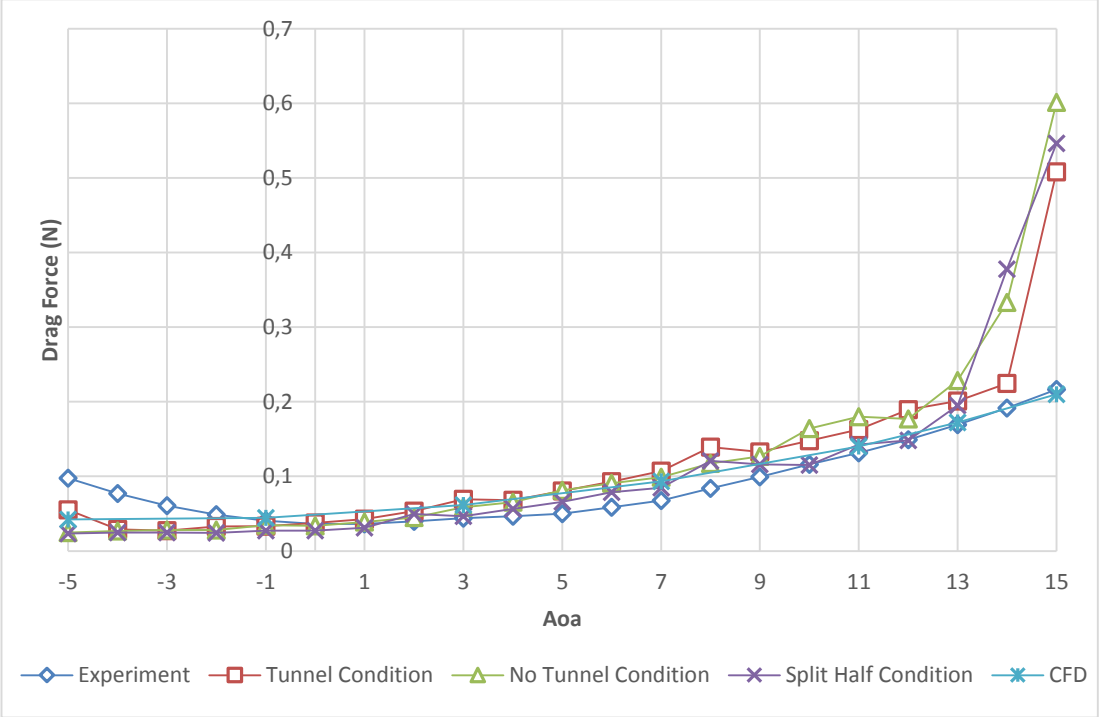

Figure 4-61 M16.5 drag results for 10 m/s

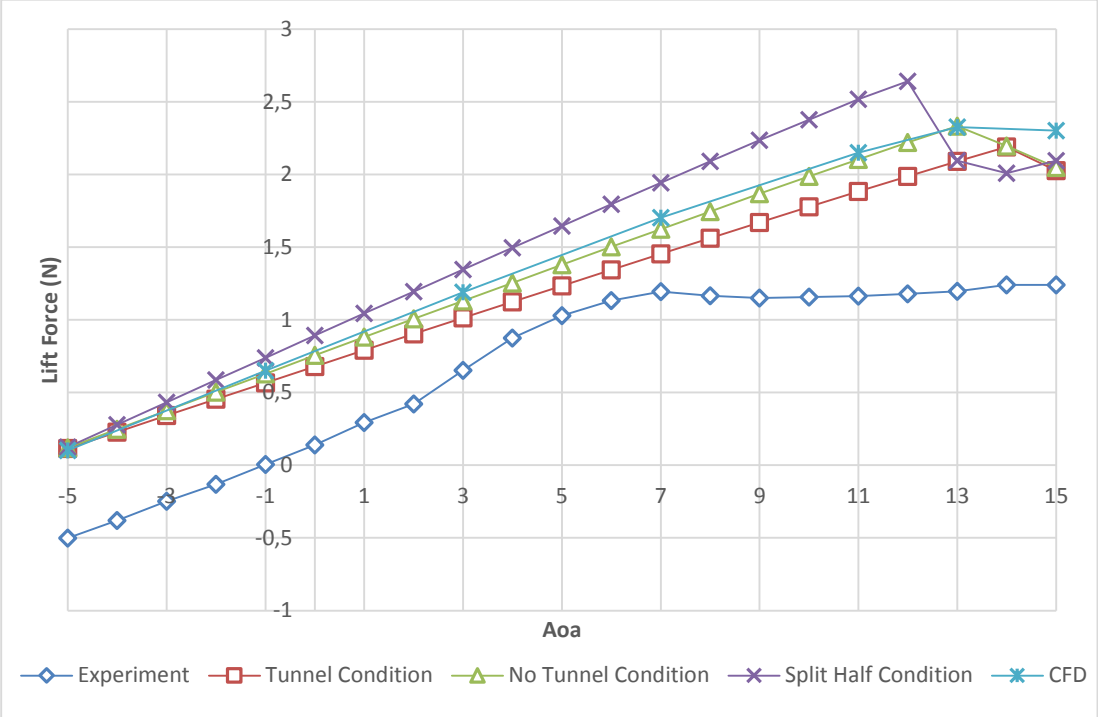

Figure 4-62 M16.5 lift results for 11 m/s

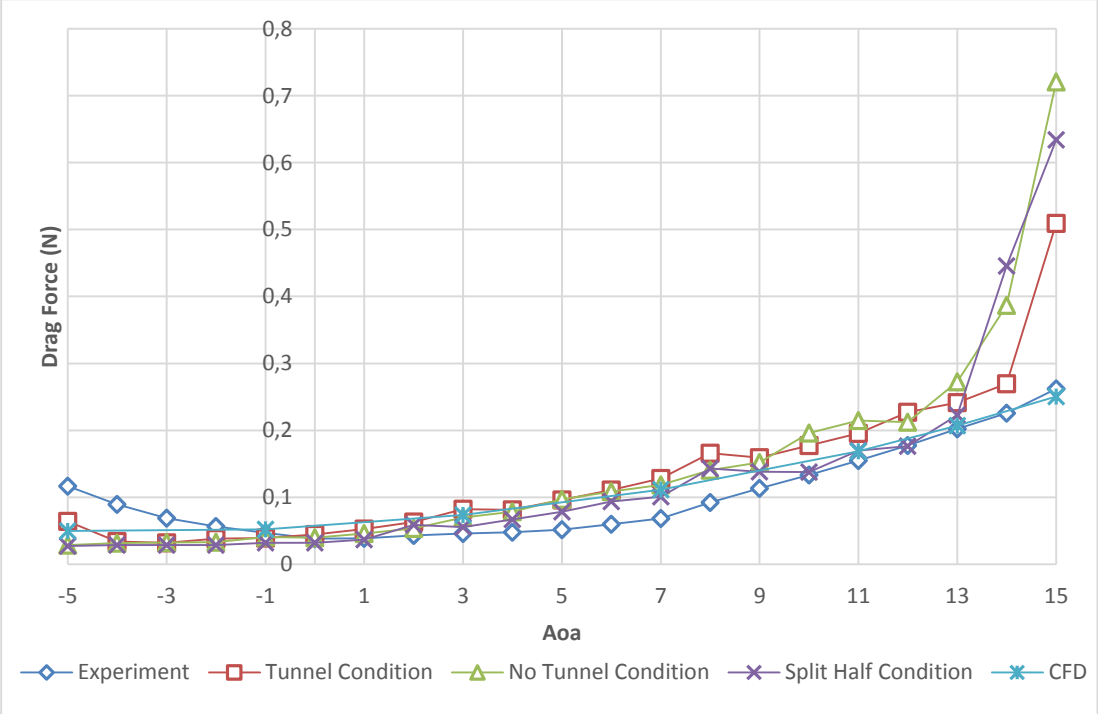

Figure 4-63 M16.5 drag results for 11 m/s

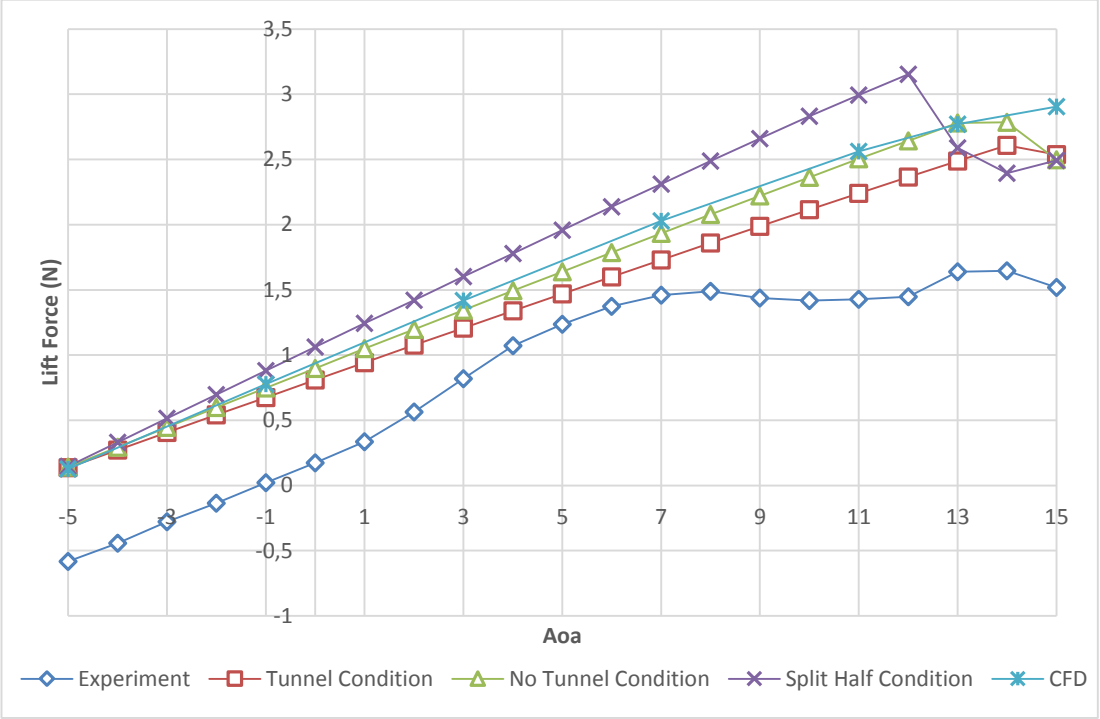

Figure 4-64 M16.5 lift results for 12 m/s

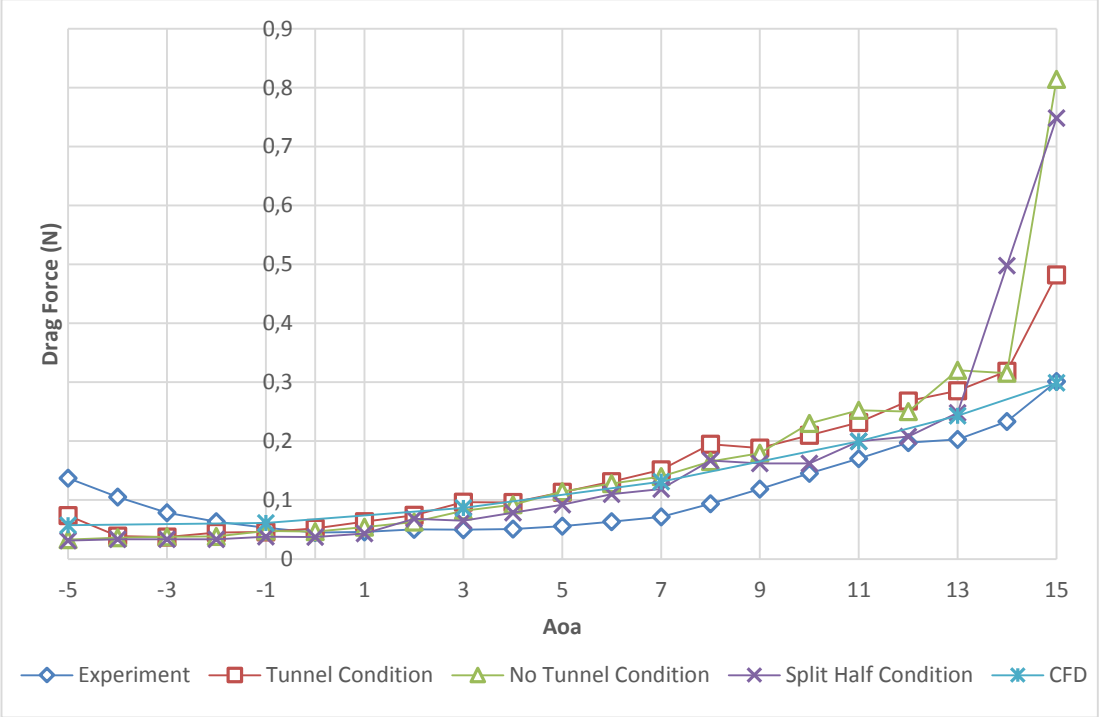

Figure 4-65 M16.5 drag results for 12 m/s

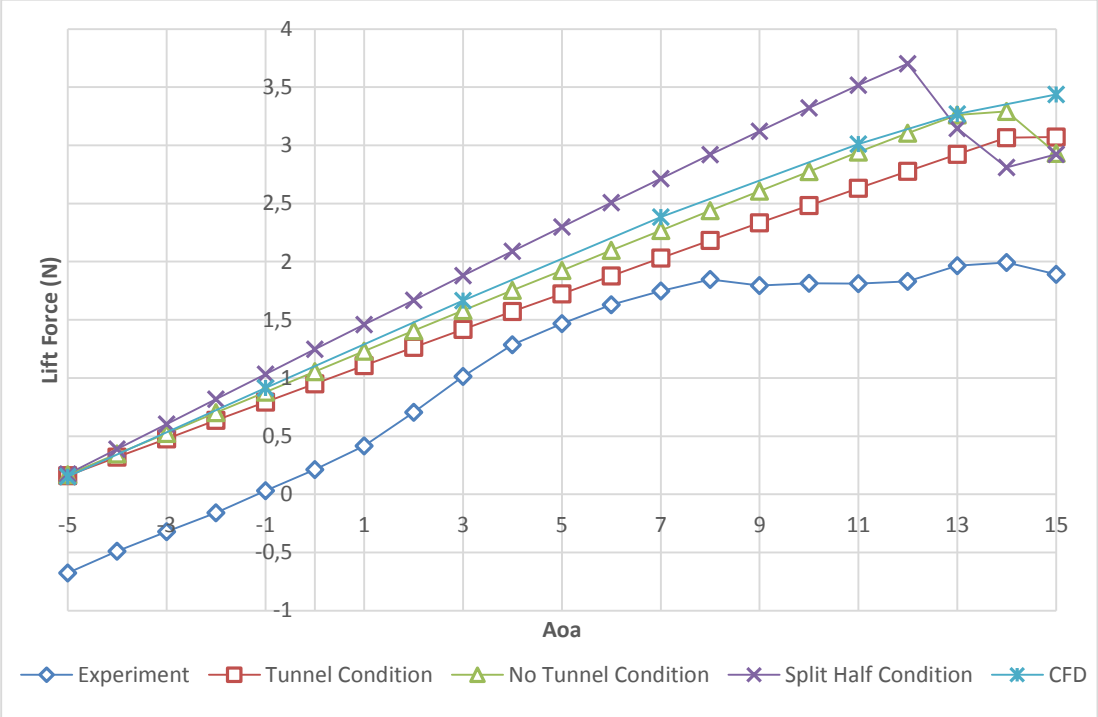

Figure 4-66 M16.5 lift results for 13 m/s

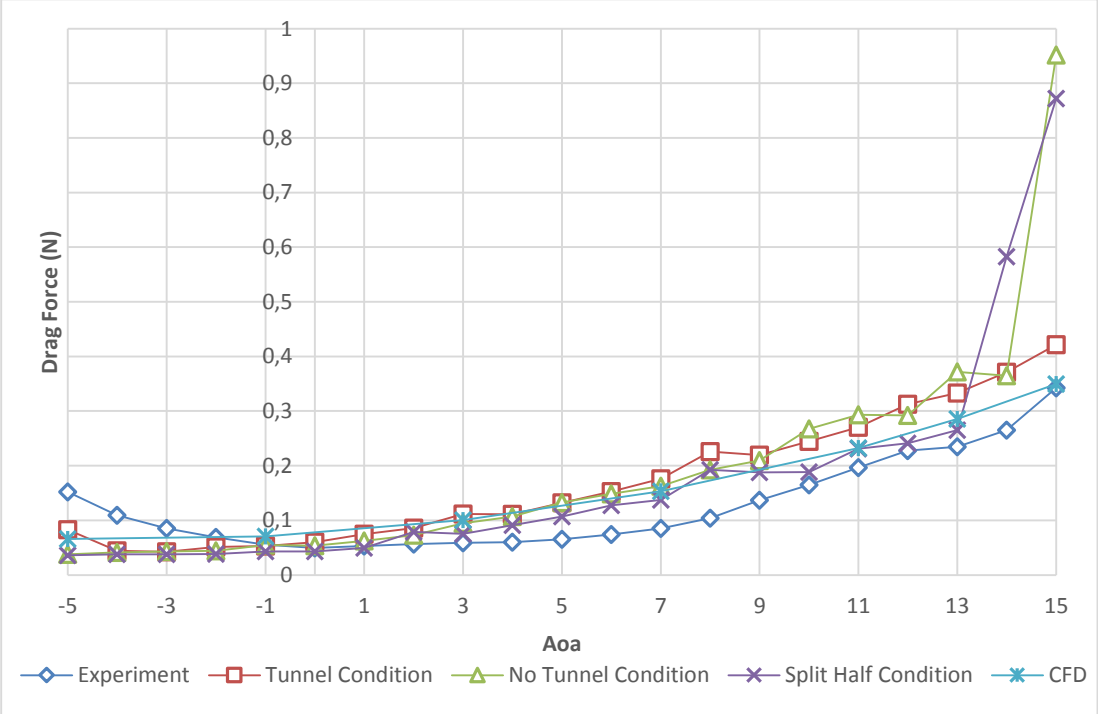

Figure 4-67 M16.5 drag results for 13 m/s

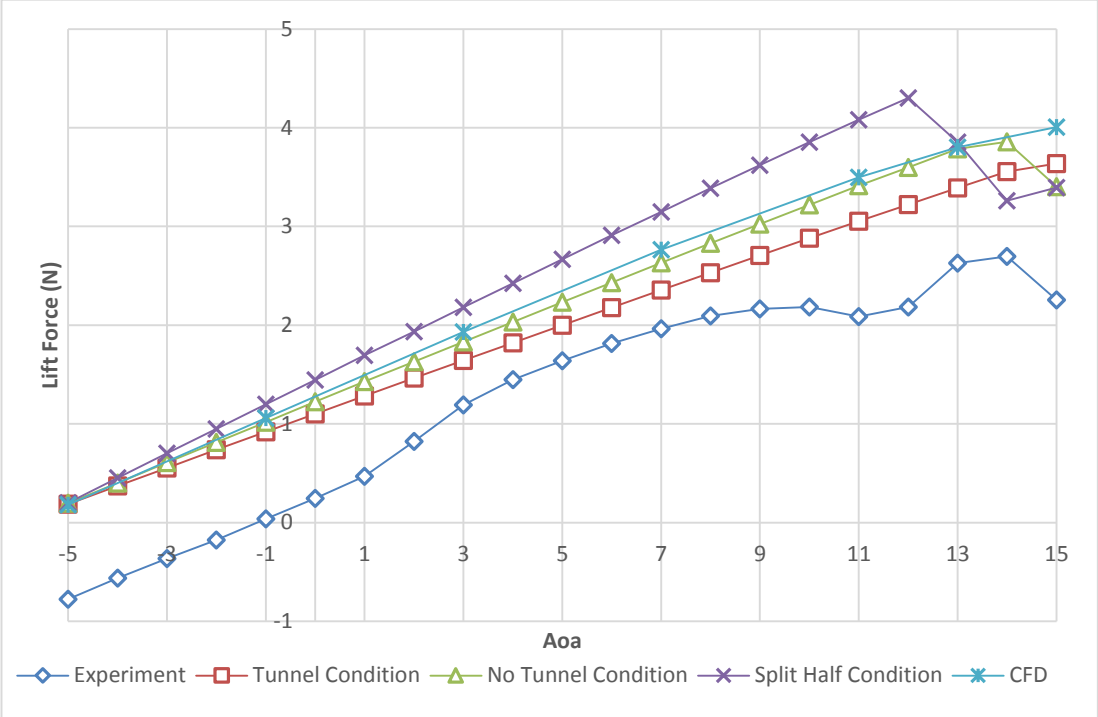

Figure 4-68 M16.5 lift results for 14 m/s

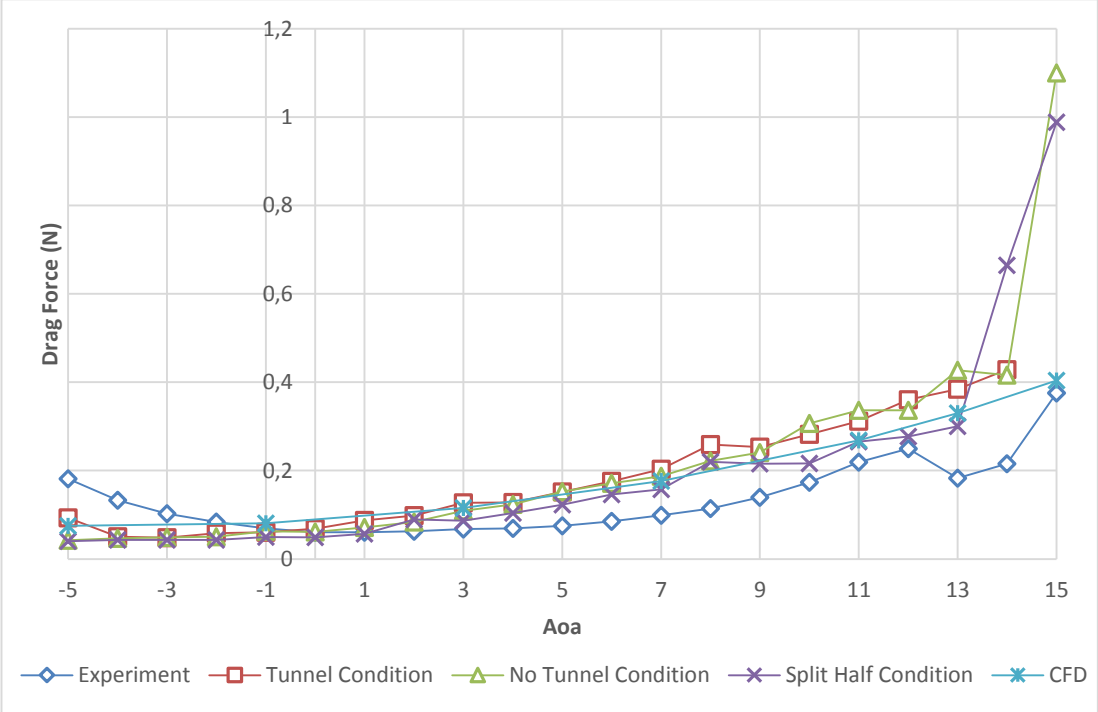

Figure 4-69 M16.5 drag results for 14 m/s

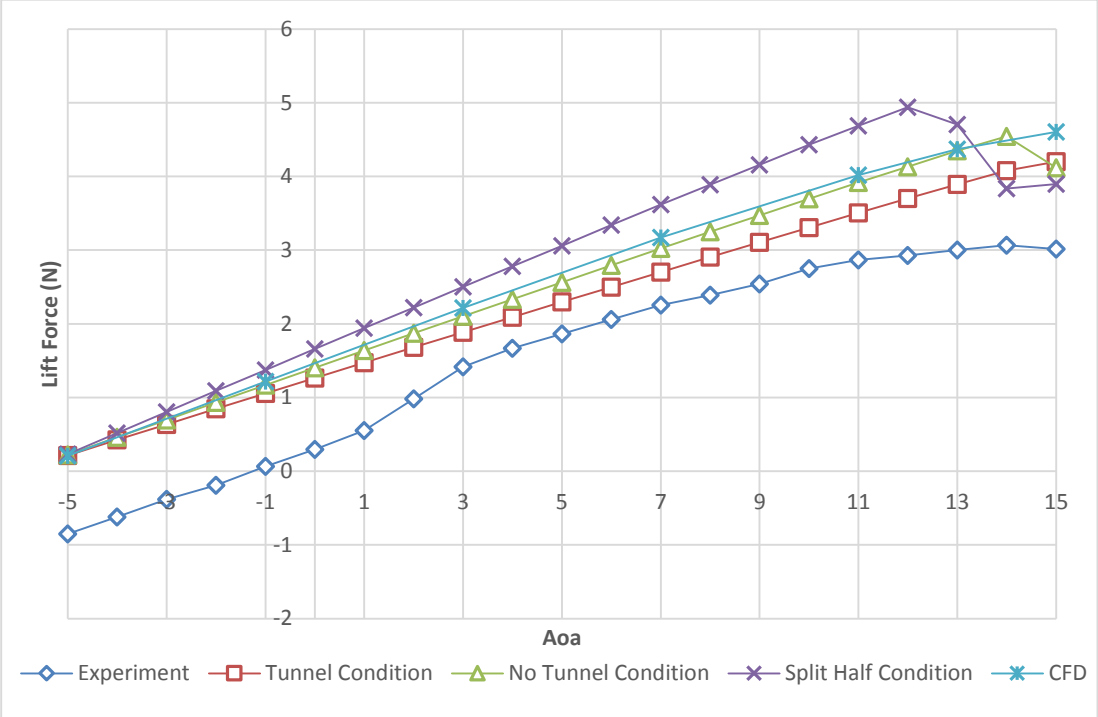

Figure 4-70 M16.5 lift results for 15 m/s

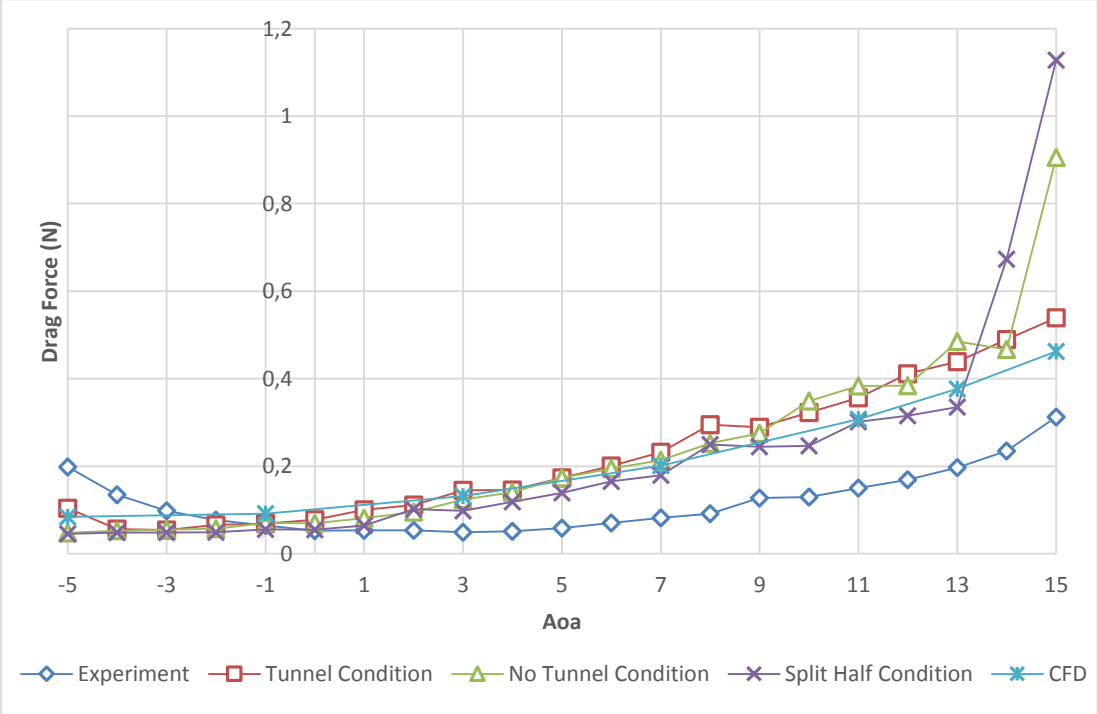

Figure 4-71 M16.5 drag results for 15 m/s

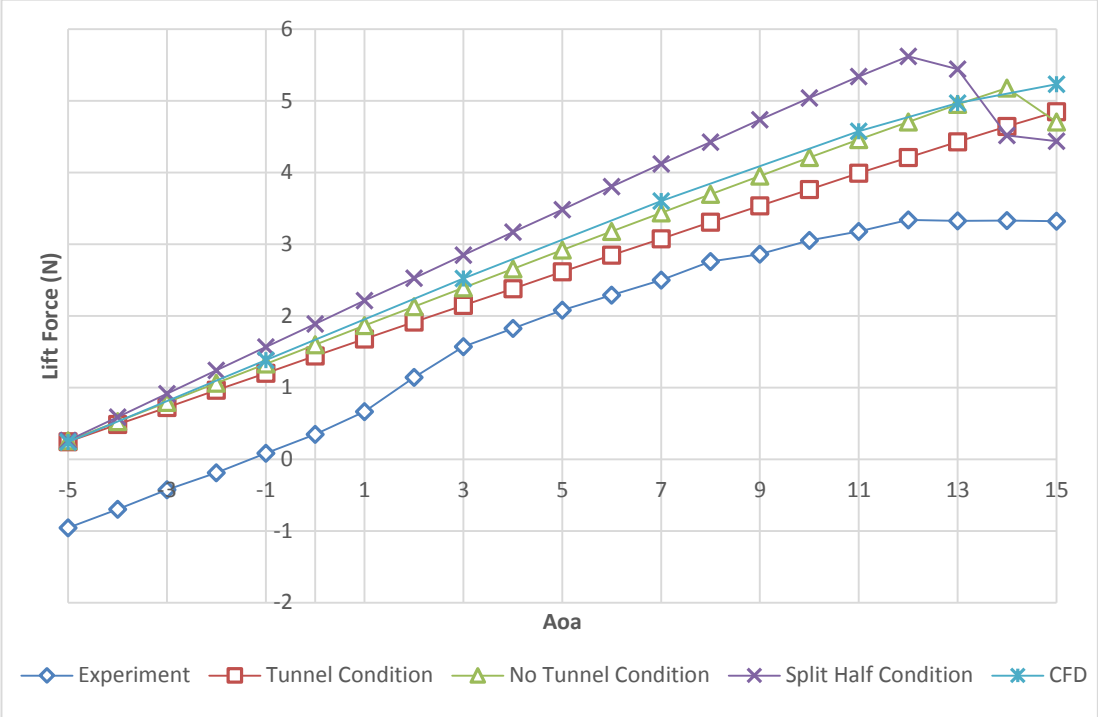

Figure 4-72 M16.5 lift results for 16 m/s

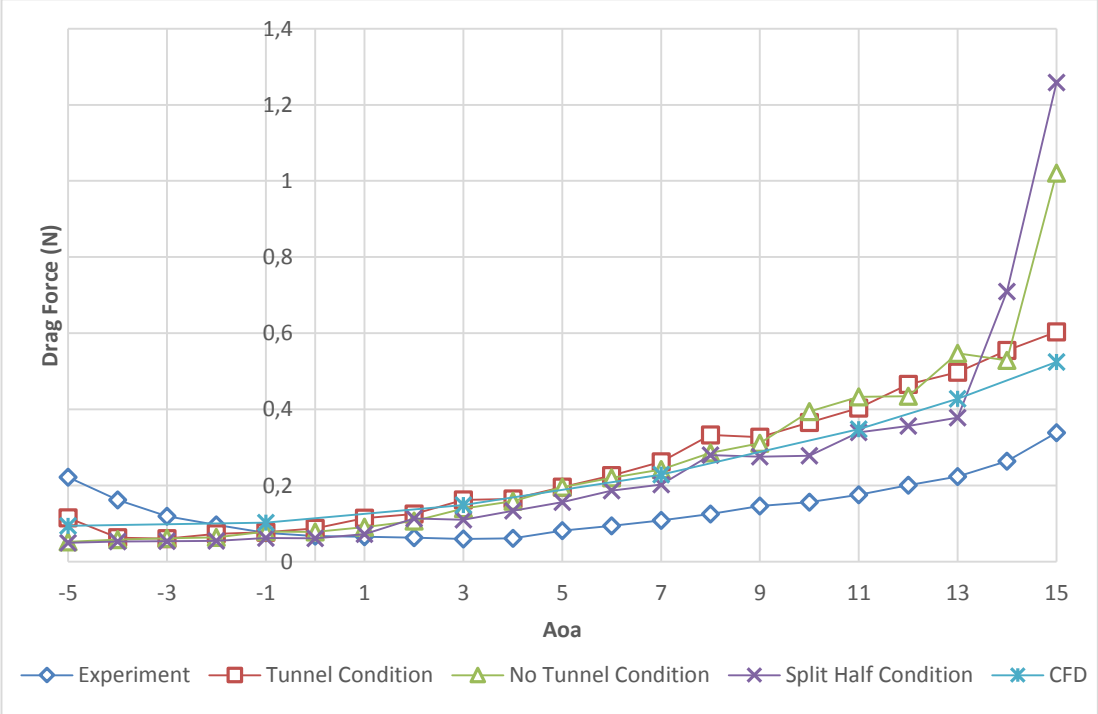

Figure 4-73 M16.5 drag results for 16 m/s

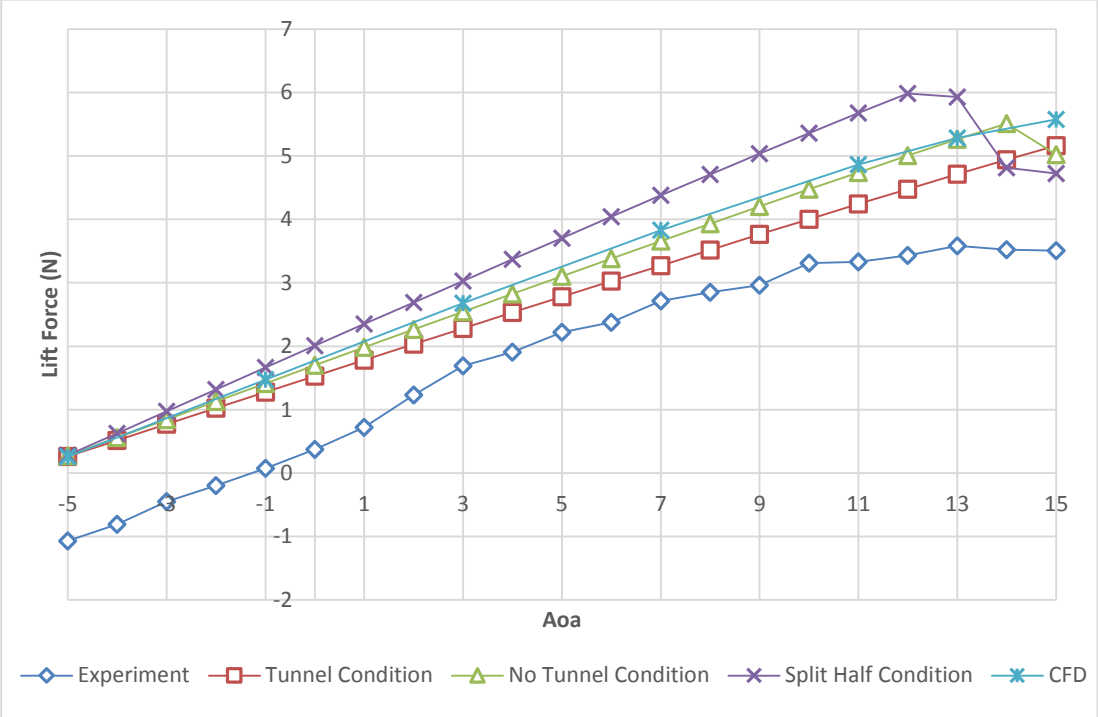

Figure 4-74 M16.5 lift results for 16.5 m/s

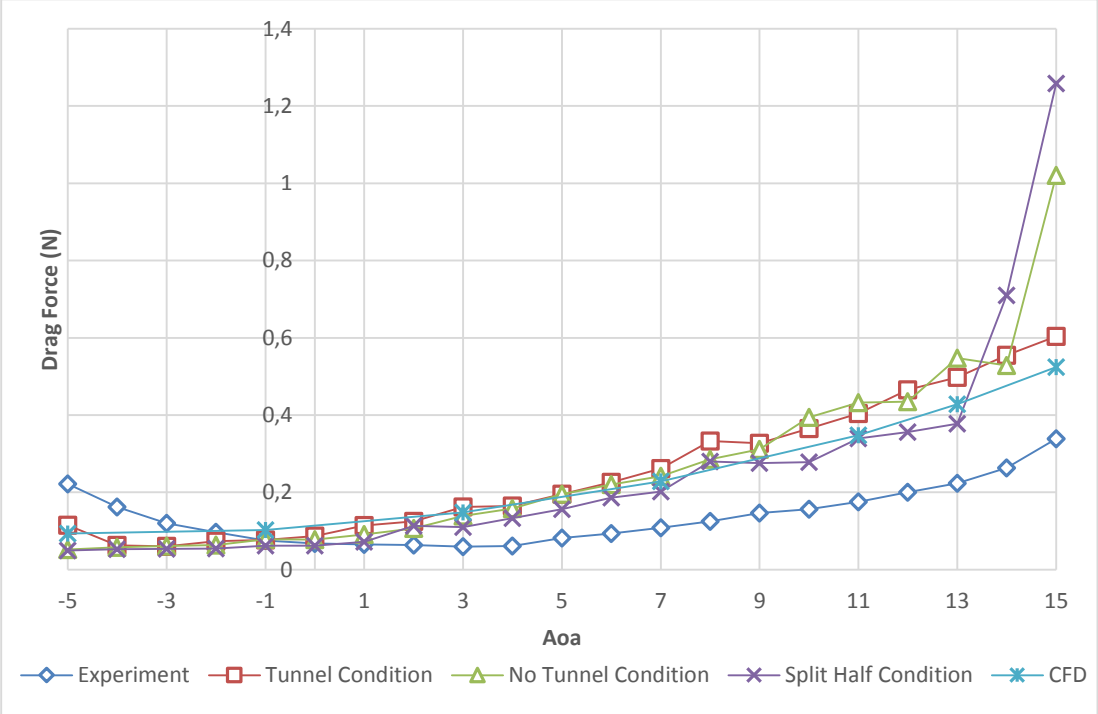

Figure 4-75 M16.5 drag results for 16.5 m/s

4.3.5. Optimization Curve

In this chapter, experimental drag results of all wing configurations are presented in Figure 4-76 where corresponding wing configuration produces 2.5 N lift force. This graph shows all the work done throughout this study.

Every wing configuration except M10, draw resembling curves as expected where drag values of the wing configuration are the lowest at the particular velocity where the corresponding wing is optimized. Having same Reynolds number range interval by O14 and M16.5 is the one of the main reason of this drag curve similarity.

In detail, among the all other wing configurations, M10 has the most different drag curve. Reason of this drag curve dissimilarity could be explained by high Reynolds number of the corresponding wing.

Each wing drag curve is represented in the Figure 4-76, also trend lines are generated in order to expand drag curve trend where experiments could not be performed.

In Figure 4-76 light blue starred line is representing the wing configurations with hypothetical shape shifting mechanism. If the optimization tool is utilized for other flow velocities such as 12m/s and 13 m/s, this line would become more likely to be flat.

Ultimately, wings generated by aerodynamic optimization tool give the least amount of drag at the freestream velocity where this particular wing was optimized, even though optimization tool and experimental results do not exactly match. In addition, 50% reduction in drag force points out that optimization tool is a robust tool in terms of optimization. This is to say that, optimization tool that developed separately, serves it purpose successfully.

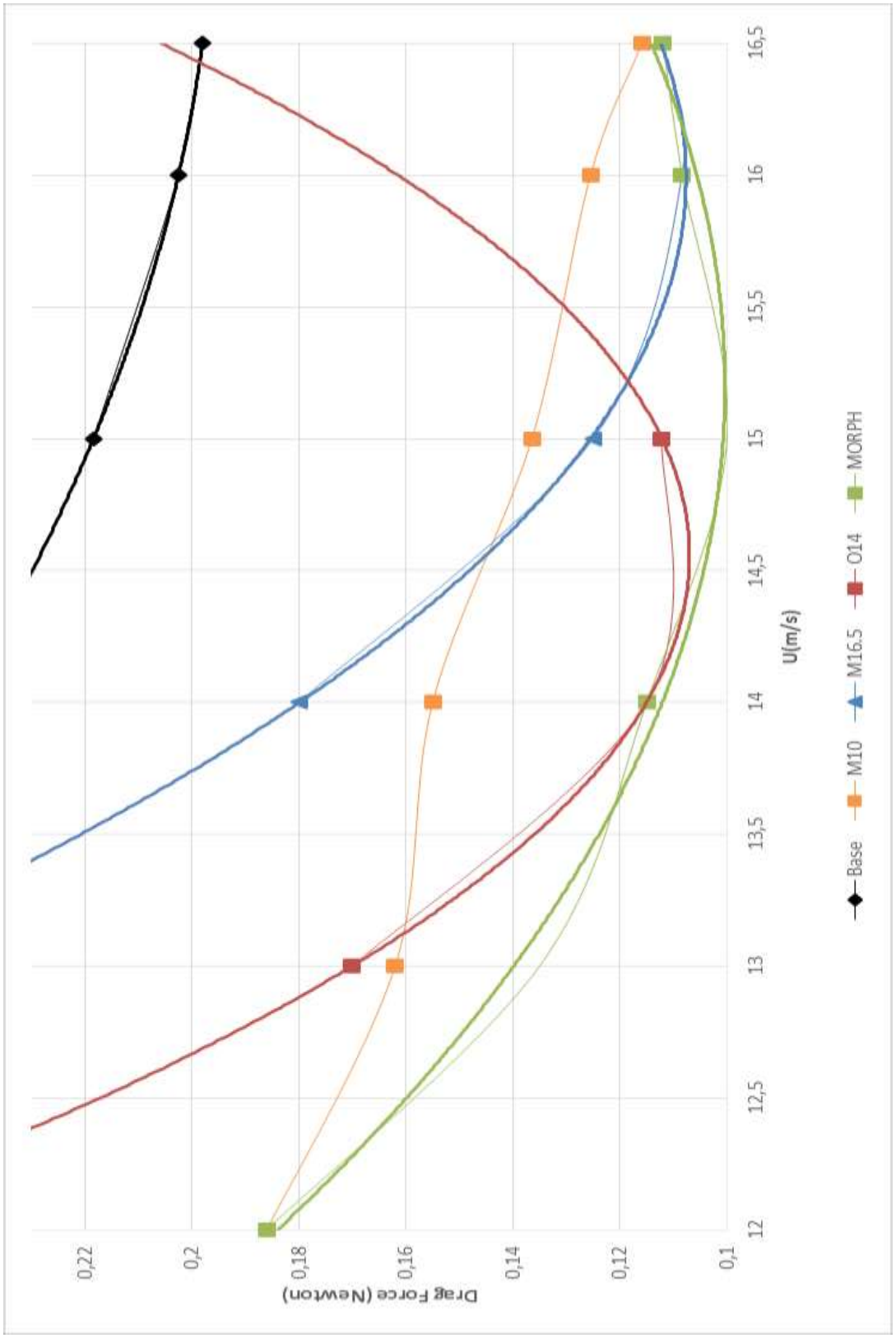

Figure 4-76 Experimental Drag values where corresponding wing produce 2.5 N lift

CHAPTER 5

CONCLUSIONS

In this thesis, experimental and CFD studies were conducted in order to validate the outcomes from optimization tool. For this purpose, a test setup and 4 different wing configurations were manufactured and used in a low speed blower type wind tunnel. The test setup was mounted on the middle of the wind tunnel's test section and instrumented with a high precision load cell.

Before the initialization of the experiments, extensive error analysis and calibration runs were performed in order to obtain the best experimental data possible. In the analysis, the phenomenon called, eccentric load sensitivity error, was encountered. In the light of the experiments conducted for load sensitivity error, this particular problem was modeled mathematically and deducted from experimental results in order to collect clean data.

The wind tunnel experiments and CFD analyses were performed for each of the different wing configurations which are the baseline wing, and three morphing wings optimized for 14 m/s, 10 m/s and 16.5 m/s, respectively. These analyses include 8 different flow velocities which are 10, 11, 12, 13, 14, 15, 16 and 16.5 m/s and 21 different angles of attack which ranged from -5 degree to 15 degree with 1 degree increment.

CFD analyses were modeled by taking the real conditions of our ambient test setup and the dimensions of the wind tunnel into account. Spallart-Almaras turbulence model was chosen for its good prediction of lift and drag and the applicability to these cases. Meshes were generated with regards to boundary layer, wing tip vortices and aerodynamic forces. Roughly, each CFD case contains roughly 2.5 million mesh elements.

Wind tunnel experiments were performed for each wing configuration at the above mentioned velocities and angles of attack. Laminar separation bubble (LSB) occurred

on the optimized and morphing wings. Separated shear layer reattached on the wings surface as the velocity of the flow was increase. This occurrence is common for such low Re number flows, with thin and cambered airfoils. Also, these findings are found beneficial for the improvement of the optimization tool.

Wind tunnel measurements and CFD analyses were performed for each wing configuration to validate the theoretical design tool. Besides, it can be stated that the main deductions from experimental works such as laminar bubble separation, surface roughness effects, low Reynolds number corrections and airfoil parameters should be added to the optimization tool for a more capable and realistic solver.

In the literature survey, it was clearly seen that numerical optimizations are useful but not completely precise. However, by this study, it is observed that these numerical optimization tools should be improved through experimental efforts. The results and observations that were obtained in this work may offer some additional intuition into not only the optimization process but also to the design of wing planforms and airfoils for low Reynolds number performance.

Although, it was not within the scope of the thesis, designing and manufacturing a wind tunnel test setup aimed measuring data with the lowest possible error proved to be a great challenge.

To sum up, this work was devoted to validate and guide the numerical optimization tool generated for three dimensional morphing wing configurations. This kind of studies related to more efficient structures shall arise awareness for a greener world.

5.1. Lessons Learned During Experiments

A lot of experience were gained through the wind tunnel experiments which were mostly originated from problems that were encountered during the tests. These lessons are so important that they must be expressed in order to prevent recurrence of the time and energy loss.

Test setup should be capable and up to date with respect to current technology. Incompatibility of the hardware and test equipment as well as different input protocols of the test equipment caused synchronization problems. Therefore, test equipment such

as wind tunnel, should be operated by one station (PC) and data (load cell and wind speed measurements) should be collected by the same station. This improvements in the tests will make the experiments more reliable.

Besides, while test is designed on the paper, maximum velocity concern should be taken into account and maximum test velocity should be at least 15% lower than the wind tunnel maximum speed specification. Thus, heating and speed maintaining issues can be eliminated.

This kind of works should be done by considering Reynolds number. In the results of the experiments, it was obviously seen that Reynolds number is the dominating parameter of the separation and convergence of results, not velocity. Therefore, it is recommend that experiments should be utilized in a Reynolds number less than 70,000.

5.2. Future Works

The first suggestion out of this work is to conduct this experiment with a non-intrusive method such as PIV in order to investigate the laminar separation bubble. There is also no doubt that developing CFD models where separation can be modeled will be beneficial. Besides, wing tip vortex behaviors regarding the optimized and the non-optimized wings may be a vital work from the optimization stand point.

Secondly, morphing mechanisms should be produced in order to investigate material constraints, material-related or manufactural allowances and their effects to measurements. These shape shifting mechanisms should also perform the mission-based scenarios in flight tests. Especially, unsteady aerodynamics should be studied in order to explore turbulence and vortex characteristics, while outer geometry of the wings change their shapes in different time intervals.

Last but not least, real morphing wing mechanisms should be implemented on a test aircraft and its flight characteristics should be analyzed in detail. Especially, the stability of the aircraft should be analyzed in the transformation interval. This transition region is expected to cause severe changes in the flight dynamics of the aircraft.

REFERENCES

[1]. Patel, S., Majji, M., Koh, B., Junkins, J., & Rediniotisx, O. (2005). *Morphing wing: A demonstration of aero servo elastic distributed sensing and control*. Technical report, Texas Institute for Intelligent Bio-nano Materials and Structures for Aerospace Vehicles.

[2]. Wall, R. (2002, April 8). *Darpa Eyes Materials for 'Morphing' Aircraft*, Aviation Week and Space Technology, 156(14), 36.

[3]. Valasek, J. (Ed.). (2012). *Morphing aerospace vehicles and structures* (Vol. 56). John Wiley & Sons.

[4]. Anonymous (2006) *Defense Technology Objectives, DTO 71*, DDR&E. Washington, DC: U.S. Department of Defense.

[5]. Melin, T. (2006). *Multidisciplinary Design in Aeronautics, Enhanced by Simulation-Experiment Synergy.* Stockholm: Kungliga Tekniska högskolan.

[6]. Ajaj, R., Keane, A., Beaverstock, C., Friswell, M., & Inman, D. (2013). *Morphing Aircraft: The Need for a New Design Philosophy*. Aerospace Industries Association of Canada.

[7]. Weisshaar T. A., "*Morphing Aircraft Technology – New Shapes for Aircraft Design"*, TO-MP-AVT-141, 2006.

[8]. Arasse, D. (1998). *Leonardo Da Vinci*. New York: Konecky & Konecky.

[9]. Gray, C. (2003, January 1). Leonardo da Vinci (1452-1519). Retrieved December 15, 2014, from http://www.flyingmachines.org/davi.html.

[10]. Anonymous. (2007, October 11). Eole/Clément Ader. Retrieved December 17, 2014, from https://web.archive.org/web/20071020082858/http:/www.eads.com/1024/en/eads/history/airhist/1890_1899/ader.html.

[11]. Wright, Orville, "*How We Invented the Airplane*." (From depositions in Montgomery vs. U.S. 13 Jan 1920 and 2 Feb 1921; in Kelly, Fred C. (editor) How We Invented the Airplane, an Illustrated History. Dover Publications, New York, 1953, p 12-13).

[12]. Kelly, Fred C. *The Wright Brothers, a Biography*. Harcourt, Brace and Co., New York, 1943, p 49.

[13]. McFarland, Marvin W. (ed) *the papers of Wilbur and Orville Wright.* McGraw-Hill Book Co., New York, 1953, pp 8-12, 1183; Orville's illustrations of the 1899 Kite are on pages 9-10.

[14]. Anonymous. (n.d.). The Breakthrough Concept. Retrieved December 17, 2014, from http://airandspace.si.edu/exhibitions/wright-brothers/online/fly/1899/breakthrough.cfm.

[15]. Anonymous. (n.d.). MAK-10. Retrieved December 11, 2014, from http://www.airwar.ru/image/idop/xplane/mak10/mak10-3.jpg.

[16]. Hallion, Richard P. *On The Frontier: Flight Research at Dryden 1946-1981* (NASA SP4303). Washington, DC: National Aeronautics and Space Administration, 1984 (revised 2003 in Smithsonian edition). ISBN 1-58834-134-8.

[17]. General Dynamics F-111. (2014, December 5). Retrieved December 15, 2014, from http://hars.org.au/general-dynamics-f-111c/.

[18]. Logan, D. (1998). *General Dynamics F-111 Aardvark*. Schiffer Pub.

[19]. Davies, P. (2013). *General Dynamics F-111 Aardvark (Vol. 10)*. Osprey Publishing.

[20]. Army, U. S. (2006). FM 3-01.80 (FM 44-80) Visual Aircraft Recognition.p124.

[21]. Peter Lert, "*The FS-29, a telescoping wing sailplane,"* Soaring, January 1976, pp. 21-27.

[22]. Wlezien R. W., Horner G. C., McGowan A.R., Padula S. L., Scott M. A., Silcox R. J., Simpson J.O., "*The Aircraft Morphing Program*", SPIE Proceedings, Vol. 3326, pp. 176-187, 1998.

[23]. DARPA's Morphing Program. (2004, January 1). Retrieved December 15, 2014, retrieved from http://dnc.tamu.edu/projects/flowcontrol/Morphing/public_html/darpa.html.

[24]. Ivanco, T. G., Scott, R. C., Love, M. H., Zink, S., & Weisshaar, T. A. (2007). *Validation of the Lockheed Martin morphing concept with wind tunnel testing*.AIAA Paper, 2235, 2007.

[25]. Poonsong, P. (2004). *Design and analysis of a multi-section variable camber wing* (M. Sc. Thesis, University of Maryland).

[26]. Boria F., Stanford B., Bowman S. and Ifju P., ‘‘*Evolutionary Optimization of a Morphing Wing with Wind-Tunnel Hardware in the Loop’’*, AIAA J., Vol. 47, pp. 399-409, 2009.

[27]. Sakarya, E. (2010). *Structural Design and Evaluation of an Adaptive Camber Wing* (M. Sc. Thesis, METU,, Institute of Natural and Applied Sciences).

[28]. Bilgen, O., Friswell, M. I., Kochersberger, K. B., & Inman, D. J. (2011). *Surface actuated variable-camber and variable-twist morphing wings using piezocomposites*. Proceedings of 52nd AIAA/ASME/ASCE/AHS/ASC Structures, Structural Dynamics, and Materials, 4(7), 2011-2072.

[29]. Bilgen, O., Junior, C. D. M., Kochersberger, K. B., & Inman, D. J. (2010). *Macro-fiber composite actuators for flow control of a variable camber airfoil.* Journal of Intelligent Material Systems and Structures, 1045389X10392613.

[30]. Blondeau, J. E., & Pines, D. J. (2004, April). *Pneumatic morphing aspect ratio wing*. In AIAA Structures, Structural Dynamics and Materials Conference.

[31]. Blondeau, J., Richeson, J., & Pines, D. J. (2003). *Design, development and testing of a morphing aspect ratio wing using an inflatable telescopic spar*. AIAA paper, 1718, 7-10.

[32]. Neal, D. A., Good, M. G., Johnston, C. O., Robertshaw, H. H., Mason, W. H., & Inman, D. J. (2004). *Design and wind-tunnel analysis of a fully adaptive aircraft configuration.* Proceedings of AIAA/ASME/ASCE/AHS/ASC SDM, Palm Springs, California.

[33]. Gamboa, P., Vale, J., P. Lau, F. J., & Suleman, A. (2009). *Optimization of a morphing wing based on coupled aerodynamic and structural constraints*. AIAA J.l, 47(9), 2087-2104.

[34]. Körpe, D. S. (2014). *Aerodynamic Modelling and Optimization of Morphing Wings* (Doctoral Dissertation, Middle East Technical University).

[35]. ATI Force / Torque Sensor: Gamma. (n.d.). Retrieved December 24, 2014, from http://www.ati-ia.com/products/ft/ft_models.aspx?id=Gamma.

[36]. NI USB-621x Specifications. (2009, April 1). pp. 3-5. Retrieved April 5, 2015, from http://www.ni.com/pdf/manuals/371932f.pdf.

[37]. Model 471B. (2009, January 1). Retrieved May 1, 2015, from http://www.dwyer-inst.com/Product/TestEquipment/Thermo-Anemometers/Model471B#specs.

[38]. Mitchell, R. A., Seifarth, R. L., & Reeve, C. P. (1986). *Eccentric Load Sensitivity of Force Sensors. In Mechanical Problems in Measuring Force and Mass* (pp. 275-281). Springer Netherlands.

[39]. ANSYS Solver Settings. (2006, December 1). *Introductory FLUENT Training*. Lecture conducted from Fluent User Services Center.

[40]. Ortiz, A. D., Quiroz, L. E., & Köck, R. A. *Aerodynamic Performance Analysis Of A Low-Speed Acrobatic Airplane By Numerical Simulation*. Mecánica Computacional, 21, 378-391.

[41]. Wells, J. B., Salem-Said, A., & Ragab, S. A. (2009). *Effects of turbulence modeling on RANS simulations of tip vortices* (Doctoral dissertation, University Libraries, Virginia Polytechnic Institute and State University).

[42]. Wheeler, A. J., Ganji, A. R., Krishnan, V. V., & Thurow, B. S. (1996). *Introduction to engineering experimentation* (p. 159). New Jersey: Prentice Hall.

[43]. Ostovan, Y. (2011). *Experimental ınvestigation of Waveform Tip Injection on the Characteristics of the Tip Vortex* (M. Sc. Thesis, Middle East Technical University).

[44]. Diwan, S. S., & Ramesh, O. N. (2007). *Laminar separation bubbles: Dynamics and control.* Sadhana, 32(1-2), 103-109.

[45]. Lee, C. S., Pang, W. W., Srigrarom, S., Wang, D. B., & Hsiao, F. B. (2006). *Classification of airfoils by abnormal behavior of lift curves at low Reynolds number.* In 24th AIAA Applied Aerodynamics Conference.

[46]. Schlichting, H., Gersten, K., & Gersten, K. (2000). *Boundary-layer theory*. Springer Science & Business Media.

[47]. Ma, R., & Liu, P. (2009). *Numerical simulation of low-Reynolds-number and high-lift airfoil S1223*. In Proceedings of the World Congress on Engineering (Vol. 2).

[48]. Reid, M. R., & Kozak, J. (2006, August). *Thin/cambered/reflexed airfoil development for micro air vehicle applications at Reynolds numbers of 60,000 to 100,000*. In AIAA Atmospheric Flight Mechanics Conference and Exhibit.